Experimental Study of the Mechnical Behaviour of the Sandy Facies of Opalinus Clay at Mont-Terri

GRS - 555

Gesellschaft für Anlagen-
und Reaktorsicherheit
(GRS) gGmbH

Experimental Study of the Mechnical Behaviour of the Sandy Facies of Opalinus Clay at Mont-Terri

LT-A Programme within the Mont-Terri-Project

Chun-Liang Zhang
Michael Komischke
Michael Kröhn
Abram Rogalski
Bernd Zehle

December 2019

Remark:

This report refers to the research project 02E11304 which has been funded by the German Federal Ministry for Economic affairs and Energy (BMWi).

The work was conducted by the Gesellschaft für Anlagen- und Reaktorsicherheit (GRS) gGmbH.

The authors are responsible for the content of this report.

GRS - 555
ISBN 978-3-947685-40-0

Keywords:
Opalinus Clay, Mechanical Characterization, Deformation, Damage, Strength, Water Retention, Swelling, Shrinkage

Table of contents

1 Introduction 1

2 Characterization of the studied claystone 5

2.1 Sampling 5

2.2 Mineralogical composition 7

2.3 Petrophysical properties 8

2.3.1 Definitions 8

2.3.2 Measured results 9

3 Mechanical deformation and strength 19

3.1 Experimental methodology 19

3.2 Load paths 21

3.2.1 Triaxial compression 23

3.2.2 Triaxial extension 24

3.2.3 Triaxial cyclic compression 24

3.2.4 Triaxial creep 25

3.3 Results and discussions 27

3.3.1 Triaxial compression 27

3.3.2 Triaxial extension 38

3.3.3 Triaxial cyclic compression 44

3.3.4 Strength in dependence on load path 54

3.3.5 Time-dependent behaviour 58

4 Moisture effects 67

4.1 Water uptake and free swelling 67

4.1.1 Samples 68

4.1.2 Test methodology 70

4.1.3 Test results 71

4.2 Strain response to humidity change under load 87

4.3 Influences of water content on stiffness and strength 90

5 Summary 97
5.1 Main characteristics 97
5.2 Deformation and strength 97
5.3 Moisture effects 98
5.4 Outlook 99

6 Acknowledgements 101

References 103

List of tables 111

List of figures 113

1 Introduction

The indurated Opalinus Clay formation (OPA) has been proposed as a potential host rock for a deep geological repository for high-level radioactive waste (HLW) in Switzerland /NAG 02/14/. Recently, the part of the OPA formation in Southern Germany has been considered as one of the German generic models for elaborating the methodology of safety demonstration of a HLW repository in clay rock /JOB 17/. The selection of OPA as a potential host rock is due to its favourable attributes, such as appropriate formation size and depth, homogeneous and stable rock mass, extremely low hydraulic conductivity, self-sealing potential of fractures, and high sorption capacity for the retardation of radionuclides. The potential repositories will be constructed in the clay formation with a thickness of about 100 m at a depth of 400-700 m below the ground surface.

In the framework of the R&D programme, site-independent research work has been intensively performed by participation in international research activities investigating the OPA claystone at the Underground Research Laboratory (URL) Mont-Terri in Switzerland. Since last two decades, the OPA has been comprehensively investigated at the URL Mont-Terri with some 140 in situ experiments by sixteen research institutions from 8 countries /BOS 17a/b/. These experiments aim to characterize the clay rock, to test and demonstrate technologies for repository construction, waste emplacement, backfilling and sealing of the reminding openings, to understand and predict coupled processes and complex interactions in the multi-barrier disposal systems, and to estimate model parameters for safety assessment of the potential repositories. Figure 1.1 shows the geological structure of the URL.

At the URL location, the OPA formation can be divided into three layered lithological facies: 1) clay rich shaly facies – a dark grey silty calcerous shale and argillaceous marl in the lower half of the sequence; 2) sandy-carbonate rich facies – a grey sandy and argillaceous limestone in the middle of the sequence; and 3) sandy facies – silty to sandy marls with sandstone lenses cemented with carbonate in the upper part /THU 99/, /PEA 03/, BOS 17a/. Up to now, the clay-rich shaly facies has been extensively characterized with laboratory and in situ experiments /COR 07/, /NAU 07/, /POP 07/, /BOC 10/, /ZHA 07/13/, /MIN 17/, /AMA 15/17/, /BOS 17/, /MAR 17/, /WIL 15/17/18/, /FAV 18/ GIG 18/, /BÖH 18/, among others. Valuable knowledge about the thermo-hydro-mechanical (THM) properties and behaviour of the shaly facies has been obtained. In order to characterize the sandy and carbonate-rich facies for establishing a

robust mechanical database for the entire OPA formation, a new gallery 18 was planned in 2018 /SWI 18/ and constructed in 2019 within these facies (fig. 1.1a) for more in situ experiments. Before the URL extension, a laboratory program called LT-A experiments was launched by BGR and GRS to pre-investigate the hydro-mechanical behaviour of the sandy facies.

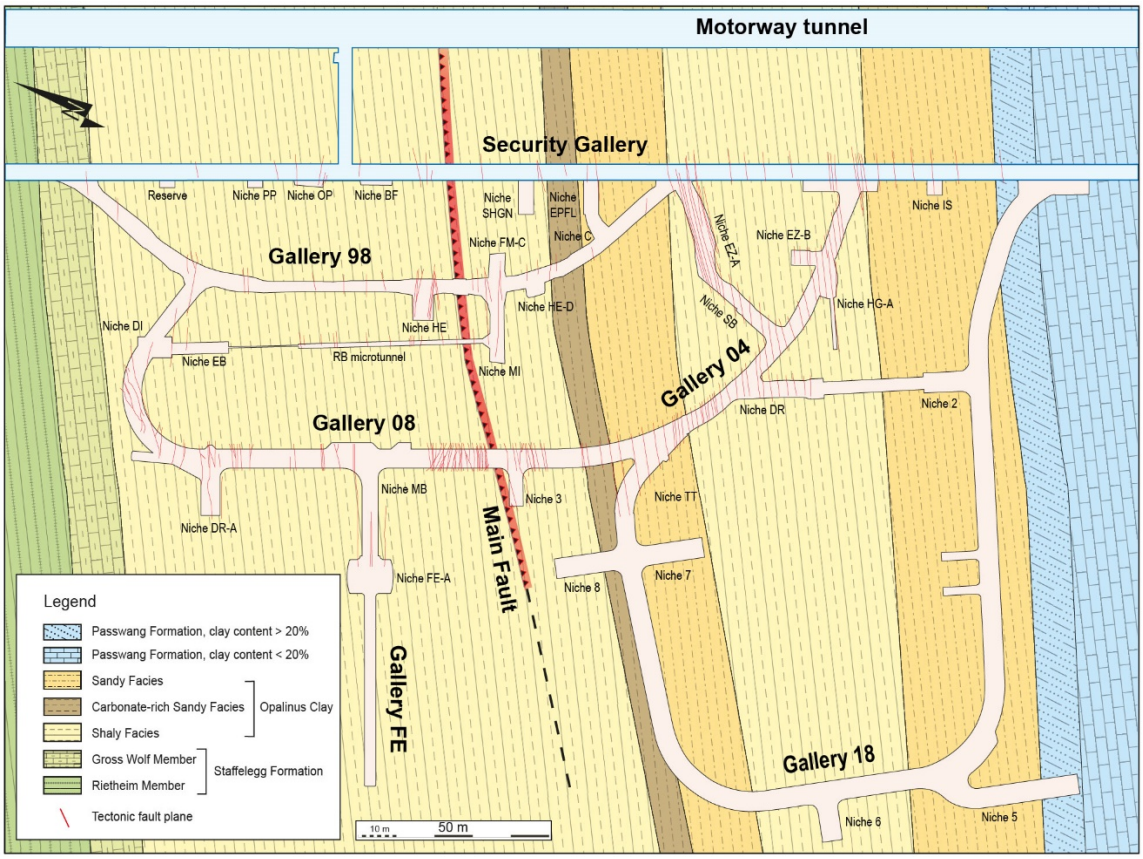

Fig. 1.1 Geological structure map and horizontal cross section of the Underground Rock Laboratory Mont-Terri (taken from Swisstopo, 2019)

A major safety concern in underground repositories is the excavation damage zone (EDZ). It develops around excavated openings and may reduce the barrier function of the host rock against water flow and radionuclide transport. As observed in the OPA at URL Mont-Terri /BOS 04/17a/ and in the similar Callovo-Oxfordian claystone (COX) at URL Bure in France /ARM 14/, DEL 15/, fractures are generated in the EDZ and the resulting permeabilities near drift walls are several orders of magnitude higher than that of the rock mass in the far-field. However, significant self-sealing of fractures was observed in laboratory tests of the clay-rich OPA shaly facies and the COX clay unit /BOC 10/, /ZHA 11/13/, /AUV 15/, /GUS 17/, /GIO 18/, as well as in the *in situ* EDZ /DEL 15/, /MAR 17/.

In order to characterize the mechanical properties and the behaviour of the sandy OPA facies, we performed different kinds of laboratory experiments. Our objectives are threefold, as we investigate a) mechanical deformation and damage under various load conditions during repository excavation and operation; b) moisture effects due to ventilation and water migration; and c) self-sealing of fractures under hydro-mechanical impact during a repository post-closure phase. This report presents our investigations on the mechanical behaviour (a) and moisture effects (b), while the self-sealing study (c) is still ongoing and will be reported in near future.

2 Characterization of the studied claystone

2.1 Sampling

The here investigated core samples derive from the air-drilled boreholes of 110 mm diameter in the sandy facies of OPA at URL Mont-Terri: BMB-A0, BDM-B9, BLT-A4, BLT-A8, BLT-A9, and BLT-A10. Figure 2.1 depicts the positions of the boreholes. Whereas BDM-B9 and BMB-A0 were drilled from the gallery 98 nearly parallel to bedding, the others were drilled from a niche of the gallery 04 parallel bedding (BLT-A4 & A8) and perpendicular to bedding (BLT-A9 & A10). Both locations are in a distance of about 60 meters. The drilled cores had a diameter of 100 mm and different lengths of cm - m scale, depending on material properties, homogeneity, drilling direction in relation to bedding planes, drilling techniques, and others. Figure 2.2 shows pictures of some drilled cores. The cores were cut in lengths of 250 – 500 mm.

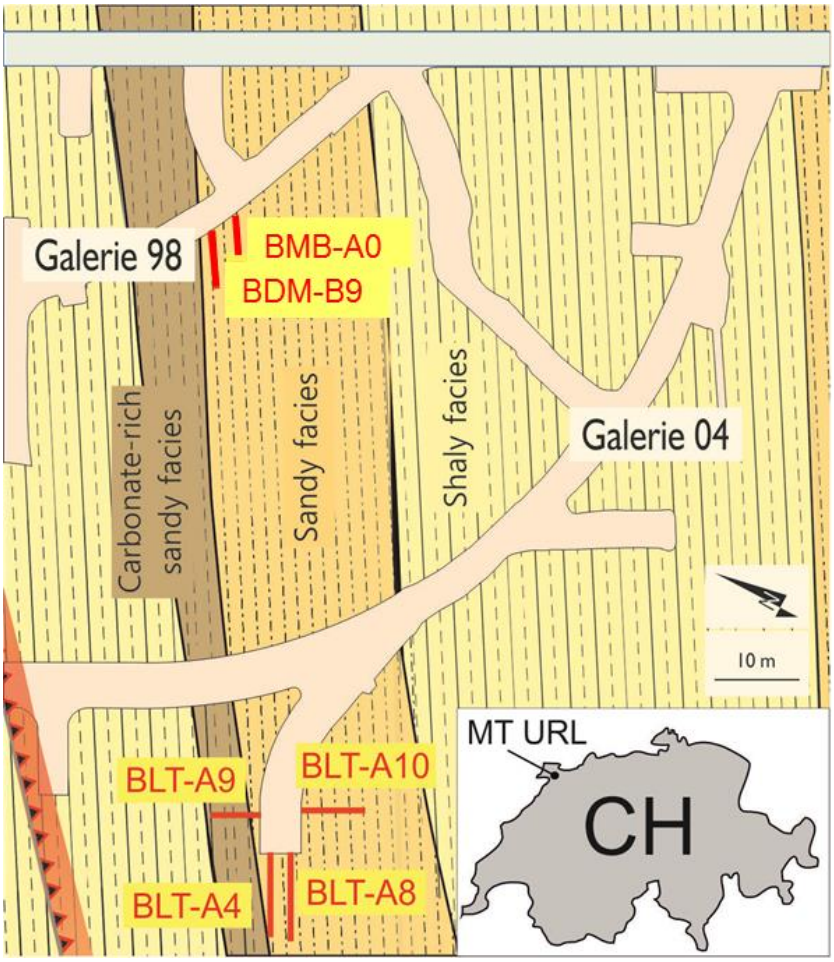

Fig. 2.1 Positions of boreholes drilled in the sandy facies of Opalinus Clay at URL Mont-Terri

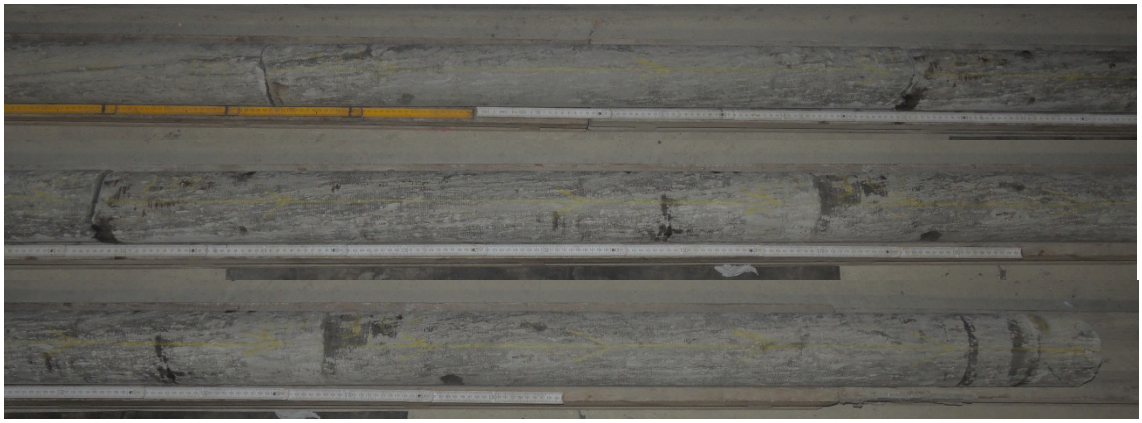

Cores from borehole BMB-A0

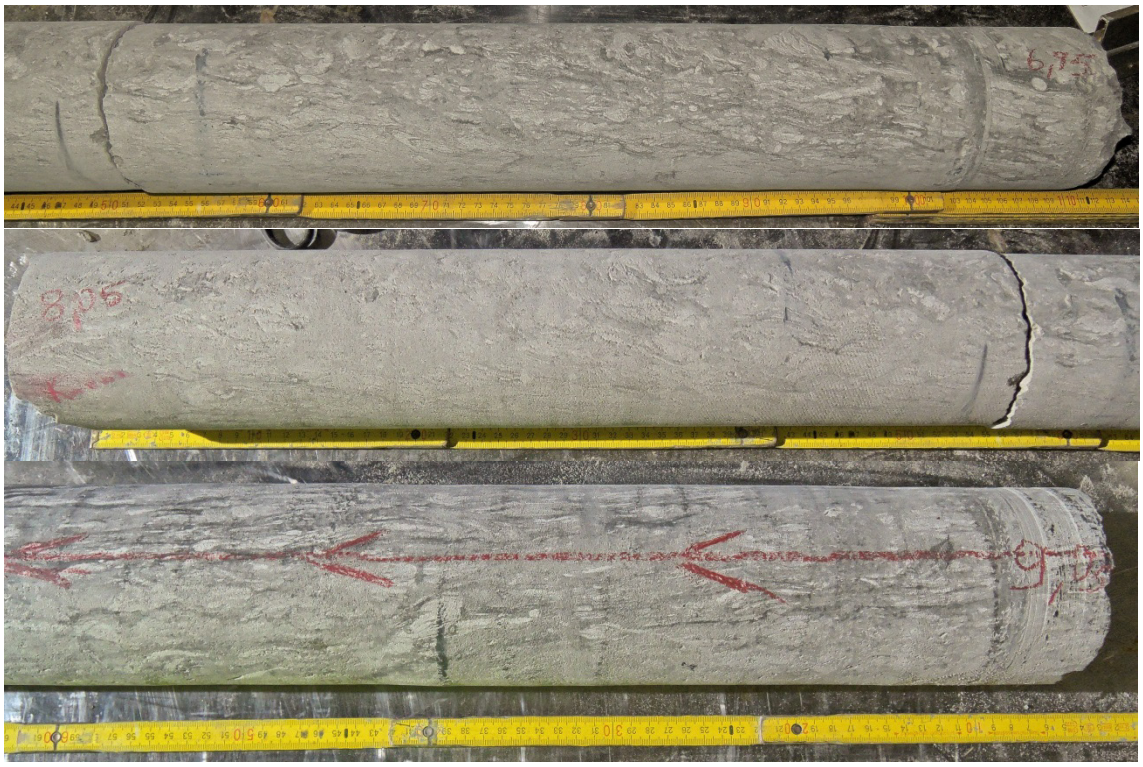

Cores from borehole BDM-B9

Fig. 2.2 Pictures of some drilled cores from boreholes BMB-A0 and BDM-B9 parallel to bedding

In order to hinder damage from unloading and desaturation, the cores were sealed in rubber jackets, then confined by pressing two parts of hard plastic tube on the jackets with two stretching steel bands as well as by forcing two plastic plates on the end faces with a stretching plastic band, and finally wrapped in vacuum-tight aluminium foil (Fig. 2.3). Some cores were sealed in vacuum-tight aluminium foil. The sealed samples were then stored in a climate-controlled room at 22 °C for several months to a year un-

til testing. From the cores, cylindrical samples were carefully prepared by cutting, smoothing and planishing the end faces in a lathe to three sizes of diameter/length D/L = 50/100, 70/140 and 100/200 mm for mechanical testing (fig. 2.3). Even though the sampling procedure was carefully conducted, the samples inevitably desaturated to some extend and a few visible micro-fissures appeared on the surface of some samples. These fissures occur mostly along the bedding planes. In the mechanical tests, For the mechanical testing the bedding foliation in the samples is in parallel orientation to the sample axis.

inserted in jacket | confined in cell | confined in cell | prepared to cylindrical sample in a lathe

Fig. 2.3 Pictures of the confinement, storage and preparation of test samples

2.2 Mineralogical composition

Table 2.1 lists the major mineralogical phases in samples from borehole BDM-B9, as found by X-ray diffraction with Rietveld quantification. The mineralogical composition displays a strong spatial variability: Within a 4 m interval, clays range from 24 – 41 %, quartz from 33 – 39 %, carbonates from 14 – 33 %, and feldspar from 8 – 9 %. This variability is in accordance with samples from borehole BLT-A2, which showed relative lower contents of clay minerals (20 – 25 %), similar contents of quartz (30 – 45 %) and carbonates (20 – 40 %) /KAU 11/. Compared to the shaly facies with clay minerals of 60 – 80 %, quartz of 10 – 27 % and carbonates of 4 – 35 % /THU 99/, /BOS 17a/, the sandy facies generally has much lower clay contents but more quartz and carbonates. Kaufhold et al. /KAU 13/16/ and Houben et al. /HOU 14/ demonstrated that the sandy facies is more heterogeneous on mm – cm scale than the shaly facies: The sandy facies comprises coarse-grained carbonate-rich lenses and exposes a smaller contribution of clay matrix (down to 32 % compared to max. 85 % in the shaly facies). In general, a material with high clay content is weaker than a material with a high abundance of hard

grains, e.g. /BAK 17 and /LUP 81/. This holds true for the shaly and the sandy facies. They expose a drastic difference in bedding parallel uniaxial strength of about 10 MPa versus 18 MPa, respectively, and in bedding perpendicular uniaxial strength of 7 MPa versus 16 MPa /JAE 17/. Similarly, stiffness of the sandy facies exceeds the shaly facies, exhibiting Young's Modulus of 12.6 GPa versus 7.4 GPa parallel to the bedding, and 3.6 GPa versus 2.4 GPa in perpendicular direction /VÖB 14/.

Tab. 2.1 Main mineralogical components of the sandy facies from borehole BDM-B9

Sample	Length (m)	Clay (%)	Quartz (%)	Carbonates (%)	Feldspar (%)	Pyrite (%)
B9-9	8.2	24	34	33	9	< 1
B9-17	10.2	41	37	14	8	< 1
B9-18	10.4	36	39	15	9	< 1
B9-19	10.6	26	33	32	9	< 1
B9-29	12.8	39	38	14	8	< 1

2.3 Petrophysical properties

2.3.1 Definitions

The petrophysical properties of all the samples were determined before testing, including grain density, bulk density, dry density, porosity, water content and saturation degree. According to ISRM (International Society for Rock Mechanics) suggested testing methods /ISR 81/, these properties are defined as follows:

Grain density: $\rho_s = \frac{M_s}{V_s}$ (2.1)

M_s = mass of solids, V_s = volume of solids.

Bulk density: $\rho_b = \frac{M}{V} = \frac{M_s + M_w}{V}$ (2.2)

M = mass of bulk sample, V = volume of bulk sample,

M_s = mass of solids, M_w = mass of water.

Dry density: $\rho_d = \frac{M_s}{V}$ (2.3)

Porosity: $\varphi = \frac{V_v}{V} = \left(1 - \frac{\rho_d}{\rho_s}\right)$ (2.4)

V_v = volume of voids.

Water content: $w = \frac{M_w}{M_s}$ (2.5)

Degree of water saturation:

$$S_w = \frac{V_w}{V_v} = \frac{\rho_d \cdot w}{\rho_w \cdot \varphi} = w \frac{(1-\varphi)}{\varphi} \frac{\rho_s}{\rho_w} \quad (2.6)$$

ρ_w = density of pore water.

2.3.2 Measured results

All the samples were characterised by the petrophysical properties. The bulk density was determined by measuring volume and weight of the sample after preparation. The water content was measured on 20 mm thick disks that were leftovers from the sample preparation. They were dried at a temperature of 105 °C for 2 days and subsequently checked for weight loss. The grain density was measured with a helium gas pycnometer on powder samples produced during sample preparation. Dry density, porosity and degree of water saturation are derived from the above measurements. Totally, more than 50 cylindrical samples were prepared and characterized for mechanical tests (tables 2.2/3/4/5) and 30 other ones for water uptake and swelling tests (tables 2.6/7).

Tab. 2.2 Characteristics of the samples from borehole BMB-A0 parallel to bedding for triaxial compression tests (sample size: D = 70 mm, L = 140 mm)

Group A Samples	Grain density ρ_s (g/cm^3)	Bulk density ρ_b (g/cm^3)	Dry density ρ_d (g/cm^3)	Porosity ϕ (%)	Water content w (%)	Saturation degree S_w (%)
A0-4/1	2.696	2.465	2.397	11.09	2.84	61.3
A0-5/1	2.688	2.458	2.384	11.31	3.12	65.7
A0-6/1	2.685	2.465	2.358	12.17	4.54	87.9
A0-7/1	2.688	2.466	2.373	11.73	3.95	80.0
A0-8/1	2.695	2.454	2.387	11.44	2.81	58.6
A0-9/1	2.688	2.478	2.403	10.59	3.10	70.3
A0-10/1	2.682	2.465	2.387	11.01	3.29	71.3
A0-11/1	2.682	2.451	2.382	11.19	2.89	61.4
A0-12/1	2.685	2.442	2.366	11.86	3.20	63.8
mean value	2.688	2.461	2.382	11.37	3.30	68.0
std. deviation	0.005	0.010	0.013	0.45	0.54	9.10

Group B Samples	Grain density ρ_s (g/cm^3)	Bulk density ρ_b (g/cm^3)	Dry density ρ_d (g/cm^3)	Porosity ϕ (%)	Water content w (%)	Saturation degree S_w (%)
A0-4/2	2.696	2.491	2.402	10.93	3.89	85.5
A0-5/2	2.688	2.460	2.343	12.83	5.24	95.8
A0-6/2	2.685	2.460	2.369	11.77	4.06	81.6
A0-7/2	2.688	2.480	2.400	10.71	3.49	78.1
A0-8/2	2.695	2.494	2.415	10.39	3.44	80.0
A0-9/2	2.688	2.477	2.381	11.41	4.21	87.9
A0-102	2.682	2.469	2.371	11.60	4.34	88.7
A0-11/2	2.682	2.452	2.356	12.15	4.29	83.2
A0-12/2	2.685	2.466	2.374	11.57	4.08	83.8
mean value	2.688	2.472	2.379	11.48	4.115	85.0
std. deviation	0.005	0.0135	0.0219	0.71	0.503	5.00

Tab. 2.3 Characteristics of the samples from borehole BMB-A0 parallel to bedding for triaxial extension tests (sample size: D = 50 mm, L = 100 mm)

Samples	Grain density ρ_s (g/cm^3)	Bulk density ρ_b (g/cm^3)	Dry density ρ_d (g/cm^3)	Porosity ϕ (%)	Water content w (%)	Saturation degree S_w (%)
for TEM tests at constant mean stress						
A0-3/3	2.683	2.415	2.348	12.48	2.77	52.1
A0-4/3	2.696	2.457	2.376	11.87	3.30	66.1
A0-5/3	2.688	2.442	2.362	12.14	3.30	64.2
A0-6/3	2.685	2.437	2.358	12.18	3.25	62.9
A0-7/3	2.688	2.464	2.384	11.30	3.25	68.5
for TEA tests at constant axial stress						
A0-8/3	2.695	2.457	2.388	11.40	2.81	59.0
A0-9/3	2.688	2.459	2.380	11.46	3.24	67.3
A0-10/3	2.682	2.432	2.353	12.28	3.25	62.3
A0-11/3	2.682	2.418	2.343	12.65	3.11	57.6
A0-12/3	2.685	2.434	2.382	11.28	2.13	45.9
mean value	2.687	2.442	2.367	11.90	3.04	61.0
std. deviation	0.005	0.017	0.016	0.48	0.35	7.0

Tab. 2.4 Characteristics of the samples from borehole BDM-B9 parallel to bedding for triaxial cyclic compression tests (sample size: D = 70 mm, L = 140 mm)

Sample	Dry density ρ_d (g/cm³)	Porosity ϕ (%)	Water content w (%)	Saturation degree S_w (%)	Conditioning at RH (%)
B9-1	2.345	13.14	5.49	98.0	100
B9-3	2.358	12.66	4.92	91.6	100
B9-4	2.323	13.95	6.00	99.9	100
B9-15	2.356	12.73	4.93	91.3	100
B9-6	2.525	6.47	1.70	66.5	no
B9-9	2.502	7.33	2.52	86.2	no

Tab. 2.5 Initial characteristics of the samples for creep tests

Test group	Sample	Size D/L (mm)	Bulk density ρ_b (g/cm³)	Dry density ρ_d (g/cm³)	Porosity ϕ (%)	Water content w (%)	Degree of saturation S_w (%)
Triaxial creep							
1	BLT-A8	99/190	2.566	2.487	8.31	3.10	92.8
2	BDM-B9-11	70/140	2.479	2.454	9.11	1.01	27.0
	BDM-B9-12	70/140	2.556	2.465	9.70	3.56	98.5

Tab. 2.6 Initial characteristics of the samples (D = 70 mm, L = 20 mm) for measurement of water retention and volume change at different humidities

Group A Samples	Borehole depth (m)	Bulk density ρ_{bo} (g/cm^3)	Dry density ρ_{do} (g/cm^3)	Porosity ϕ_o (%)	Water content w_o (%)	Water saturation S_{wo} (%)
B9-1a	6.21	2.439	2.357	12.71	3.36	62.33
B9-2a	6.45	2.431	2.335	13.51	3.93	67.88
B9-3a	6.71	2.432	2.341	13.30	3.75	66.02
B9-4a	6.94	2.476	2.395	11.30	3.28	69.55
B9-5a	7.28	2.531	2.470	8.51	2.39	69.35
B9-6a	7.53	2.569	2.517	6.77	2.03	75.51
B9-7a	7.78	2.561	2.525	6.48	1.40	54.55
B9-8a	8.06	2.568	2.523	6.57	1.77	68.10
average	7.00	2.501	2.433	9.89	2.74	66.66

Group B Samples	Borehole depth (m)	Bulk density ρ_{bo} (g/cm^3)	Dry density ρ_{do} (g/cm^3)	Porosity ϕ_o (%)	Water content w_o (%)	Water saturation S_{wo} (%)
B9-1b	6.22	2.446	2.370	12.24	3.11	60.13
B9-2b	6.47	2.430	2.330	13.71	4.12	70.11
B9-3b	6.72	2.445	2.356	12.72	3.63	67.24
B9-4b	6.95	2.453	2.378	11.92	3.06	60.98
B9-5b	7.29	2.518	2.454	9.11	2.53	68.28
B9-6b	7.54	2.562	2.516	6.81	1.79	66.31
B9-7b	7.79	2.578	2.540	5.91	1.47	63.32
B9-8b	8.07	2.566	2.522	6.60	1.71	65.22
average	7.00	2.500	2.433	9.88	2.68	65.20

Group C Samples	Borehole depth (m)	Bulk density ρ_{bo} (g/cm^3)	Dry density ρ_{do} (g/cm^3)	Porosity ϕ_o (%)	Water content w_o (%)	Water saturation S_{wo} (%)
B9-26a	12.13	2.548	2.503	7.30	1.78	60.94
B9-26b	12.14	2.523	2.469	8.57	2.16	62.13
B9-26c	12.15	2.511	2.463	8.79	1.95	54.54
B9-26d	12.16	2.536	2.481	8.12	2.17	66.35
B9-27a	12.30	2.558	2.498	7.49	2.34	77.98
B9-27b	12.31	2.535	2.486	7.94	1.95	61.16
B9-27c	12.32	2.534	2.477	8.27	2.25	67.35
B9-27d	12.33	2.529	2.482	8.09	1.88	57.67
average	12.20	2.534	2.482	8.07	2.06	63.51
Average over all samples		2.512	2.449	9.28	2.49	65.13

Tab. 2.7 Average characteristics of the samples from boreholes BLT-A8/9/10 for measurement of water retention

Sample	Borehole depth (m)	Grain density (g/cm^3)	Bulk density (g/cm^3)	Dry density (g/cm^3)	Porosity (%)	Water content (%)	Water saturation (%)
OPA-BLT-A8	3.73	2.705	2.540	2.517	6.9	0.9	32.6
OPA-BLT-A9	1.12	2.705	2.530	2.497	7.7	1.3	42.2
OPA-BLT-A10	6.79	2.705	2.500	2.400	11.3	4.0	85.1

Tab. 2.8 Characteristics of the reconditioned samples from borehole BMB-B9 parallel to bedding for testing moisture effects on uniaxial deformation and strength (sample size: D = 70 mm, L = 140 mm)

Sample	Dry density ρ_d (g/cm^3)	Porosity ϕ (%)	Water content w (%)	Saturation degree S_w (%)	Conditioning at RH (%)
B9-8	2.50	7.3	0.64	22.0	30
B9-14	2.40	11.3	0.78	30.9	50
B9-7	2.55	5.5	1.46	36.6	70
B9-5	2.44	9.5	3.60	92.7	93
B9-16	2.41	10.7	4.31	97.3	100

The data of grain density, dry density, water content and saturation degree are depicted in figs. 2.4 to 2.7 along borehole length. The grain density is relatively constant at ρ_s = 2.69±0.012 g/cm^3 (fig. 2.4), which is consistent with the data obtained on the OPA sandy facies from literature /YU 17/. The results from /YU 17/ also show marginal differences of the grain densities between the sandy and shaly facies in a range of 2.69 - 2.71 g/cm^3, which are also comparable to that of COX claystone /ZHA 19/. Whereas the dry density and porosity along borehole BMB-A0 are relatively constant at ρ_d = 2.37±0.027 g/cm^3 and ϕ = 11.7±1.30 % (fig. 2.5a), they vary largely along borehole BDM-B9 (fig. 2.5b). The dry density increases dramatically from ρ_d = 2.33 g/cm^3 to 2.53 g/cm^3 in the small distance of 6 to 8 m and the corresponding porosity drops from ϕ = 13.5 % down to 6.5 %. This illustrates a significant heterogeneity of the claystone in this borehole. Similarly, the water contents measured on the samples from borehole BMB-A0 vary in a small range around w = 3.12±0.45 % and the corresponding saturation degrees are S_w = 63.0±10.0 % (fig. 2.6a). The data obtained on the samples from borehole BDM-B9 indicate a significant decrease in water content from w ≈ 4.0 % at L ≈ 6 m down to w ≈ 1.8 % at L ≈ 8 m (fig. 2.6b), in correlation to the decrease in porosity (fig. 2.5b). The higher porosity samples contain more water. The corresponding degrees of water saturation are quite similar at S_w = 65±10 % along the borehole. The results indicate a remarkable desaturation of the samples due to coring, storage and preparation.

In order to recover the natural water content in the claystone, resaturation was carried out by wetting some samples in humid air at relative humidity of ~100 % for 1.5 – 2.5 months. Figure 2.7 shows the wetting results of the samples BMB-A0 in group B with a dimeter of 70 mm and a length of 140 mm (table 2.2). The wetting over 1.5 months increased the water content from the initial mean value of w_o = 3.1 % to a high mean level of w_r = 4.1% and the corresponding saturation degree from S_{wo} = 68 % to S_{wr} = 85 %. Higher saturation degrees of 92 – 99 % were achieved for a longer wetting duration of 2.5 months (tables 2.4 and 2.6). It needs to be pointed out that the wetting resulted in some swelling of the unconfined samples and hence in changes of the measured volumes used in equations 1 to 6. For instance, sample BDM-B9-12 with an initial size of D/L = 70/140 mm and an initial water content of 2.23 % was rewetted at RH = 100 % over 2.5 months, resulting in an increase in water content by 1.33 % and swelling to an axial strain of 0.3 % and a radial strain of 0.4 %. The radial swelling normal to bedding is relatively larger due to more opening of the bedding planes, which can even generate visible cracks along bedding planes, especially when over saturated for a longer time, as observed on another unconfined sample rewetted at RH = 100 % over 6 months in Fig. 2.8. We therefore propose a new fracture type, where bedding parallel cracks form due to locally inhomogeneous swelling, instead of the well-known fracture generation by desiccation and unloading /HOU 14/. In order to minimize the swelling effects, claystone samples have to be hydrostatically recompressed for mechanical testing /CON 18/, /ZHA 19/. A few samples that were significantly damaged due to swelling were not used for the mechanical testing here.

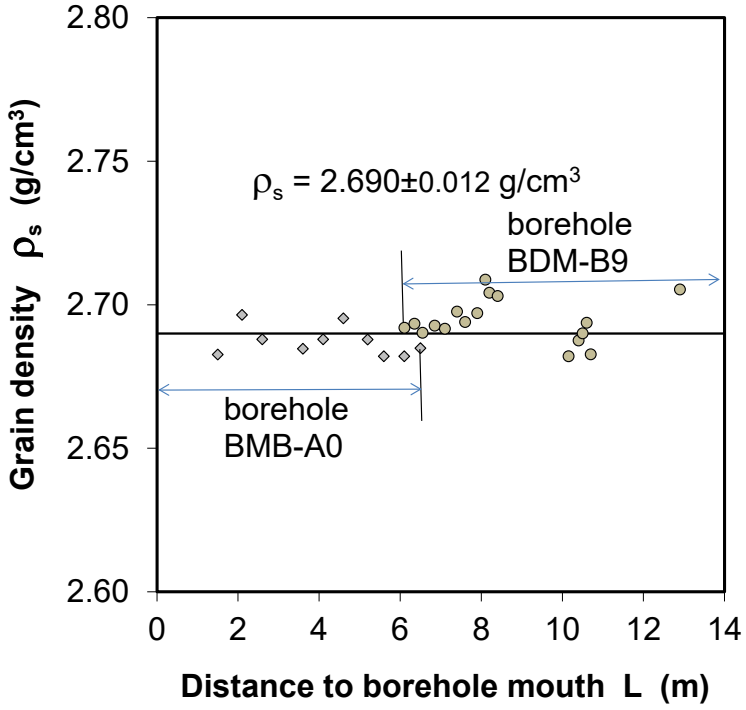

Fig. 2.4 Distributions of grain density along borehole length for boreholes BMB-A0 and BMB-B9

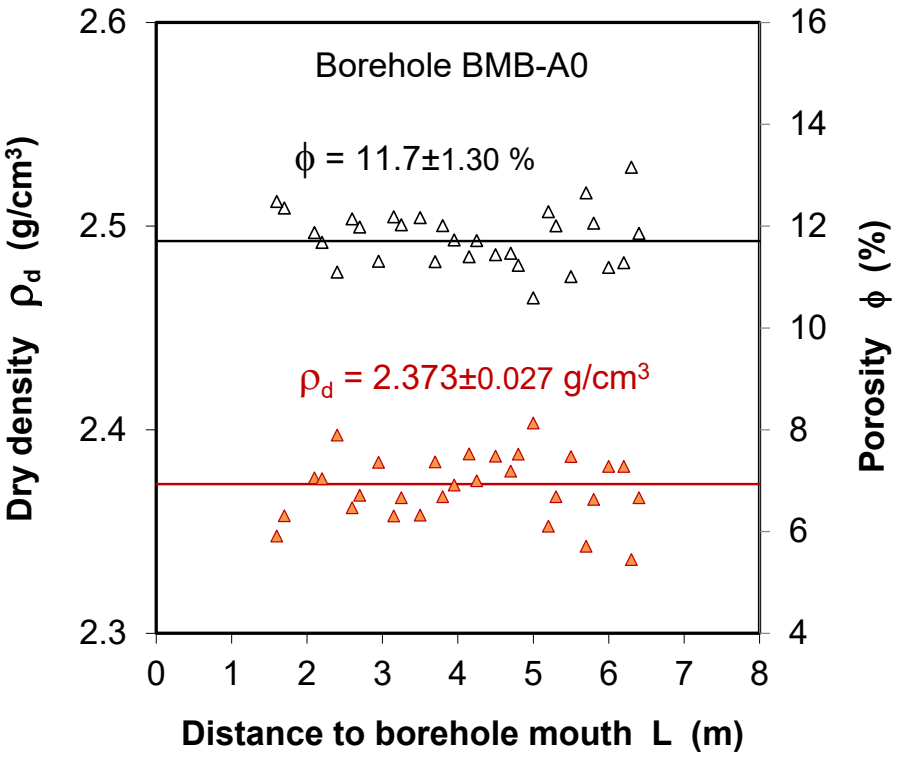

a. Borehole BMB-A0

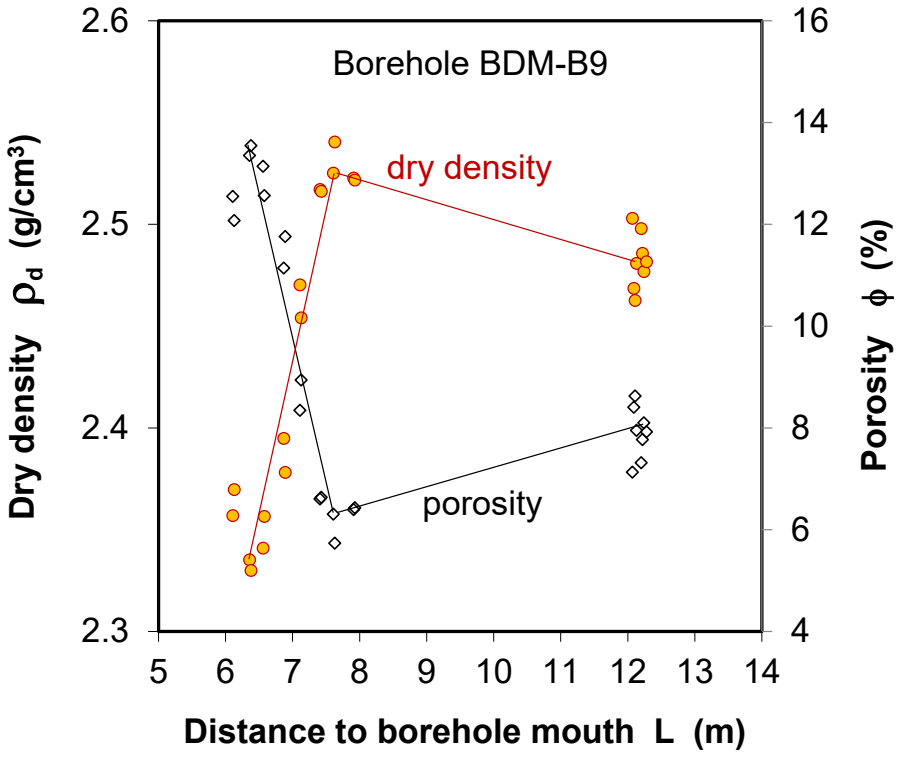

b. Borehole BDM-B9

Fig. 2.5 Distributions of dry density and porosity along borehole length for boreholes BMB-A0 and BDM-B9

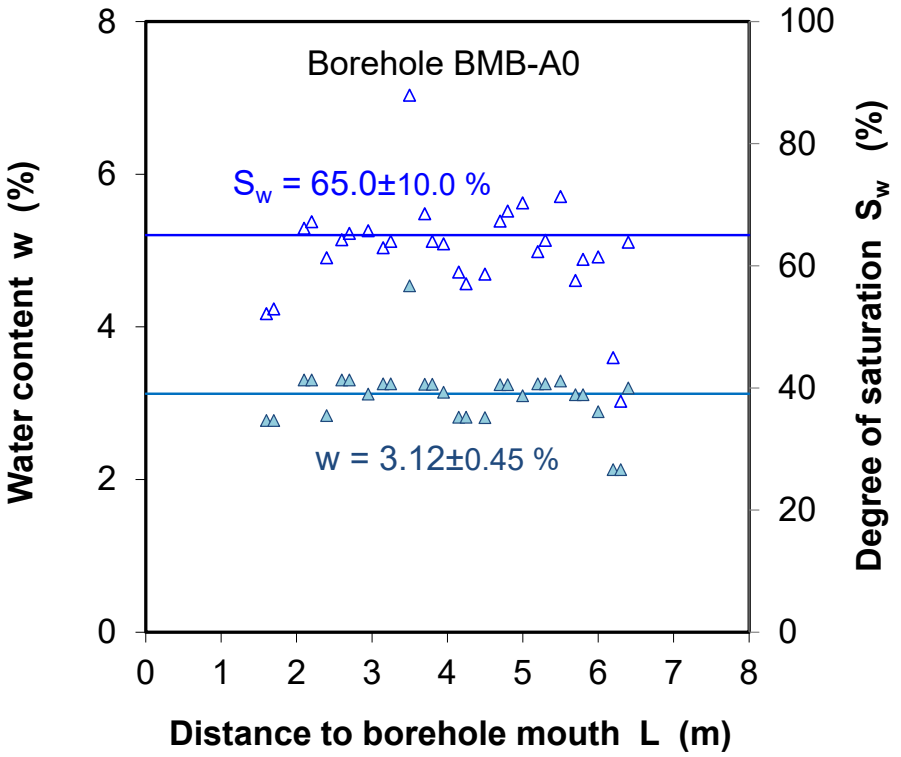

a. Borehole BMB-A0

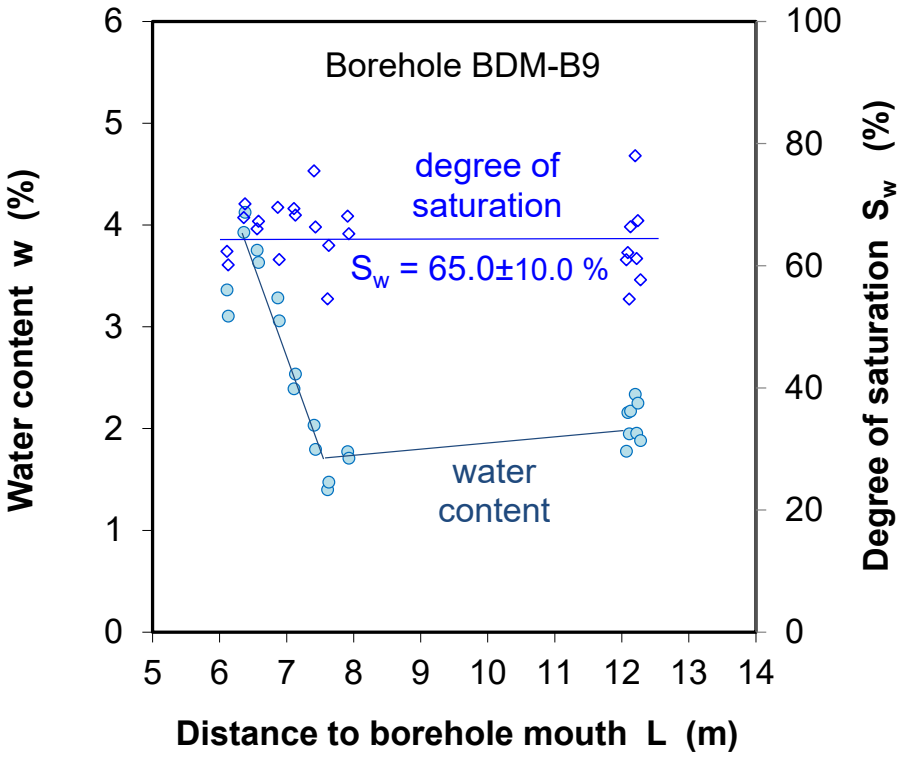

b. Borehole BDM-B9

Fig. 2.6 Distributions of water content and saturation degree along borehole length for boreholes BMB-A0 and BDM-B9

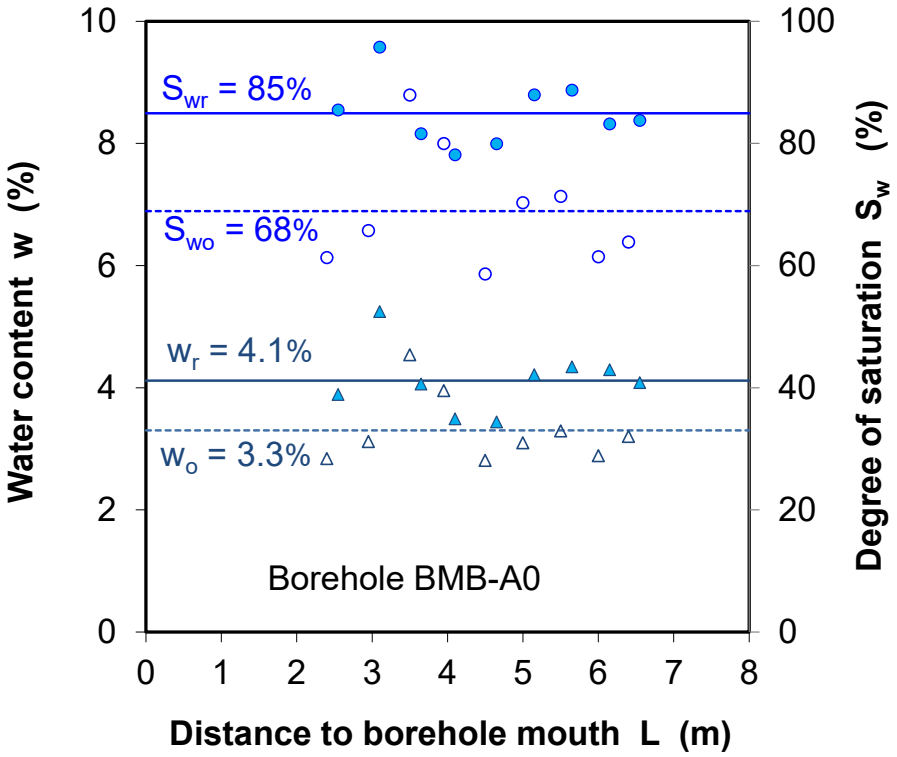

Fig. 2.7 Comparison of water content and saturation degree of the samples in the initial conditions (w_o, S_{wo}) and after resaturation (w_r, S_{wr}) at 100 % relative humidity over 1.5 months

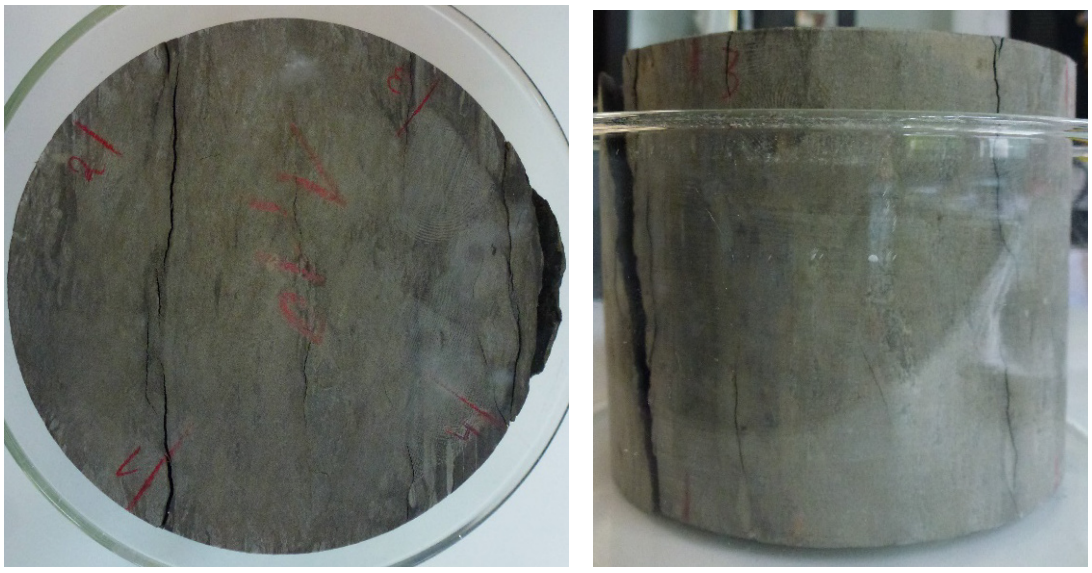

Fig. 2.8 Wetting-induced cracks along bedding planes in an unconfined sample (diameter = length = 100 mm) at relative humidity of 100 % over 6 months

3 Mechanical deformation and strength

3.1 Experimental methodology

Laboratory testing to characterize the mechanical behaviour of low-permeability claystone is a big challenge due to a high sensitivity of the material to unloading and humidity change by coring and sampling (induced desaturation, shrinkage, micro-fissures), chemical interactions with water and resulting effects (swelling, weakness and damage), and due to strong hydro-mechanical coupling effects (variations in pore pressure and effective stress). Specific testing techniques and procedures are required with careful sampling and reconditioning, measurements of stress, strain and pore pressure, reconsolidation to minimize effects of sampling-induced micro-fissures, and others /MEN 15/, /WIL 17/18/, /BEL 18/, /CON 18/, /EWY 18/, /GIG 18/, /ZHA 13/19/.

One of the technical challenges is to measure or control porewater pressure during mechanical loading. Usually, the porewater pressure of a sample is measured by the pressure in external reservoirs at the sample ends. However, it is still questionable whether the water pressure measured in the reservoirs is representative of the porewater pressure inside the sample and how the internal structure of the claystone is affected by contact with the external water. For the porewater pressure measurement, test conditions must be well controlled. For instance, claystone samples must be fully saturated; the pressure in the reservoirs must be steadily in equilibrium with the porewater pressure during testing; swelling of the samples is not allowed to avoid alteration of the internal structure of the material; and the volume of the reservoir must be fully saturated and maintain constant. These conditions are hardly met in laboratory tests. As mentioned earlier, some desaturation of claystone samples is unavoidable due to coring, storage and preparation. The samples usually need to be resaturated in humid environment and by injecting formation water. As contacting to water, however, the claystone is going to swell, even under high confining stresses as observed on COX claystone under the lithostatic stresses of 12 – 15 MPa and porewater pressure of 4.5 MPa at the sampling location URL Bure /ZHA 13/. Therefore, any water injection to claystone samples shall be avoided for mechanical testing due to swelling-induced alteration of the internal structure /CON 18/, /ZHA 19/.

For this among other reasons, our tests were conducted in drained and undrained conditions without introducing water to the samples and without monitoring porewater pressure. As consequence, the tests can only be analyzed by adopting total stress instead of effective one. It is to be pointed out here that the effective stress in indurated clay rock is partly transferred by bound porewater in interlayers and interparticle narrow pore space between clay particles /HOR 96/. This was evidenced by Zhang /ZHA 17a/b/ with various kinds of experiments for COX and OPA claystones, which demonstrated that if not total, most of the bound porewater in these claystones is supporting the lithostatic stresses and even bearing deviatoric stresses up to the material strength. Hence, the total stress applied to the claystone samples might be equivalent to the effective one. For the drained tests, we regard the bound porewater pressure to be equivalent to the effective stress and the pressure of mobile water in relatively large pores to be at atmospheric state. For the undrained tests on the partly saturated samples, we speculate that some water in saturated pores could be expelled into unsaturated space during mechanical loading. The pressure of the mobilizing porewater may be very low before fully saturated.

The main purpose of our tests is to investigate effects of load paths on the deformation and strength behavior of the OPA sandy facies with the large number of samples (tables 2.2 – 2.5). Additionally, effects of water saturation on the mechanical properties are also examined with two groups of the samples with different saturation degrees (table 2.2): group A as received with average saturation degree of S_w = 68 % and group B rewetted to S_w = 85 %.

Figure 3.1 shows schematic layouts of undrained and drained triaxial tests. For the samples in tables 2.2, 2.3, and 2.6, the so-called undrained condition was applied by sealing the samples in rubber jackets and covered at the top and bottom with load pistons (Fig. 2.9b). The samples in tables 2.4 and 2.5 were tested in drained condition (Fig. 2.9c), where the sample ends were covered with metallic porous discs connected to long tubes to keep atmospheric pressure. The porewater can be expelled by compression into the porous discus without rising backpressure at the sample ends. All the samples with the different sizes were loaded in several triaxial cells with controlled strain or stress rates. During loading, axial strain (ε_a) is recorded by linear variable displacement transducers (LVDT) installed inside the cell along the sample length, while radial strain (ε_r) is measured by a circumferential extensometer chain mounted around the sample outside the jacket. The volumetric strain is obtained approximately by $\varepsilon_v = \varepsilon_a + 2\varepsilon_r$ for small strains.

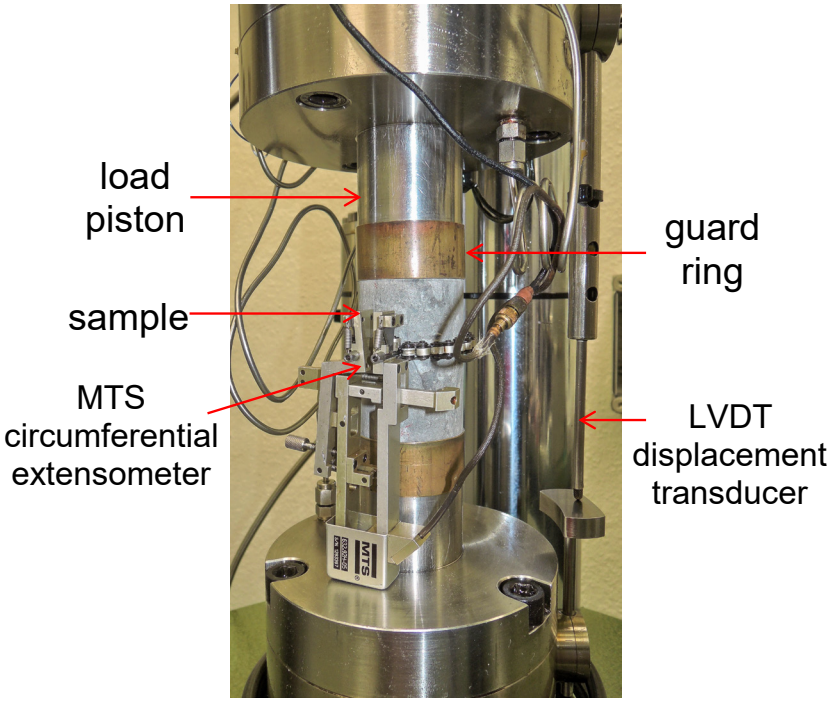

a. test setup

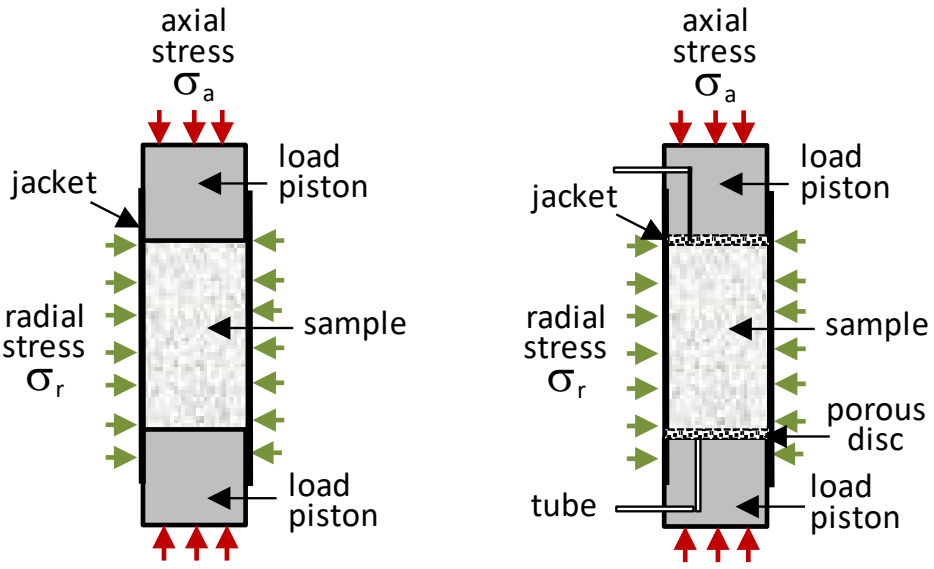

b. undrained condition c. drained condition

Fig. 3.1 Assemble of sample for triaxial testing (a) under undrained (b) and drained (c) conditions

3.2 Load paths

A basic principle of laboratory mechanical testing of rock to obtain data for design of underground openings is that the load boundary conditions applied to the test samples should simulate those imposed on the rock element *in situ*. This can rarely be achieved /BRA 06/. Most of the mechanical tests are carried out in triaxial compression, i.e. the

sample becomes shorter. But an underground excavation results in various kinds of stress paths and states around the openings, mostly dominated by extension in the near regions /CRI 98/, /BRA 06/. As shown by numerical modelling of drift excavation, for instance, in the shaly facies of OPA at URL Mont-Terri /ZHA 07/, the radial stress normal to the opening wall is decreased while the vertical and horizontal stresses are increased after excavation. Consequently, the rock extends in radial direction towards the opening. In order to simulate the the prevailing in situ stress conditions using triaxial testing apparatus, several different load paths were designed and applied to the samples, as illustrated in figure 3.2.

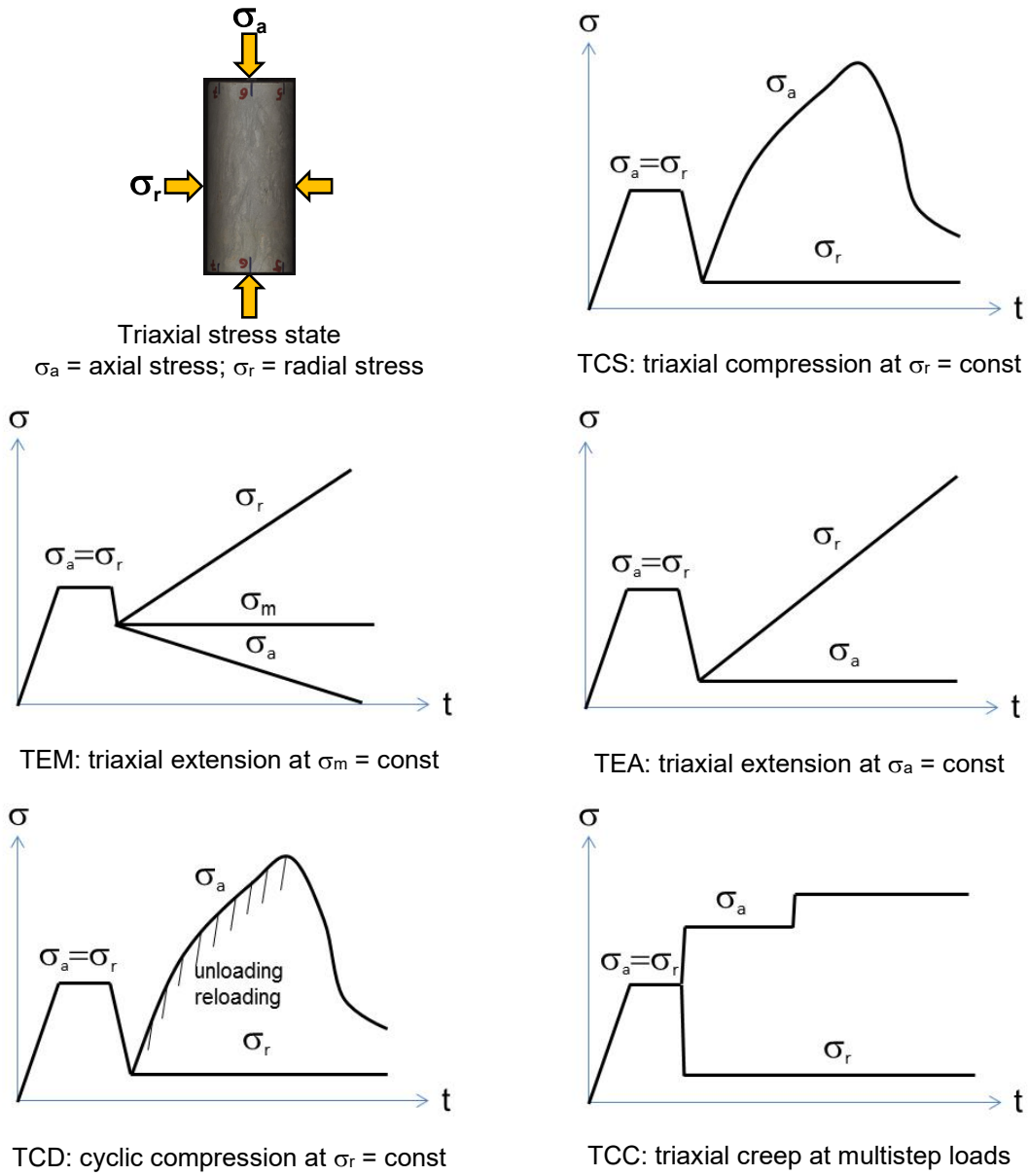

Triaxial stress state
σ_a = axial stress; σ_r = radial stress

TCS: triaxial compression at σ_r = const

TEM: triaxial extension at σ_m = const

TEA: triaxial extension at σ_a = const

TCD: cyclic compression at σ_r = const

TCC: triaxial creep at multistep loads

Fig. 3.2 Load paths applied in mechanical testing of the OPA sandy claystone

The tests were generally performed in two steps with hydrostatic pre-compaction followed by deviatoric stressing. The pre-compaction aimed to minimize effects of micro-fissures induced by sampling, which was performed at a load rate of $7 \cdot 10^{-3}$ MPa/s up to an isostatic stress of 15 MPa and kept for a duration of 15 – 20 hours. Based on the maximum burial of approximately 1350 m /MAZ 07/, the pre-compaction stress corresponds approximately to the maximum effective stress (the maximum overburden pressure of about 30 MPa – porewater pressure of about 13.5 MPa). Thus, the pre-compaction should not cause drastic (if any) over-consolidation of the claystone matrix but the closure of micro-fissure artefacts. After unloading to a desired level, subsequent deviatoric loading was conducted with regard to five respective load paths and their scientific objectives:

1) Investigation of effects of different load paths on short-term deformation and strength with respect to excavation
   - compression by increasing axial stress σ_a at constant radial stress σ_r (TCS)
   - extension at constant, *in situ* resembling mean stress $\sigma_m = (\sigma_a+2\sigma_r)/3$ (TEM) by simultaneously increasing radial stress σ_r and decreasing axial stress σ_a to determine extensional deformation and strength of the rock
   - extension by increasing radial stress σr at constant axial stress σ_a (TEA) to resemble conditions at the opening wall
2) Investigation of elastic parameters under different loads by cyclic axial compression ε_a at constant radial stress σ_r (TCD)
3) Investigation of time effects on deformation and strength by creep under multistep constant stress states, σ_a = const. and σ_r = const. (TCC).

3.2.1 Triaxial compression

The triaxial compression tests (TCS) were conducted on 18 samples in two groups from borehole BMB-A0 (table 2.2). Group A consisted of 9 samples without reconditioning and hence relatively low saturation degrees of S_w = 68±9 %, while the other 9 samples in group B had been rewetted to higher saturation degrees of S_w = 85±5 %. All the samples were loaded at an axial strain rate of $7 \cdot 10^{-7}$ s^{-1} under different radial stresses of σ_r = 0.5 to 10 MPa. The strain rate is the same order of the low strain rates of

10^{-6} - 10^{-8} s^{-1} applied in the undrained tests on claystones (e.g. /WIL 17/, /EWY 18/, /GIG 18/) in order to ensure dissipation of porewater pressure throughout the sample. The identical load conditions applied allow identification of effects of water saturation of the samples with and without rewetting.

3.2.2 Triaxial extension

The triaxial extension tests (TEM and TEA) were carried out on 9 samples from the same borehole BMB-A0 (table 2.3). Without reconditioning, their saturation degrees of S_w = 61±7.0 % were relatively low because they had been exposed to air in a longer preparation phase. Extensional loading (TEM) was conducted by simultaneously increasing radial compression at a rate of $3.5 \cdot 10^{-3}$ MPa/s and axial tension load at $7 \cdot 10^{-3}$ MPa/s and at respective mean stress σ_m = 15, 16, 18 and 20 MPa. Contrary, the TEA loads were applied by increasing the radial compression stress at a rate of $7 \cdot 10^{-3}$ MPa/s during various constant axial stresses of σ_a = 1, 2, 3, 5 and 8 MPa, respectively. The loading rate is comparable to the strain rate in the TCS tests.

3.2.3 Triaxial cyclic compression

The cyclic compression tests (TCD) are designed to examine variations of the rock elasticity with loading and deformation in drained condition. The tests were conducted on six samples from borehole BDM-B9 (table 2.4). Four samples were rewetted to high saturation degrees of S_w = 91 – 100 %, whereas the other two without wetting remained at relatively low saturation degrees of S_w = 66 – 86 %. The deviatoric loading was conducted by cyclically increasing axial compression at constant radial stress of σ_r = 1 to 5 MPa. The multiple loading-unloading cycles were performed at a constant axial strain rate of $7 \cdot 10^{-7}$ s^{-1}, which is the same order of the low strain rates of 10^{-6} – 10^{-8} s^{-1} applied in the drained tests on claystones (e.g. /BEL 18/, /EWY 18/, /GIG 18/, /WIL 18/) in order to avoid excess pore pressure during compression. Each cycle was limited in a range of $\Delta\sigma_a$ = -4 MPa for unloading and $\Delta\sigma_a$ = 6 MPa for uploading, corresponding to stress increments of 2 MPa. From the load cycles one can determine elastic parameters at different load conditions, namely Young's modulus E and Poisson's ratio ν, by

$$E = \frac{\Delta\sigma_a}{\Delta\varepsilon_a} \tag{3.1}$$

$$\nu = -\frac{\Delta\varepsilon_r}{\Delta\varepsilon_a} \tag{3.2}$$

where $\Delta\varepsilon_r$ and $\Delta\varepsilon_a$ represent the radial and axial strain changes in each loading cycle. The Poisson's ratio is an average of the response in the direction perpendicular and parallel to the bedding. For a complete description of the elastic behavior of the transversely isotropic material, five independent elastic parameters are needed and will be determined in the next program by adopting the test methodology for the COX claystone in /ZHA 19/.

3.2.4 Triaxial creep

In order to examine time effects on deformation and strength of the claystone, triaxial creep tests (TCC) were carried out on two highly-saturated and one dried sample in undrained conditions over months to years. Their initial characteristics are given in table 2.6. Before testing, sample BLT-A8 (D/L = 99/190 mm) and BDM-B9-12 (D/L = 70/140 mm) were rewetted at RH = 100 % over 2.5 months to high saturation degrees of S_w = 93 % and S_w = 98.5 % respectively, while BDM-B9-11 (D/L = 70/140 mm) was dried to a low saturation degree of S_w = 27.0 %.

The sample BLT-A8 was tested in a triaxial creep rig (Fig. 3.3), which allows a maximum axial stress σ_a of 70 MPa and a lateral pressure σ_r of 50 MPa with an accuracy of better than ±0.02 MPa (< 0.05 % of the maximum) and a maximum temperature of 150 °C within a fluctuation range of ±0.1 °C. Multistep deviatoric stresses were applied by keeping a mean stress of $\sigma_m = (\sigma_a + 2\sigma_r)/3$ = 13 MPa. Both axial and radial strains were measured on the sample by a displacement transducer (LVDT) installed inside the cell along the sample length and a circumferential extensometer mounted around the sample outside the jacket, respectively. This apparatus is also equipped with an ultrasonic device for detecting sample damage and a hydraulic system for monitoring fluid flow through the sample. But this test on sample BLT-A8 was conducted at temperature of 27.5 °C and in undrained conditions without measuring pore pressure and wave velocity.

The two other tests on samples BDM-B9-11 and -12 with different saturation degrees were conducted in a coupled triaxial creep rig which allows testing two samples simultaneously (fig. 3.4). The samples were placed in two separated chambers and simultaneously loaded at same axial and radial stresses by means of three precise syringe pumps (Model 260D). One was for the identical axial load on both samples and the other twos for the separate radial pressure in each cell. The pumps can be controlled up to a maximum volume of 260 mL and a maximum pressure of 50 MPa. The resolution of the pressure is about 0.01 MPa. Axial displacement of each sample was measured by means of two LVDT deformation transducers outside the cell. Unfortunately, radial strain could not be monitored in this rig. Identical multistep stresses were applied to both samples by keeping a mean stress of σ_m = 13 MPa and at temperature of 26 °C.

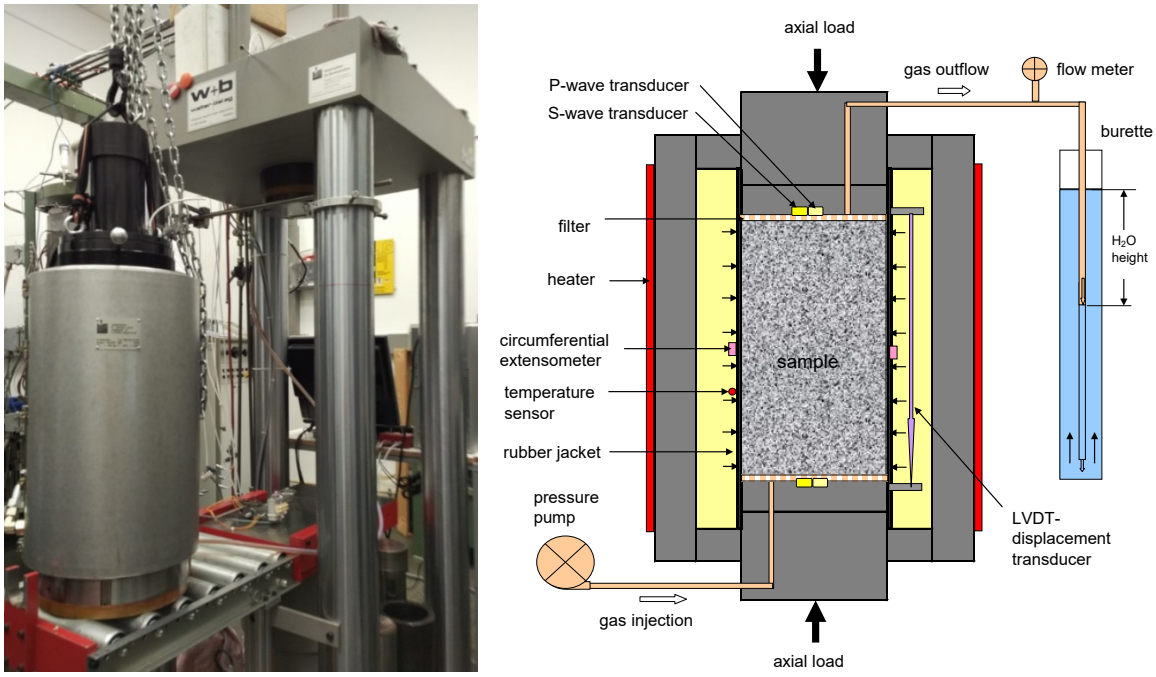

Test setup Test layout

Fig. 3.3 A triaxial testing system with thermo-hydro-mechanical control and measurements of deformation, permeability, and ultrasonic wave velocity

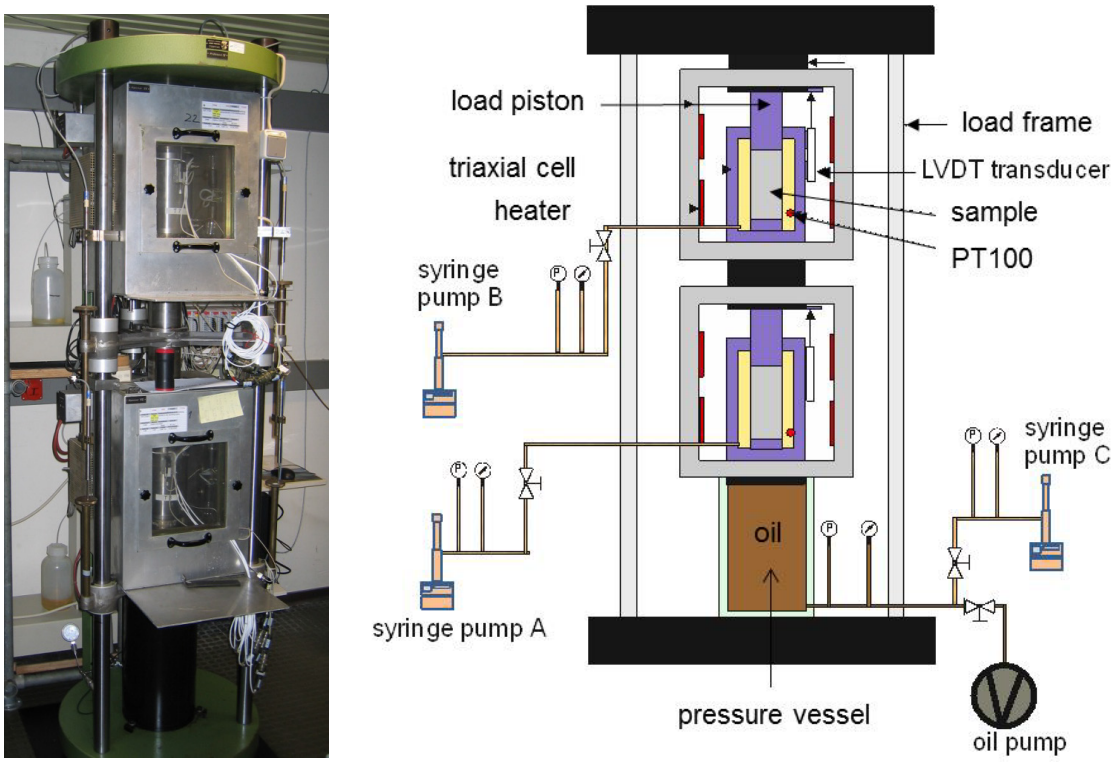

Fig. 3.4 A coupled rig for triaxial creep testing on two samples one upon another

3.3 Results and discussions

3.3.1 Triaxial compression

3.3.1.1 Pre-compaction

Figure 3.5 shows typical results of the pre-compaction obtained on a non-wetted sample BMB-A0-7/1 with saturation degree S_w = 80 % (a) and another rewetted sample BMB-A0-5/2 with S_w = 96 % (b) under isostatic stress of σ_m = 15 MPa for 15 and 18 hours respectively. The axial, radial and volumetric strains are illustrated versus the elapsed time and applied isostatic stress. The isostatic load led to a compaction in all directions. Even though the sample axis was parallel to the bedding, most of the non-wetted samples exhibited quasi-isotropic compaction with similar axial and radial strains, $\varepsilon_a \approx \varepsilon_r$. In contrast, the rewetted samples showed anisotropy with a relatively larger radial strain normal to bedding compared to the axial one parallel to bedding, $\varepsilon_{r\perp} > \varepsilon_{a/\!/}$. The anisotropic compaction is attributed to more closure of the micro-fissures

mostly embedded in bedding planes, which had been enlarged by free swelling of clay minerals during the resaturation phase in unconstrained conditions.

Logically, the volume compaction of the rewetted samples with more micro-fissures is more significant compared to the non-wetted samples. This is demonstrated in Fig. 3.6 summarizing the volumetric compaction curves vs. time (ε_v - t) and vs. isostatic stress (ε_v - σ_m) for the non-wetted samples (a) and the rewetted ones (b), respectively. The volume reduction of the rewetted samples with S_w = 85±5.0 % reached to ε_v = 0.45 – 0.70 %, which is higher than those f ε_v = 0.35 – 0.55 % for the non-wetted samples with lower S_w-values of 68±9.0 %. However, the remaining volumetric strains are quite similar in a range of 0.2 – 0.4 % for both non-wetted and rewetted samples, which were attributed to the permanent closure of the micro-fissures more in wetted and less in dried claystone. The reduction in porosity implies an increase in its water saturation up to $\Delta S_w \approx 2 – 3$ % for all the samples.

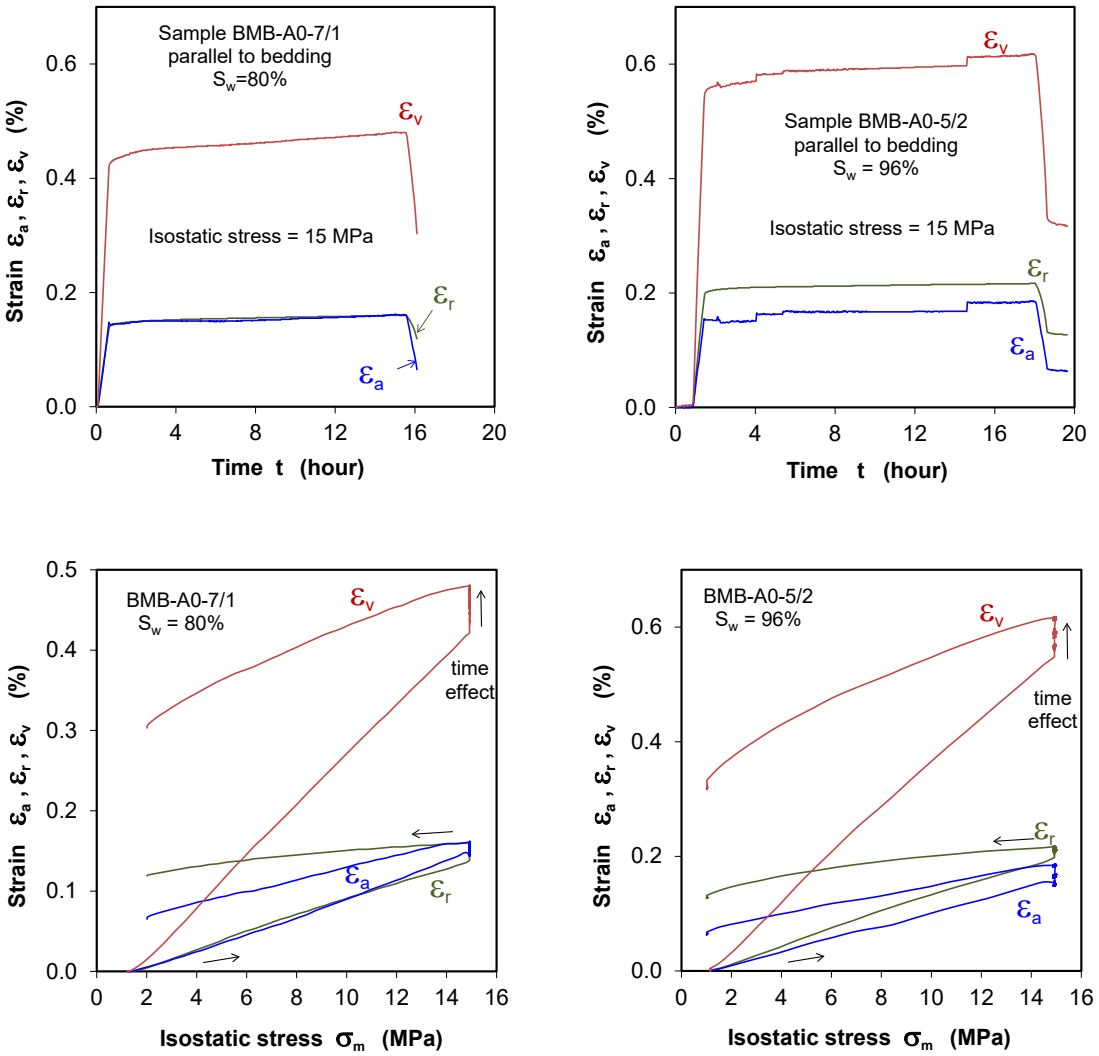

a. Sample BMB-A0-7/1 (S_w = 80%)

b. Sample BMB-A0-5/2 (S_w = 96%)

Fig. 3.5 Typical results of the pre-compaction of the delivered and wetted samples under undrained and isostatic load conditions

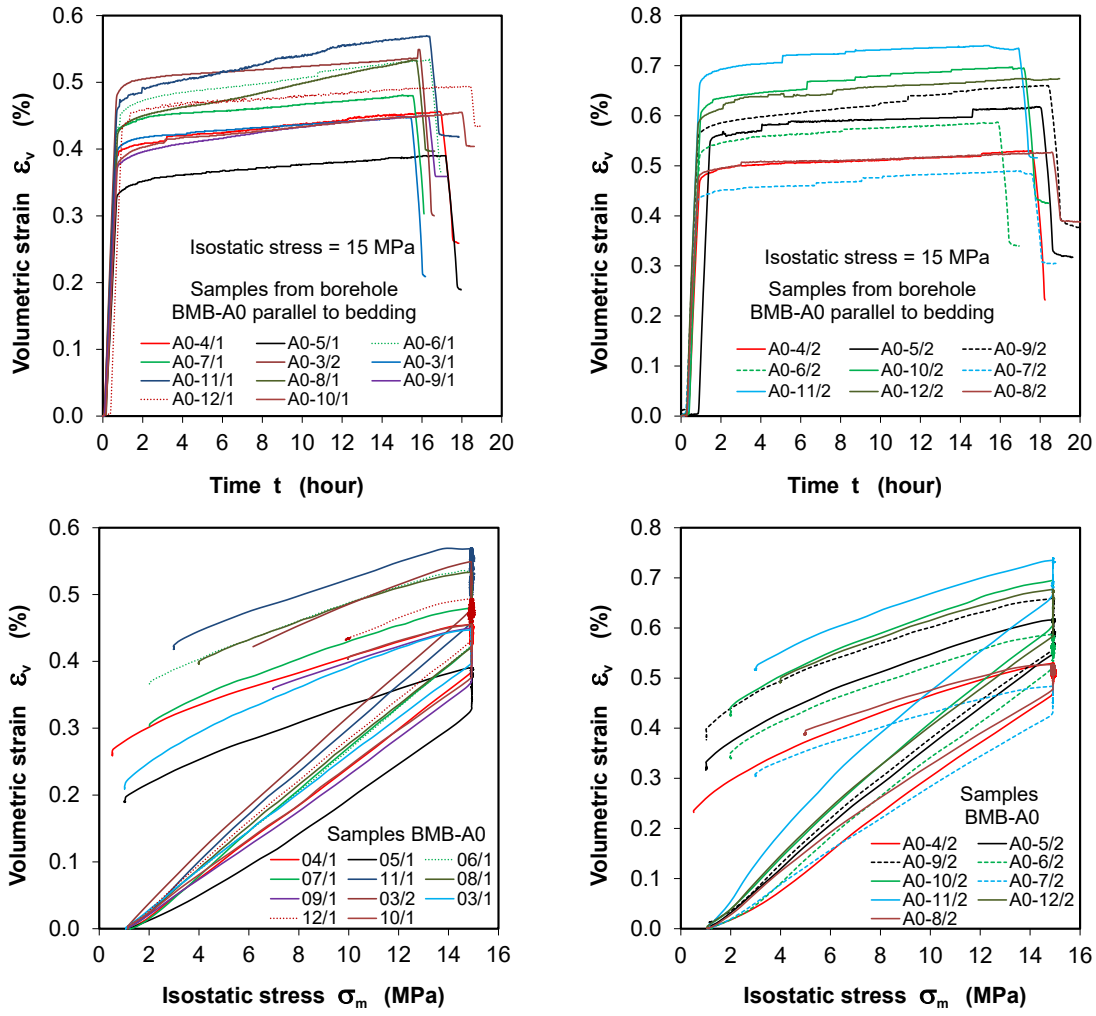

a. Group A with non-wetted samples (S_w = 68±9.0%)

b. Group B with rewetted samples (S_w = 85±5.0%)

Fig. 3.6 Volumetric compaction of the non-wetted and rewetted samples under undrained and isostatic load conditions

3.3.1.2 Deviatoric compression

Following the pre-compaction, deviatoric loading was increased by increasing axial deformation at a rate of $7 \cdot 10^{-7}$ s^{-1} under different radial stresses of σ_r = 0.5, 1, 2, 3, 4, 5, 7 and 10 MPa to examine deformation and damage to failure. As an example, results of a typical test on a highly-saturated sample BMB-A0-5/2 with S_w = 96 % at σ_r = 1 MPa are illustrated in figure 3.7 in terms of deviatoric stress ($\Delta\sigma = \sigma_a - \sigma_r$) vs. axial / radial strain (ε_a, ε_r) and volumetric strain vs. axial strain ($\varepsilon_v - \varepsilon_a$). The stress-strain curves show axial compression ($\varepsilon_a > 0$), radial extension ($\varepsilon_r < 0$) and volumetric compaction ($\varepsilon_r > 0$) with loading. As the stress reaches a critical value σ_D, the volume compaction reaches its maximum and then turns over to dilation. The stress at the onset of dilatan-

cy is called dilatancy threshold, which indicates an initiation of micro-cracks or damage. Further increase of the deviatoric stress leads to growth of micro-cracks or dilatancy/damage evolution to failure at its peak strength σ_F. Subsequently, the stress decreases with further development of the cracks down to a residual strength σ_R.

The stress-strain behaviour is qualitatively independent of the degree of water saturation (S_w) in the claystone and the radial stress (σ_r). But the quantities of the mechanical deformation and strength are influenced by both. Figure 3.8a and 3.8b show the deviatoric stress-strain curves of the non-wetted samples with S_w = 68±9.0 % and the re-wetted samples with S_w = 85±5.0 %, respectively. The results from each test group show that the deformation becomes progressively from brittle to ductile as the radial stress increases because the inner structure of the claystone becomes more compacted (indicated by large volumetric compressive strains) and hence fracturing is inhibited.

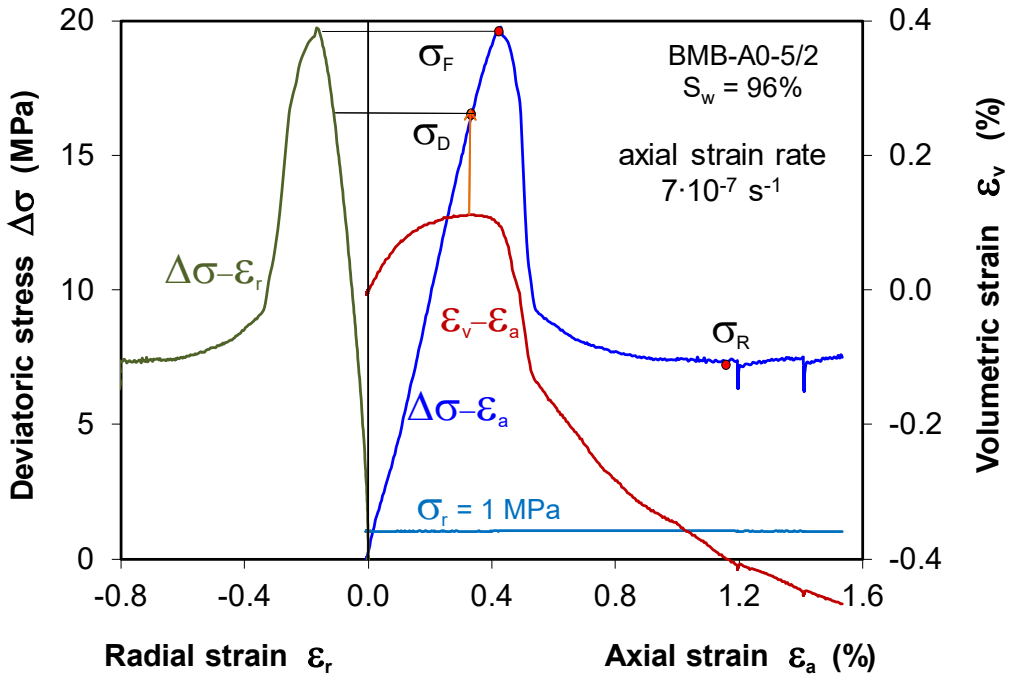

Fig. 3.7 Typical deviatoric stress-strain curves ($\Delta\sigma$–ε_a, $\Delta\sigma$–ε_r, ε_v–ε_a) of the claystone with dilatancy threshold σ_D, peak strength σ_F and residual strength σ_R

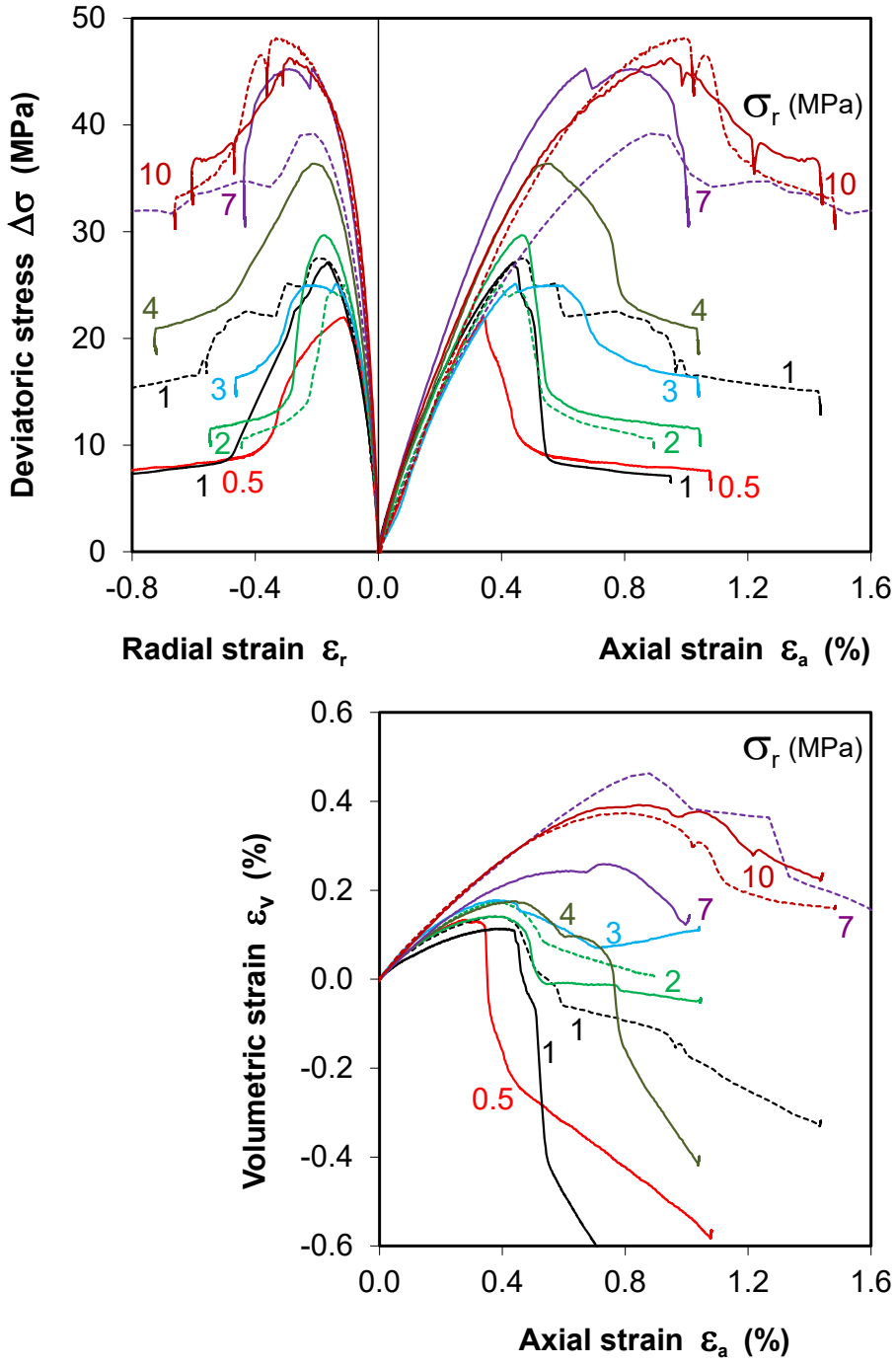

a. Non-wetted samples with an average saturation degree of 68 % (group A)

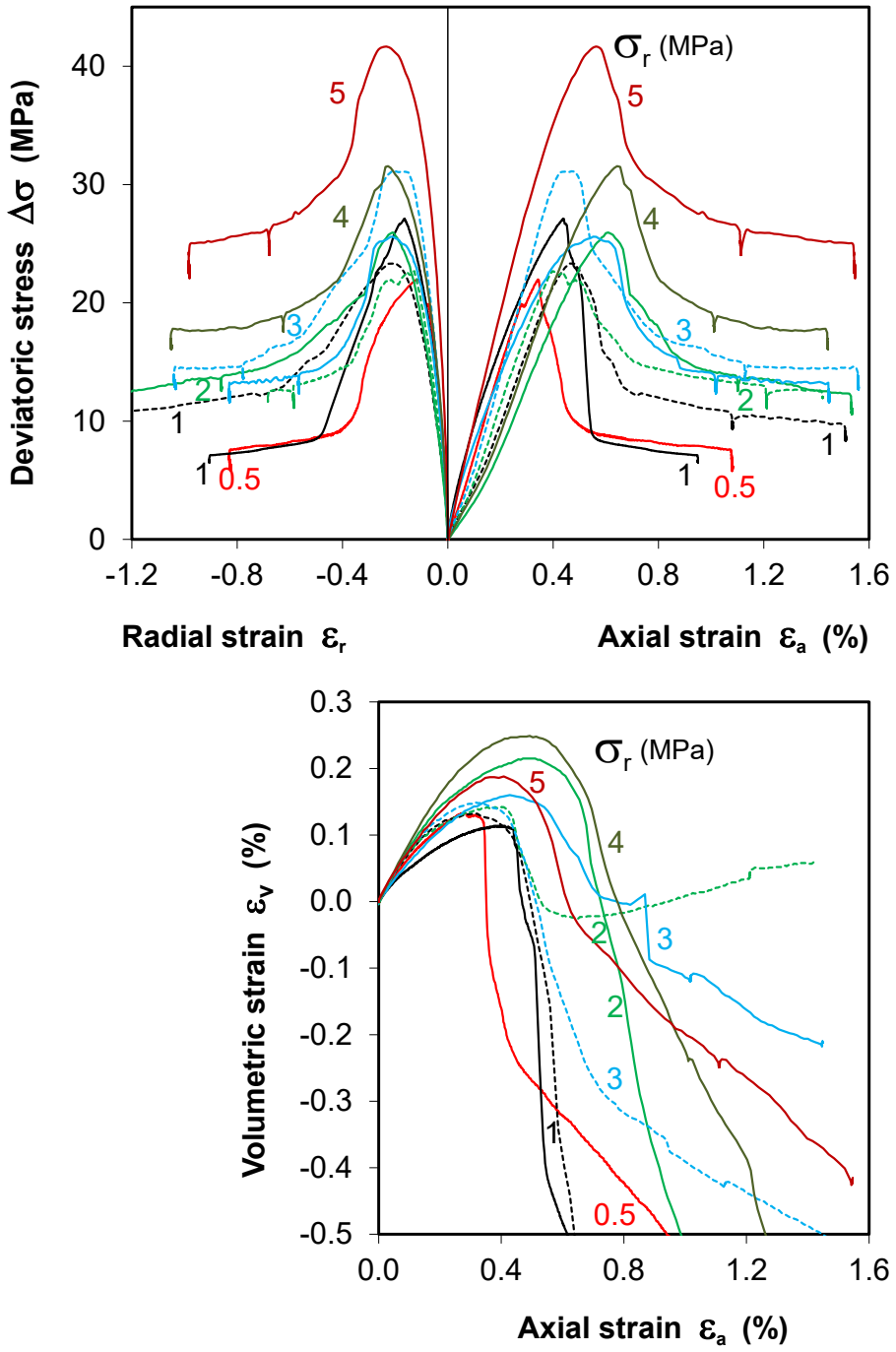

b. Rewetted samples with an average saturation degree of 85% (group B)

Fig. 3.8 Stress-strain behaviour of the no-wetted and rewetted samples during deviatoric loading

Influence of the wetting phase or water saturation on the stress-strain behaviour is highlighted in figure 3.9 comparing the stress-strain curves of the non-wetted and rewetted samples at σ_r = 0.5, 1, 2, 3, and 4 MPa. One can find out that at each given ra-

dial stress, the slopes of the stress-strain curves of the dried samples are steeper (indicating higher stiffness) and larger peak strength than those of the wetted samples. The higher stiffness and strength of the dried claystone are caused by high friction resistance between particles.

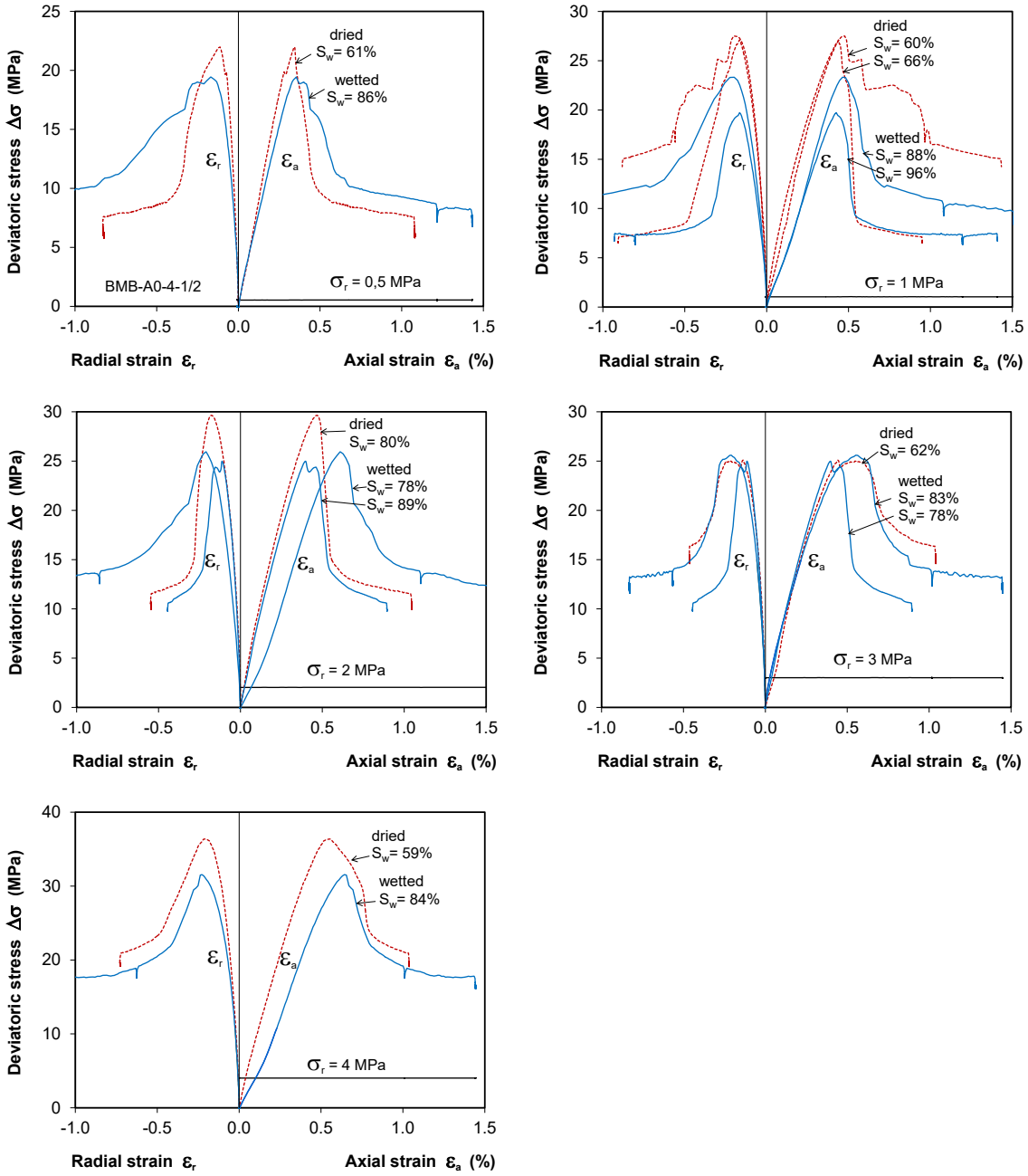

Fig. 3.9 Comparison of the deviatoric stress-strain curves of the dried and wetted samples at constant radial stress in a range from 0.5 to 4 MPa

Table 3.1 summarises the obtained data of dilatancy threshold σ_D, peak strength σ_F and residual strength σ_R as well as fracture angle ß oblique to the direction of the axial stress.

Tab. 3.1 Dilatancy threshold σ_D, peak strength σ_F and residual strength σ_R obtained on the dried samples in group 1 and wetted samples in group 2 during deviatoric loading (the characteristics of the samples in table 2.2)

Group A samples	Saturation degree S_w (%)	σ_r (MPa)	σ_D (MPa)	σ_F (MPa)	σ_R (MPa)	ß (°)
A0-4/1	61.3	0.5	19.8	22.0	7.5	15.0
A0-5/1	65.7	1.0	-	27.0	6.9	19.0
A0-6/1	87.9	2.0	24.3	24.9	10.4	19.0
A0-7/1	80.0	2.0	24.0	29.6	11.2	-
A0-8/1	58.6	4.0	28.7	36.1	21.1	21.5
A0-9/1	70.3	7.0	43.6	45.1	30.9	22.5
A0-10/1	71.3	10.0	43.2	45.9	36.6	27.0
A0-11/1	61.4	3.0	23.5	25.0	16.2	25.0
A0-12/1	63.8	10.0	44.0	47.9	33.3	20.0

Group B samples	Saturation degree S_w (%)	σ_r (MPa)	σ_D (MPa)	σ_F (MPa)	σ_R (MPa)	ß (°)
A0-4/2	85.5	0.5	17.1	19.4	8.0	12.0
A0-5/2	95.8	1.0	16.9	19.7	7.2	21.5
A0-6/2	81.6	2.0	-	22.6	12.3	21.5
A0-7/2	78.1	3.0	26.0	31.1	14.4	22.0
A0-8/2	80.0	5.0	32.0	41.2	25.1	20.0
A0-9/2	87.9	1.0	18.0	23.0	9.8	13.0
A0-102	88.7	2.0	22.0	25.9	12.4	13.0
A0-11/2	83.2	3.0	24.4	25.6	13.3	22.0
A0-12/2	83.8	4.0	24.7	31.4	17.7	25.0

The values of σ_D, σ_F and σ_R are depicted in figure 3.10 as a function of radial stress for the non-wetted samples with average saturation degree of S_w = 68 % and the rewetted ones with S_w = 85 %. It is obvious that the strengths increase with increasing the radial confining stress. At a given radial stress, the dilatancy and peak strength of the wetted samples are slightly lower than those of the dried samples, but the residual strength is similar for both. The values of dilatancy threshold vary in a range of 80 – 98 % of the peak strength at the dried samples and 78 – 95 % at the wetted ones. The average radio of dilatancy to peak strength is estimated to σ_D/σ_F = 0.91 for the dried claystone and

slightly lower value of σ_D/σ_F = 0.84 for the wetted claystone. Similarly, the ratio of residual to peak strength σ_R/σ_F = 0.53 obtained for the dried claystone is slightly lower than that of σ_R/σ_F = 0.49 for the wetted claystone.

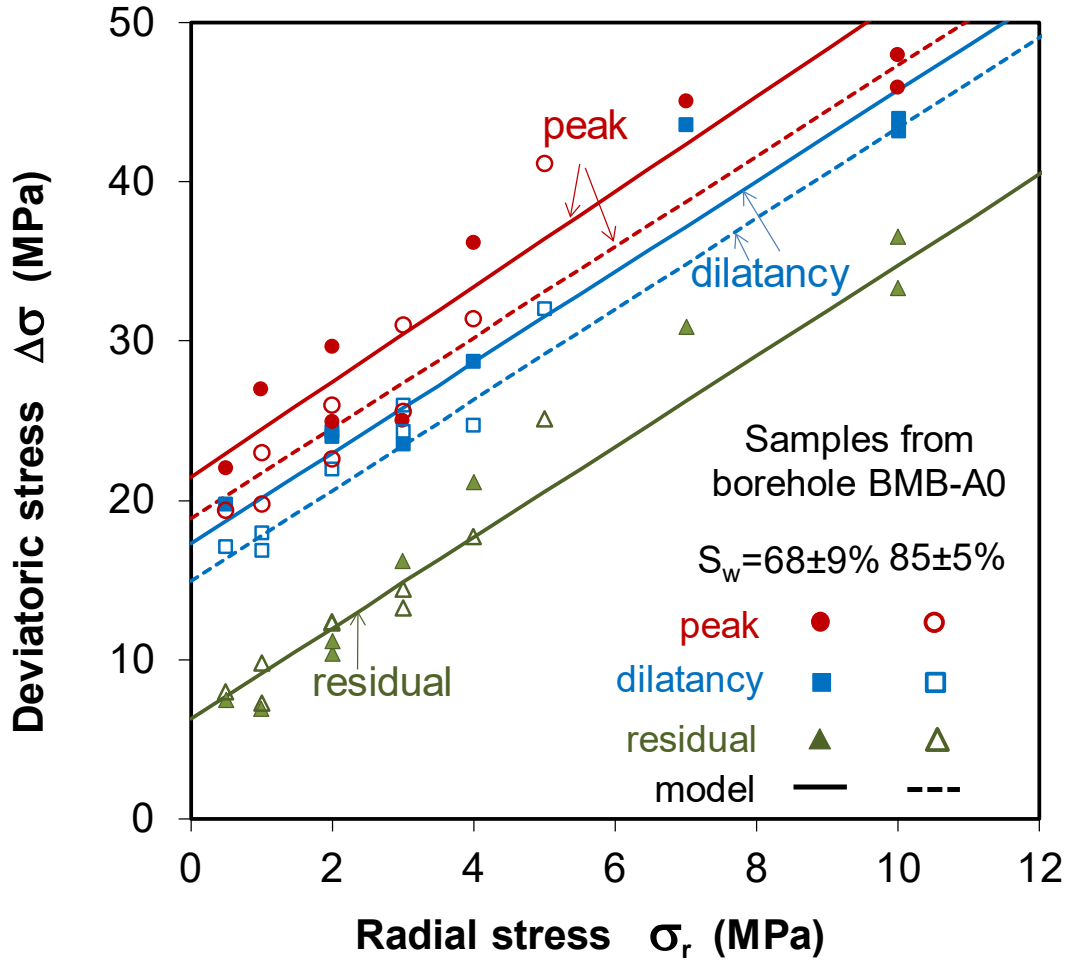

Fig. 3.10 Dilatancy, peak and residual strengths of the claystone dried to saturation degree of S_w = 68±9.0 % and wetted to S_w = 85±5.0 % as a function of radial stress

Figure 3.11 pictures fracture patterns of some non-wetted samples, similarly as observed on the rewetted samples (not shown here). The shear fracture angles oblique to the direction of the axial stress σ_a or major principal stress σ_1 are summarised in figure 3.12. Some values at low radial stresses σ_r < 2 MPa are relatively small β = 12 - 15°, which might be attributed to extensive effect of the bedding planes under low normal stresses. An average fracture angle at σ_r > 2 MPa is β = 22.5°.

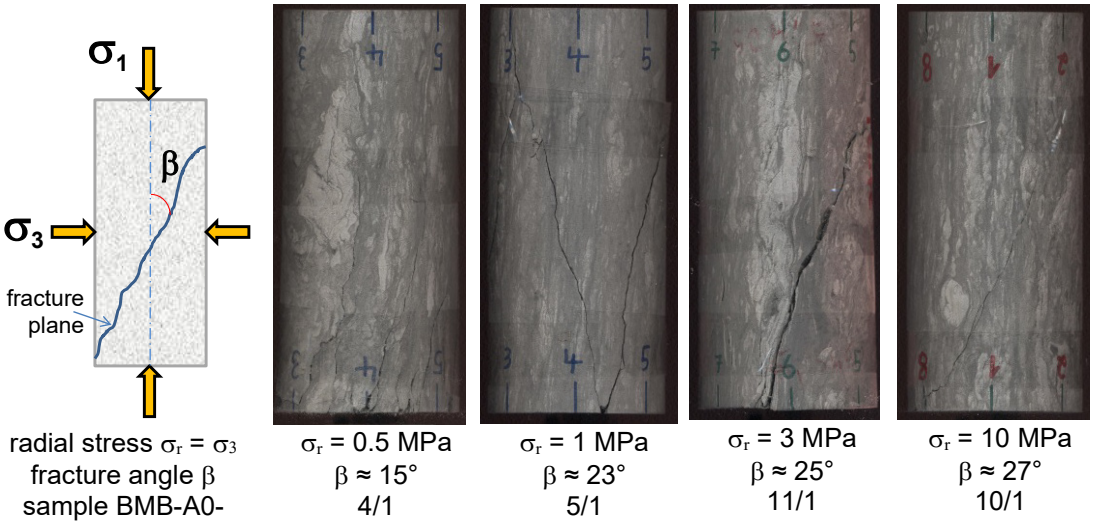

Fig. 3.11 Pictures of some failed samples with induced fractures after deviatoric compression at different radial stresses

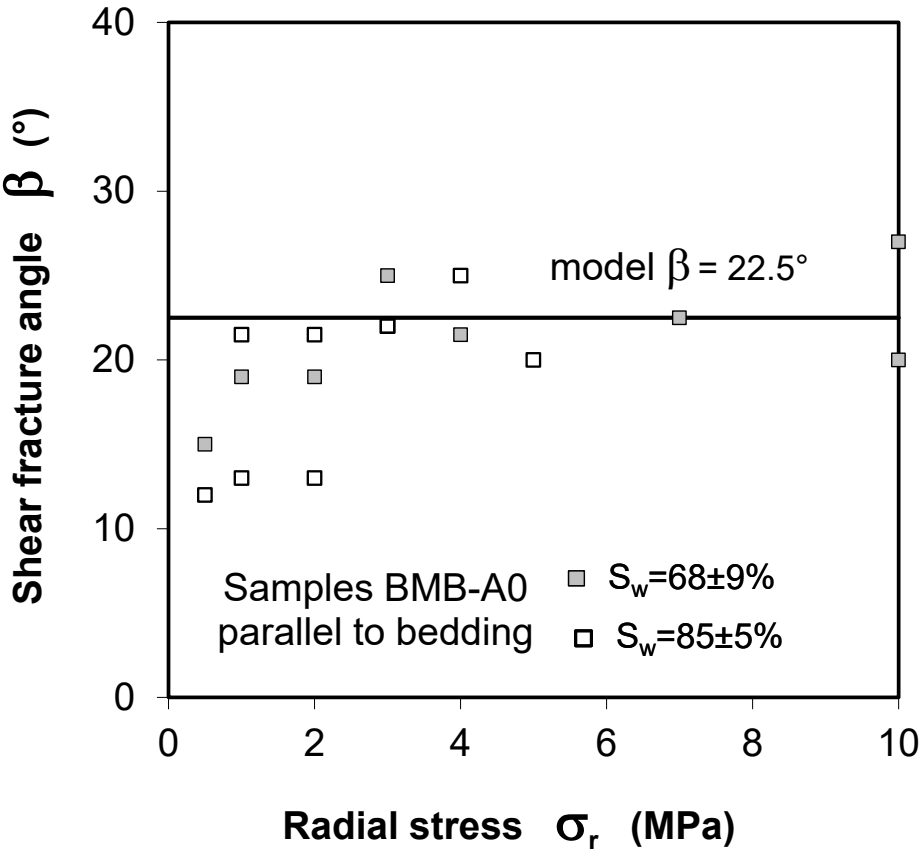

Fig. 3.12 Shear fracture angles observed on the failed samples under different radial stresses in comparison with the model result

3.3.2 Triaxial extension

3.3.2.1 Pre-compaction

Figure 3.13 shows the volumetric compaction vs. time and isostatic stress for the samples. The samples for TEA were compacted under an isostatic stress σ_m = 15 MPa and the TEM samples under σ_m = 15, 16, 18 and 20 MPa, respectively. Because of the different initial states of the samples with S_w = 61±7.0 %, the volume reduction varied in a range of ε_v = 0.65 % to 0.95 %. The volume compaction decreased the porosity and thus increased the water saturation by $\Delta S_w \approx 3 - 4$ % for the samples.

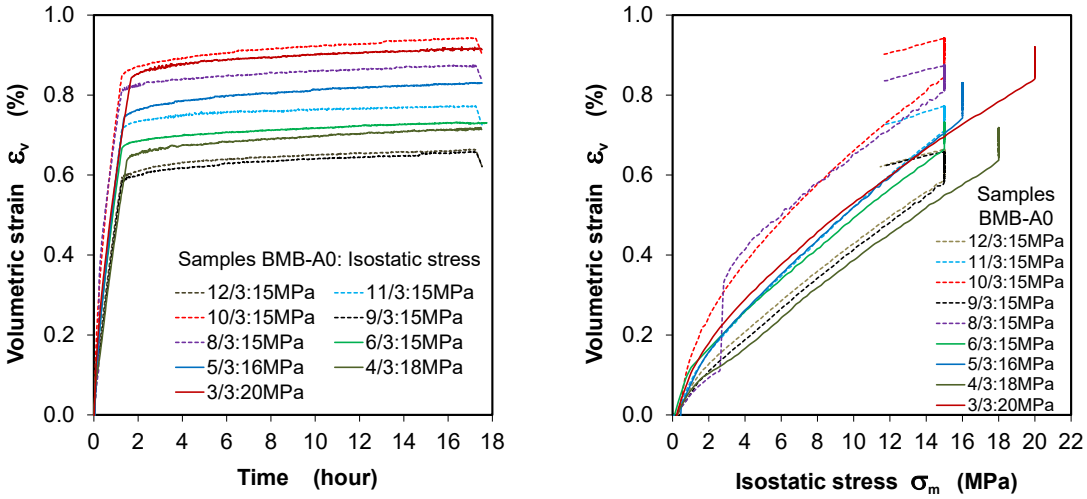

Fig. 3.13 Volumetric compaction of the dried samples with saturation degrees of 61±7.0 % under undrained and isostatic load conditions

3.3.2.2 Deviatoric extension

TEM results

The loading paths realised during the triaxial extension tests (TEM) are illustrated in figure 3.14. During TEM loading by increasing σ_r and decreasing σ_a at constant σ_m, the axial load was limited at zero, where no failure occurred yet at sample BMB-A0-5/3 at σ_m = 16 MPa and BMB-A0-3/3 at σ_m = 20 MPa. In order to reach failure, the minimum axial stress $\sigma_a \approx 0$ was kept and the radial stress σ_r increased continually, so that the failure took place not at the prescribed mean stress σ_m but at the newly reached one σ_{mF}. The stress difference is defined here by $\Delta\sigma = \sigma_r - \sigma_a$.

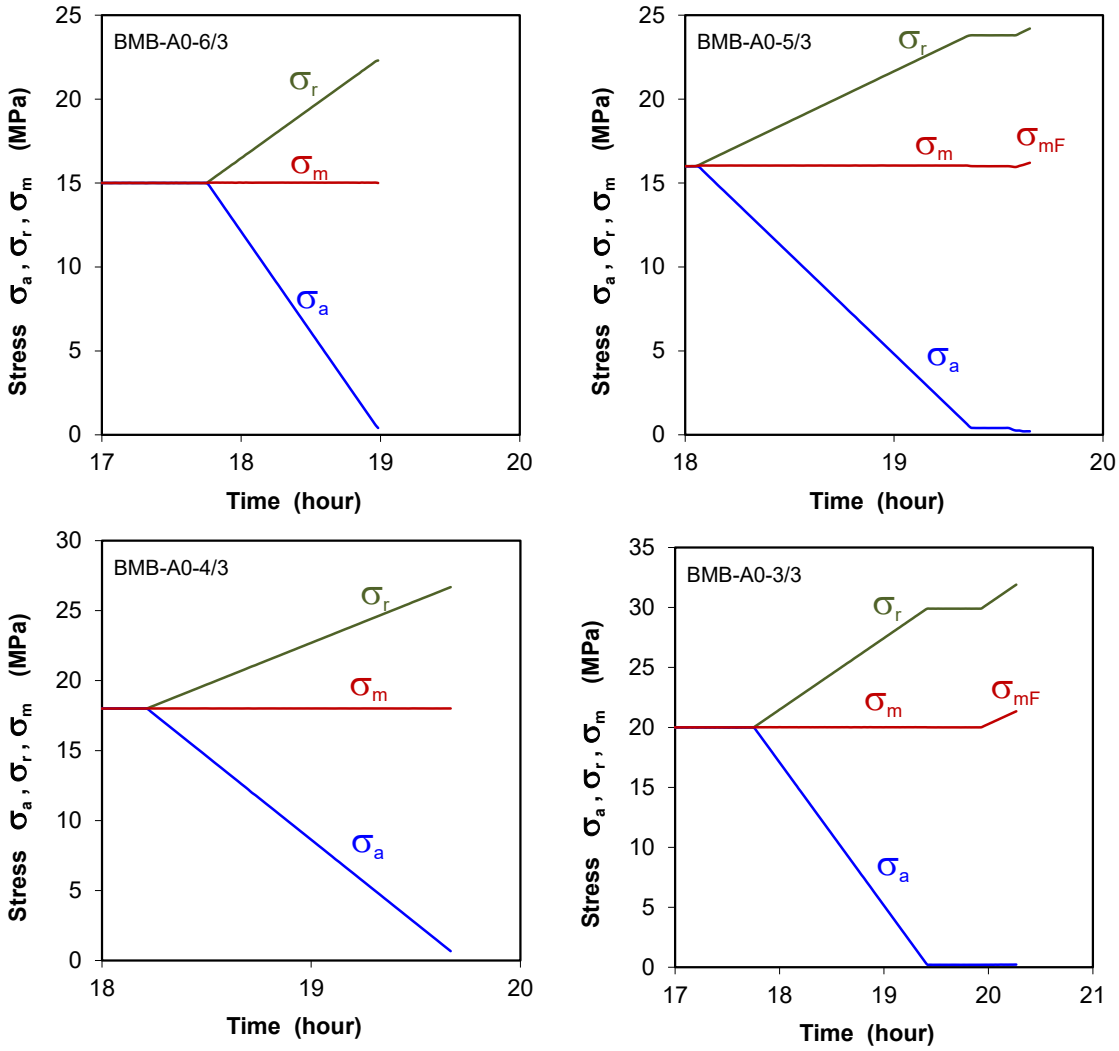

Fig. 3.14 Evolution of applied stresses during the triaxial extension (TEM) by lateral compression and axial extension

Responses of strains to the extension loading at constant mean stress σ_m = 15, 16, 18 and 20 MPa are presented in figure 3.15. The samples deformed in radial compression ($\varepsilon_r > 0$) and axial tension ($\varepsilon_a < 0$). The strains are related non-linearly to the deviatoric stress. The volumetric strains evolved over a transition phase from compaction to dilatancy at high deviatoric stresses. Further extensive loading resulted in failure.

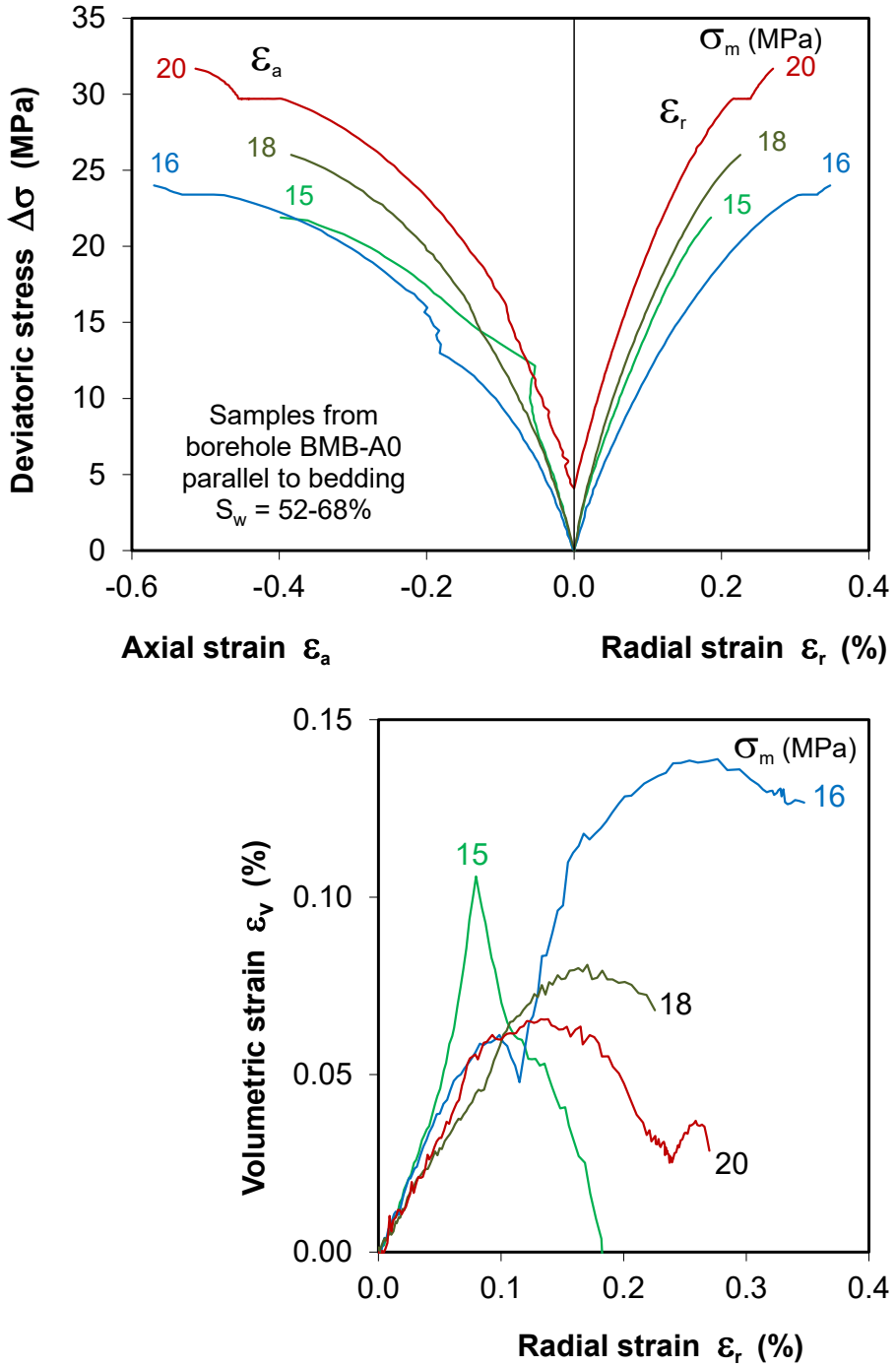

Fig. 3.15 Stress-strain curves obtained on the dried samples with saturation degrees of 52 – 63 % during lateral compression and axial extension at constant mean stress in a range of 15 to 20 MPa

TEA results

Similar like the TEM, the prescribed axial stress σ_a in some TEA tests had to be decreased for reaching failure because the maximum radial stress σ_r of about 50 MPa is allowed by this testing system. For instance, no failure occurred at sample BMB-A0-9/3

by increasing σ_r to the maximum at σ_a = 5 MPa and BMB-A0-8/3 at σ_a = 8 MPa, and then the axial stress σ_a was reduced to peak failure by keeping the increased radial stress σ_r = const, as shown in figure 3.16 depicting the evolution of applied stresses during TES testing.

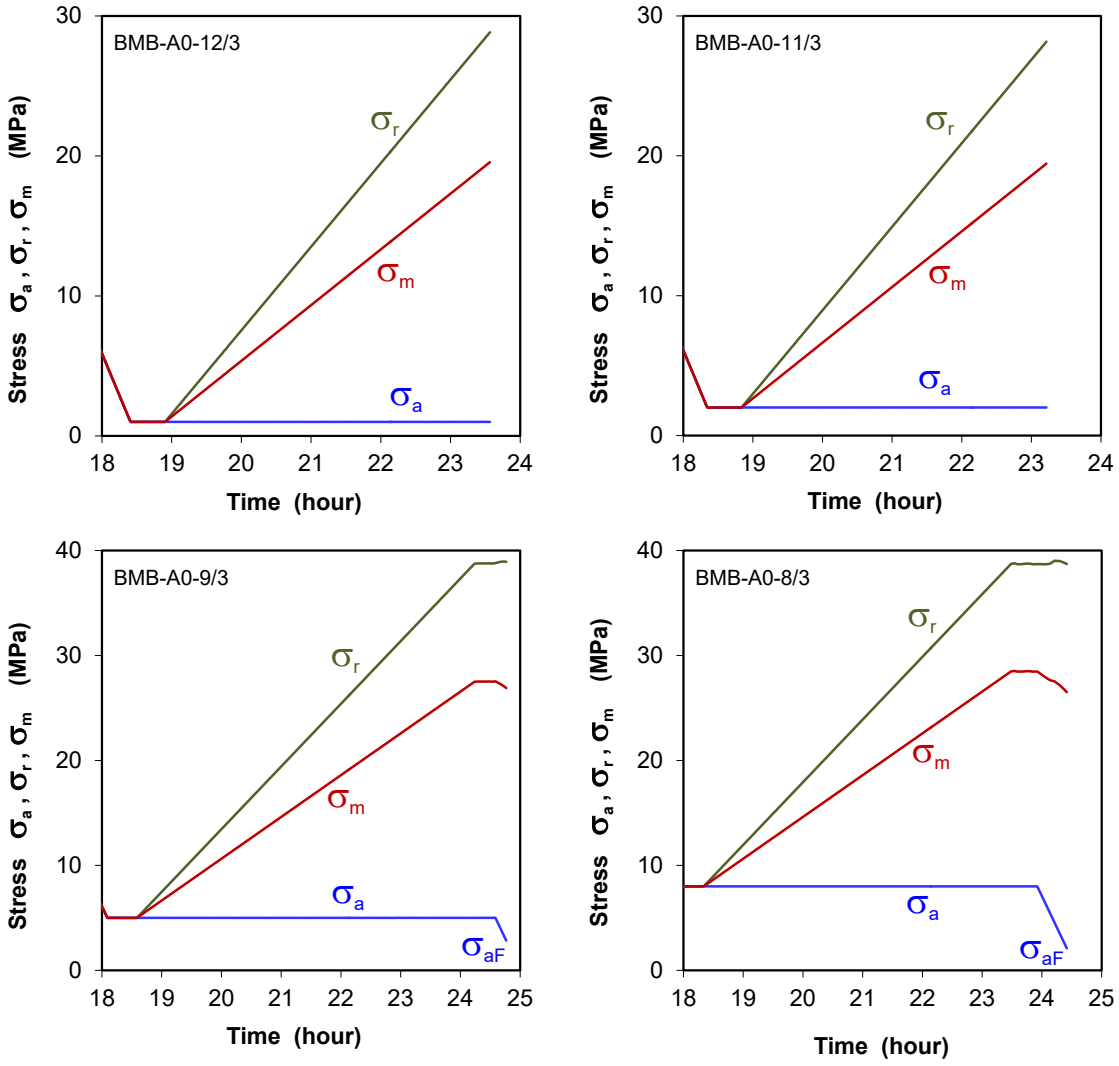

Fig. 3.16 Evolution of applied stresses during the triaxial extension (TEA) by lateral compression at constant axial stress

Stress-strain curves obtained during TEA loading at constant axial stress of σ_a = 1, 2, 3, 5, and 8 MPa are summarized in figure 3.17. As expected, axial elongation (ε_a < 0) occurs in the minor principle stress direction σ_a during the lateral compression (ε_r > 0). The volume compaction increases with increasing the lateral load up to the stresses close or equal to the peak failure strength.

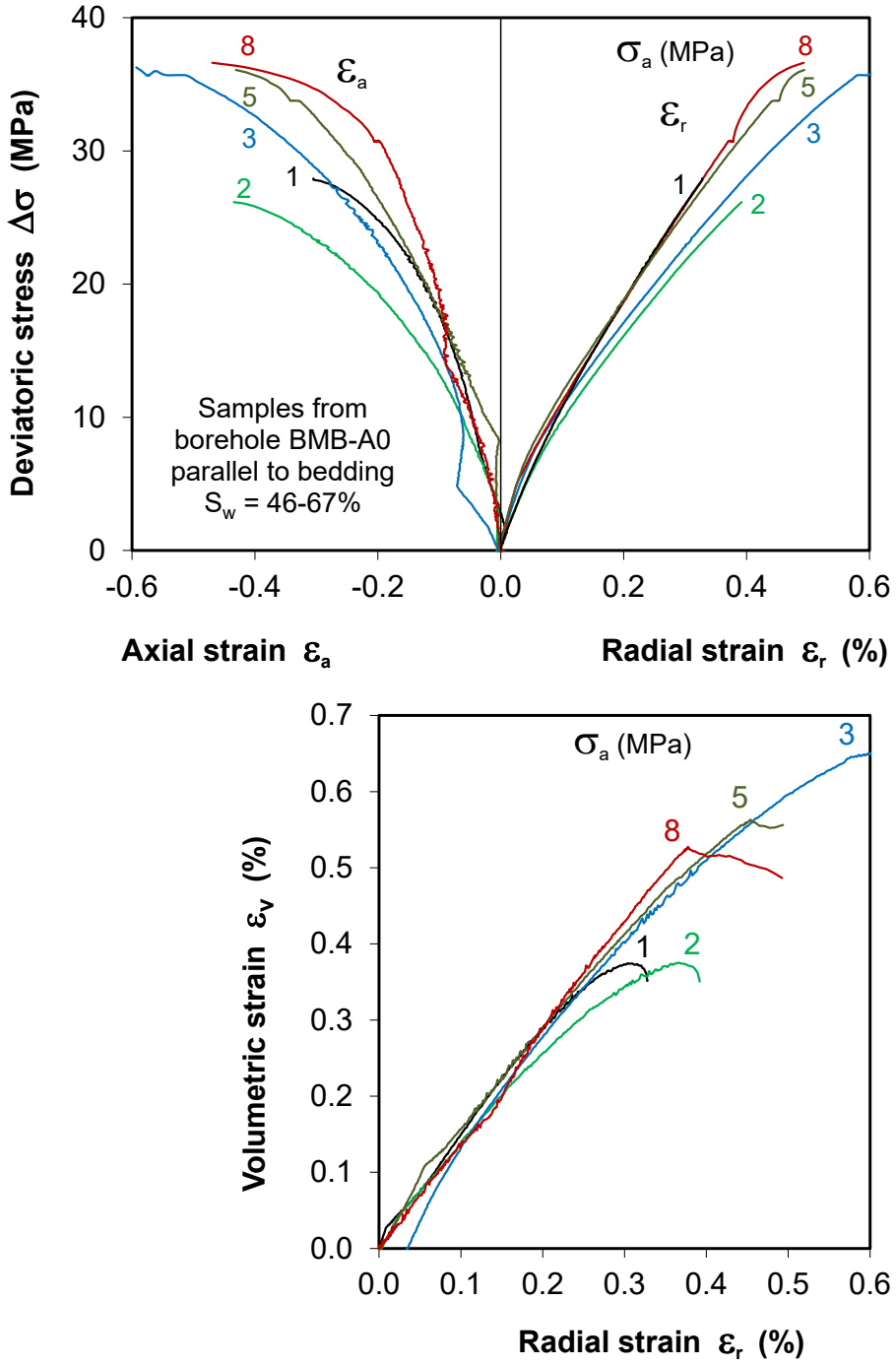

Fig. 3.17 Stress-strain curves obtained on the dried samples with saturation degrees of 46 – 67 % during lateral compression at constant axial stress in a range of 1 to 8 MPa

The dilatancy points (σ_{aD}, σ_D) and peak failure strength points (σ_{aF}, σ_F) are summarized in table 3.2. The onset of dilatancy occurred shortly before or at the peak strength. Generally, the extensional strengths increase with increasing the axial stress. Figure 3.18 shows fracture patterns of some failed samples under triaxial extension tests. The tested samples showed a single tensile fracture oblique to the radial stress at angles of 15-30 grades. The strength data will be evaluated in section 3.3.4 together with the other test results.

Tab. 3.2 Characteristics of the samples from borehole BMB-A0 parallel to bedding for triaxial extension tests (the characteristics of the samples in table 2.3)

TEM samples	**Saturation degree S_w (%)**	**σ_{mD} (MPa)**	**σ_D (MPa)**	**σ_{mF} (MPa)**	**σ_F (MPa)**	**ß (°)**
A0-3/3	52.1	20.0	22.5	21.0	31.7	25
A0-4/3	66.1	18.0	22.8	18.0	26.0	25
A0-5/3	64.2	16.0	22.2	19.0	24.0	20
A0-6/3	62.9	15.0	13.0	15.0	21.9	10
TEA samples	**Saturation degree S_w (%)**	**σ_{aD} (MPa)**	**σ_D (MPa)**	**σ_{aF} (MPa)**	**σ_F (MPa)**	**ß (°)**
A0-8/3	59.0	8.0	31.5	3.0	36.6	15
A0-9/3	67.3	5.0	35.0	3.4	36.1	30
A0-10/3	62.3	3.0	36.0	2.4	36.5	20
A0-11/3	57.6	2.0	26.0	2.0	26.2	25
A0-12/3	45.9	1.0	26.5	1.0	27.8	15

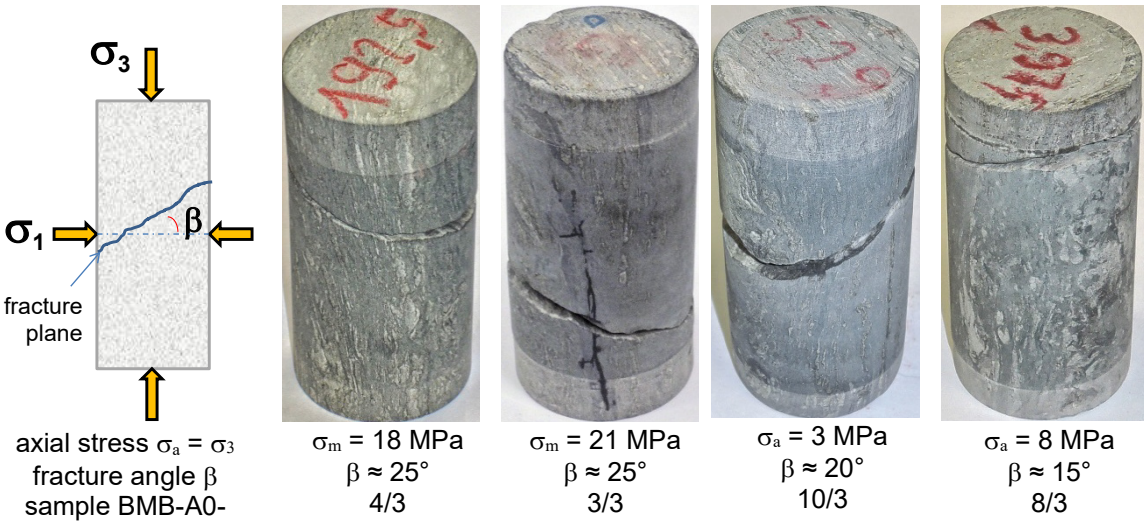

Fig. 3.18 Pictures of some samples fractured under triaxial extension at constant mean and axial stresses

3.3.3 Triaxial cyclic compression

3.3.3.1 Pre-compaction

Figure 3.19 shows volume strains of samples BDM-B9-1/4/6/9/15 during isostatic loading and unloading under drained conditions. Samples BDM-B9-1/4/15 had been rewetted to high degrees of S_w = 91 – 100 %, while the non-wetted samples BDM-B9-6/9 had low saturation degrees of S_w = 67 – 86 %. It is to be noted that the fully saturated sample BDM-B9-4 had been damaged to macro-cracks. Therefore, its compaction is more significant to a volume reduction of 1.7 % at 15 MPa. In contrast, the unsaturated samples BDM-B9-6 and B9-9 were less compacted to 0.4 – 0.5 %, which might be attributed to higher stiffness of dry claystone and less sampling-induced damage. The stress-strain (σ_m-ε_v) curves show that the volume compaction is non-linearly related to the load and also time dependent. During subsequent unloading, the volume expanded linear-elastically to some levels, but in no case fully reversible. The final results after unloading are summarized in table 3.3. Comparing the degrees of water saturation before (table 2.4) and after the pre-compaction (table 3.3), one can recognize that the water saturation was increased by 2 – 4 % due to the compaction of the pores and the rewetted samples became practically fully saturated (except for the non-wetted samples BDM-B9-6/9).

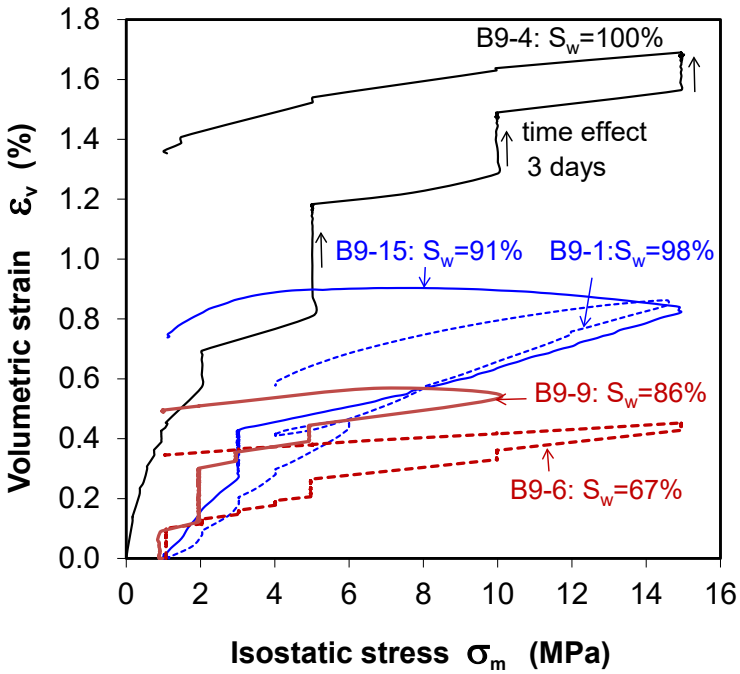

Fig. 3.19 Volumetric compaction of the samples during isostatic loading/unloading cycle in dependence on degree of water saturation

3.3.3.2 Deviatoric compression

Following the pre-compaction, multistep axial loading-unloading cycles were performed on the samples at radial stresses of σ_r = 1, 2, 3, 4 and 5 MPa to investigate the pre-failure behaviour of the claystone, including cyclic stress-strain relation, strain and damage evolution to failure, and resulting permeability change.

Figure 3.20 illustrates results of four samples at σ_r = 2, 3, 4 and 5 MPa in terms of deviatoric stress ($\Delta\sigma = \sigma_a - \sigma_r$) vs. axial / radial strain (ε_a, ε_r), and volumetric strain vs. axial strain ($\varepsilon_v - \varepsilon_a$) during the multistep loading-unloading cycles. The envelopes of the stress-strain curves show axial compression ($\varepsilon_a > 0$), radial extension ($\varepsilon_r < 0$) and volumetric compaction ($\varepsilon_r > 0$) with increasing the deviatoric stress. As the stress reaches the dilatancy threshold σ_D, the volume compaction reaches its maximum and then turns over to dilation. The dilation indicates a damage evolution due to initiation and growth of micro-cracks. Further increase of the deviatoric stress results in failure at its maximum or peak strength σ_F. Subsequently, the stress decreases with further development of the cracks to breakdown. Two samples showed relatively constant residual strength σ_R at σ_r = 3 and 5 MPa, respectively.

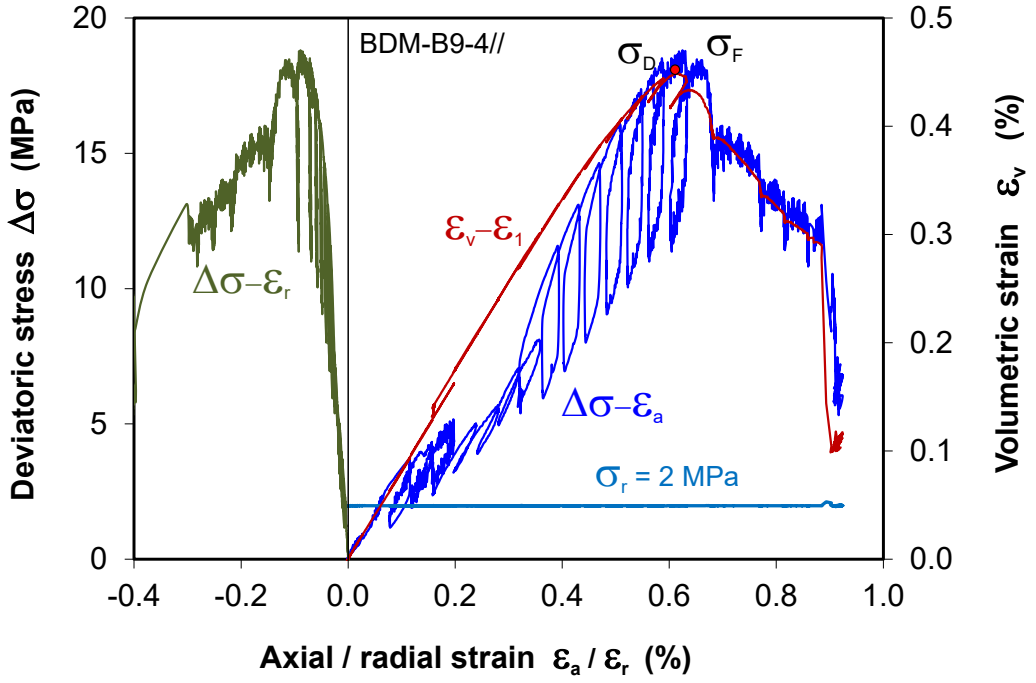

a. Sample BDM-B9-4 at radial stress of 2 MPa

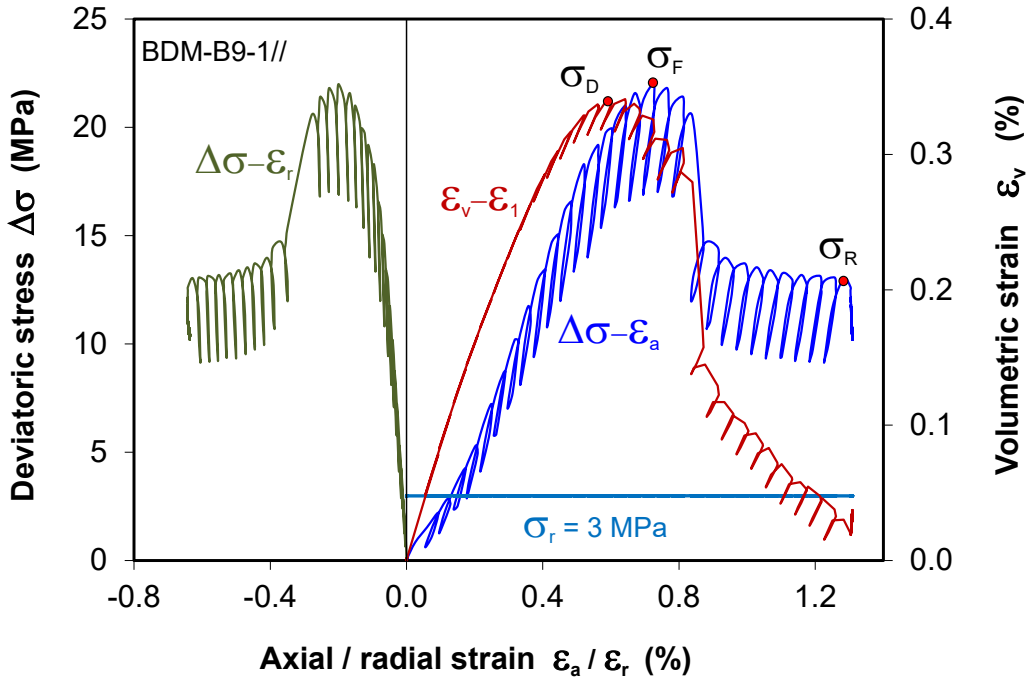

b. Sample BDM-B9-1 at radial stress of 3 MPa

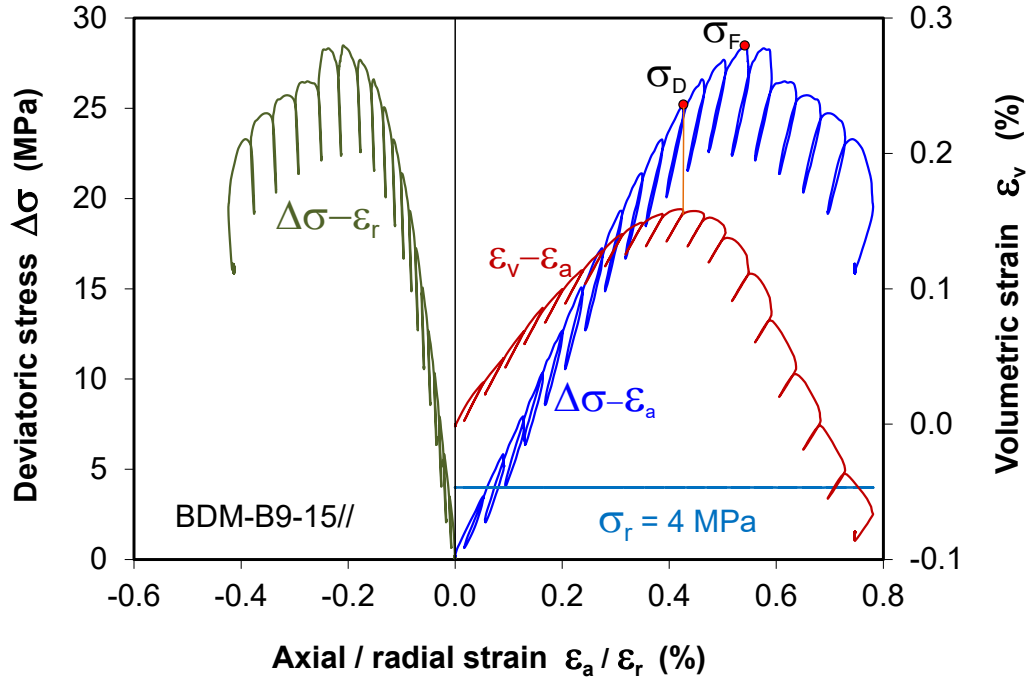

c. Sample BDM-B9-15 at radial stress of 4 MPa

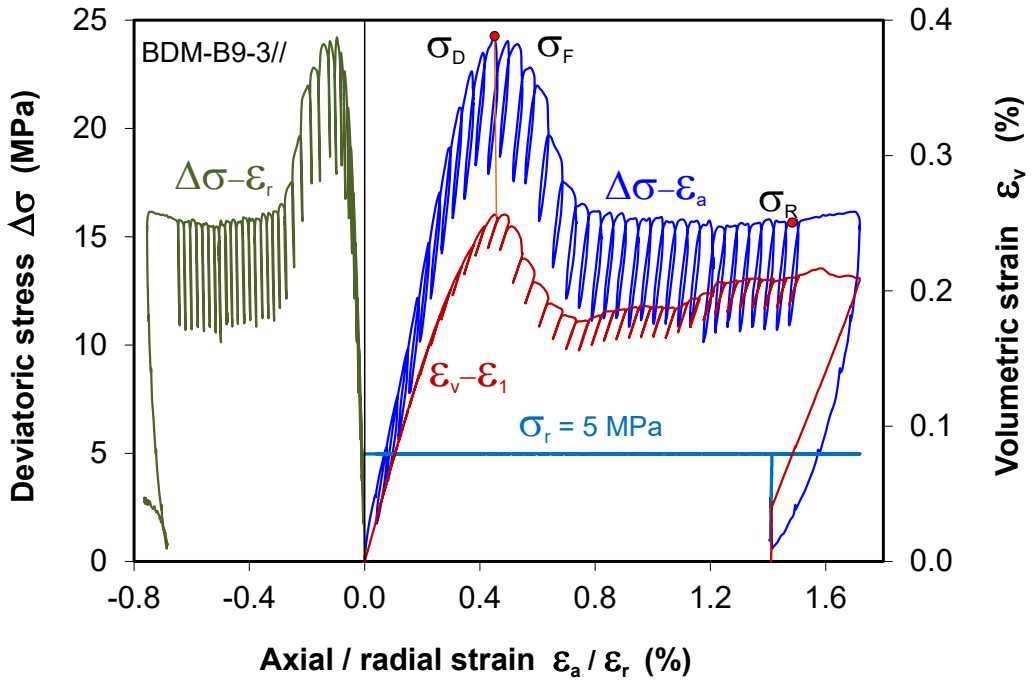

d. Sample BDM-B9-3 at radial stress of 5 MPa

Fig. 3.20 Stress-strain curves obtained on four highly saturated samples during cyclic deviatoric loading/unloading

Tab. 3.3 Results of the pre-compaction and deviatoric compression on the samples from borehole BDM-B9 parallel to bedding (cf. the characteristics of the samples in table 2.4)

	Pre-compaction			Deviatoric compressive strengths			
Sample	**Mean stress σ_m (MPa)**	**Porosity ϕ (%)**	**Saturation degree S_w (%)**	**Radial stress σ_r (MPa)**	**Dilatancy threshold σ_D (MPa)**	**Failure strength σ_F (MPa)**	**Fracture angle β (°)**
B9-1	15.0	12.64	100.0	3	20.8	22.1	20
B9-3	5.0	12.16	96.0	5	24.3	24.3	30
B9-4	15.0	12.95	100.0	2	18.7	18.9	20
B9-15	15.0	12.39	94.1	4	25.2	28.5	20
B9-6	15.0	6.12	70.5	2	51.0	56.0	20
B9-9	10.0	6.83	93.0	1	34.0	38.0	15

Based on the data obtained during the multistep loading-unloading cycles, the elastic parameters, namely Young's modulus E and Poisson's ratio ν, are determined along loading and unloading paths at different load and deformation conditions. Figure 3.21 shows the variations of measured E- and ν–values with deviatoric stress and axial deformation. It can be seen that E–values obtained along unloading path are generally higher than those along reloading, while ν–values are contrary. The values of E and ν are averaged for each loading-unloading cycle. The averaged E- and ν–values are depicted in figure 3.22 in correlation with volumetric strain ε_v for the respective sample at different radial stresses. It is obvious that the elastic stiffness E increases in relation with volume compaction until the dilatancy point σ_D is reached. In contrast, the subsequent decrease in stiffness with evolution of dilatancy. However, the Poisson's ratio ν does not change much in the beginning, then increased slightly to the dilatancy point σ_D and the peak failure σ_F, which indicates the opening of micro-cracks in the minor principal stress (σ_r) direction. During the post-failure stage, the relatively larger axial deformation compared to the radial one leads to a decrease of ν.

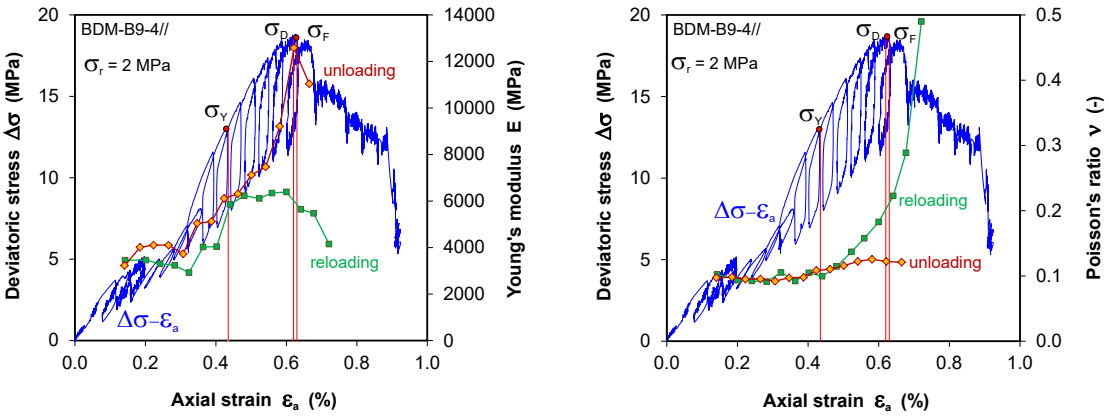

a. Sample BDM-B9-1 at radial stress of 3 MPa

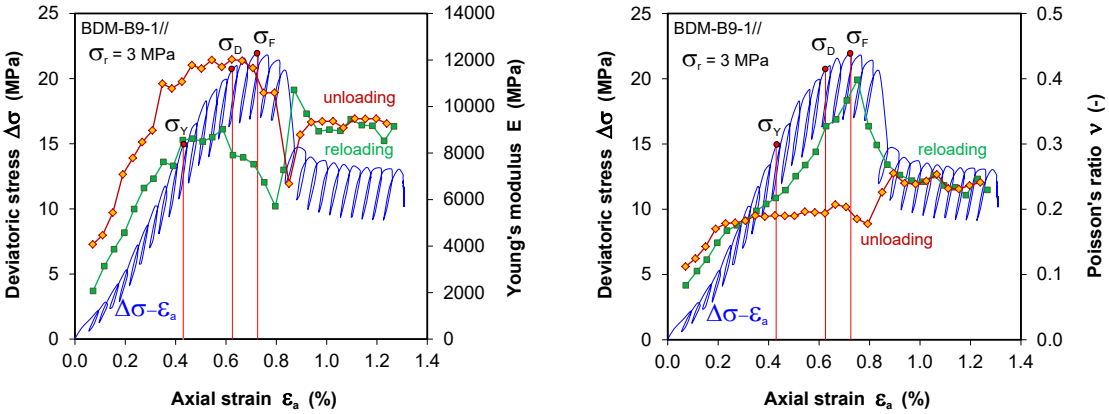

b. Sample BDM-B9-15 at radial stress of 4 MPa

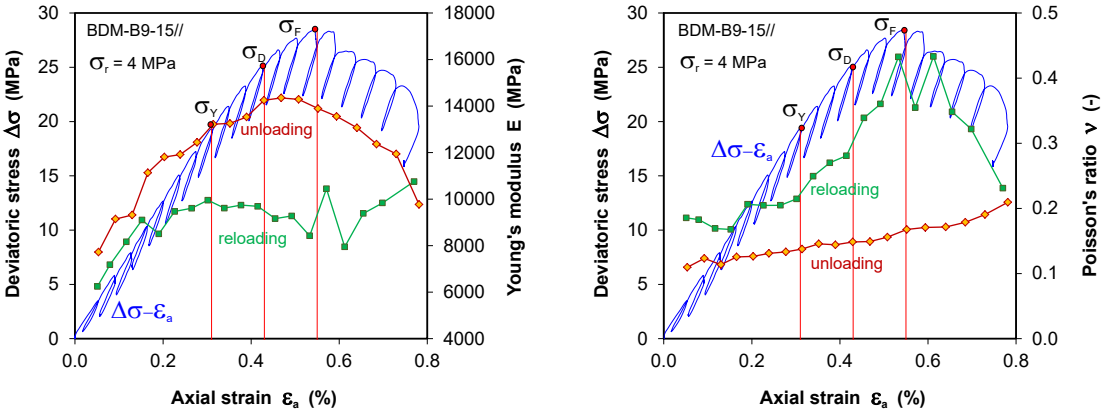

c. Sample BDM-B9-15 at radial stress of 4 MPa

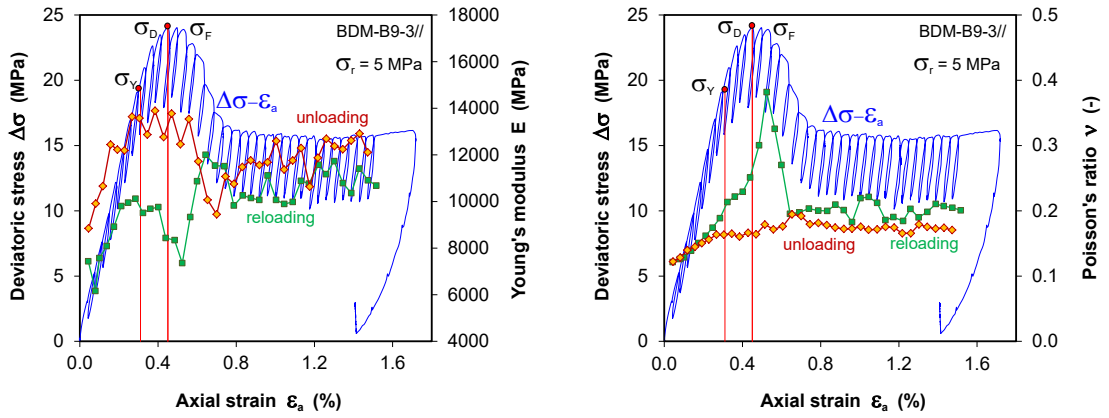

d. Sample BDM-B9-3 at radial stress of 5 MPa

Fig. 3.21 Evolution of Young's modulus and Poisson's ratio obtained from unloading and reloading paths with deviatoric stress and deformation

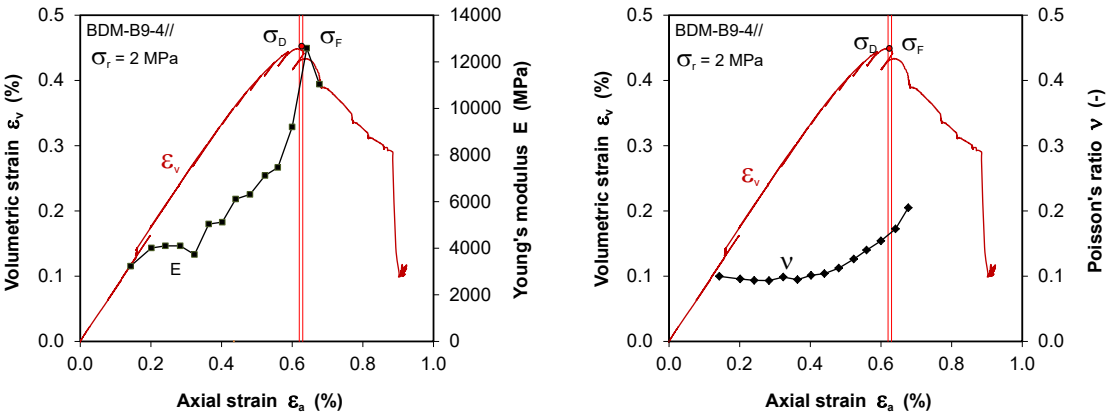

a. Sample BDM-B9-1 at radial stress of 3 MPa

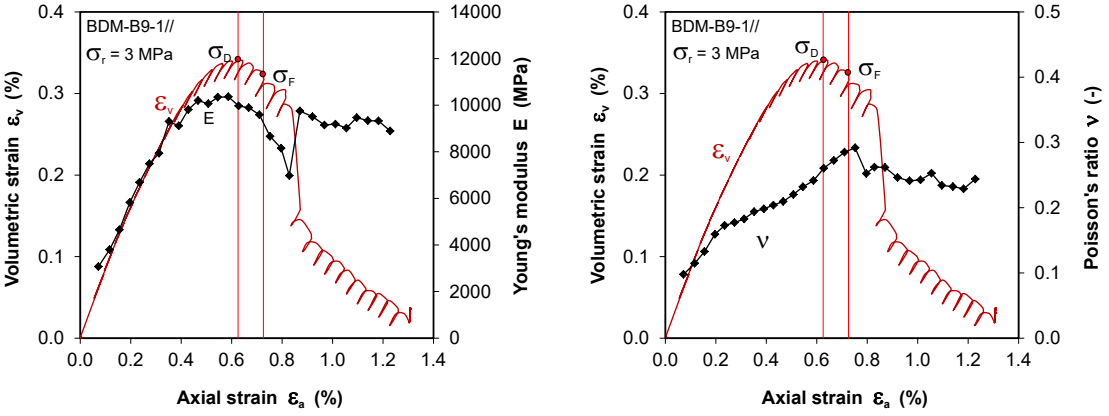

b. Sample BDM-B9-15 at radial stress of 4 MPa

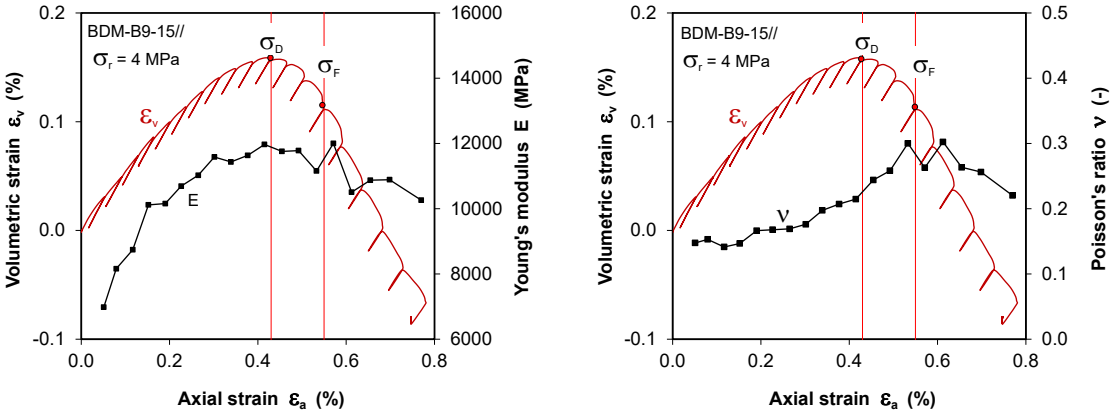

c. Sample BDM-B9-15 at radial stress of 4 MPa

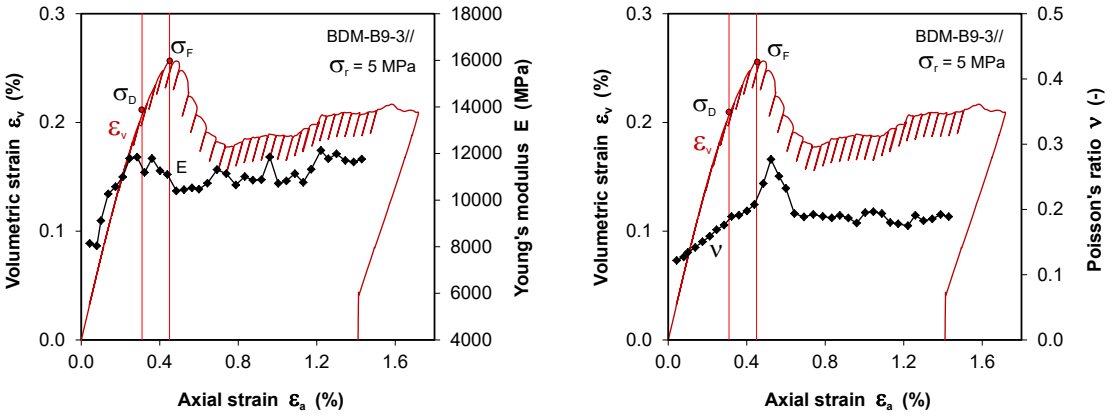

d. Sample BDM-B9-3 at radial stress of 5 MPa

Fig. 3.22 Elastic parameters averaged for each reloading-unloading cycle in correlation with volume change during deviatoric loading

Influences of the radial confining stress on the elastic parameters are illustrated in figure 3.23. Logically, the elastic stiffness E increases with increasing radial stress, which increases the density of the porous medium. In contrast, the Poisson's ratio ν is almost independent of the radial stress (despite of a sample at σ_r = 2 MPa).

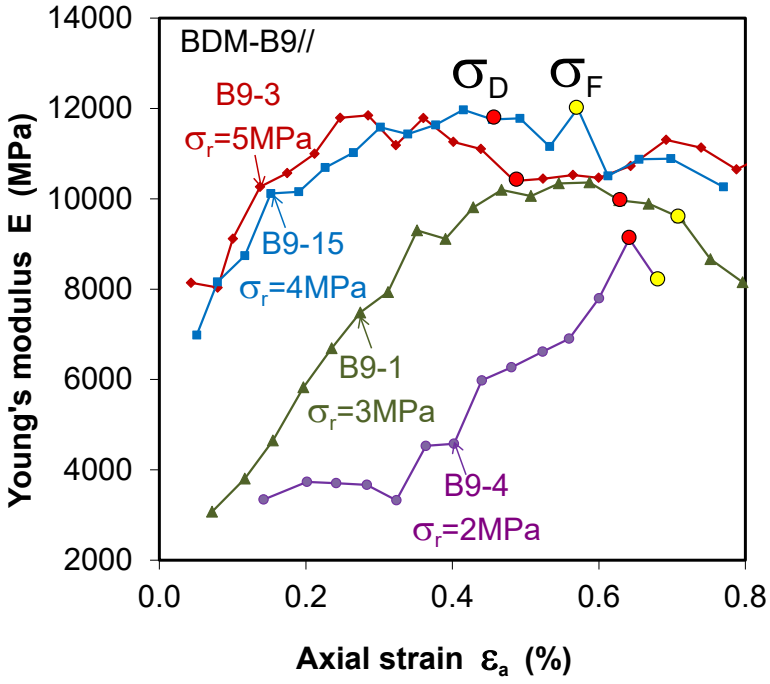

a. Young's modulus

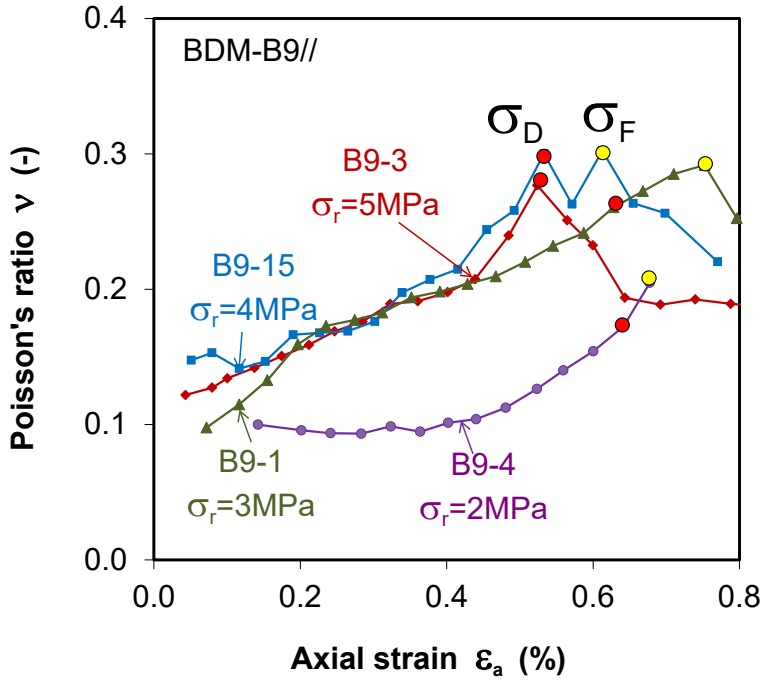

b. Poisson's ratio

Fig. 3.23 Variations of the elastic parameters with axial strain during deviatoric loading under different radial confining stresses

Additionally, the increase of the radial stress also leads to increase in the critical stresses at dilatancy and peak failure, as shown in figure 3.24. The dilatancy thresholds can be approximated by $\sigma_D = 0.9\sigma_F$. After testing, the failed samples were visually inspected. Fig. 3.25 shows some pictures of them. The fracture angle increases with increasing the lateral stress similar to the observations on the samples at TCS tests (cf. Fig. 3.11). The strength data will be evaluated in section 3.3.4 together with the other test data.

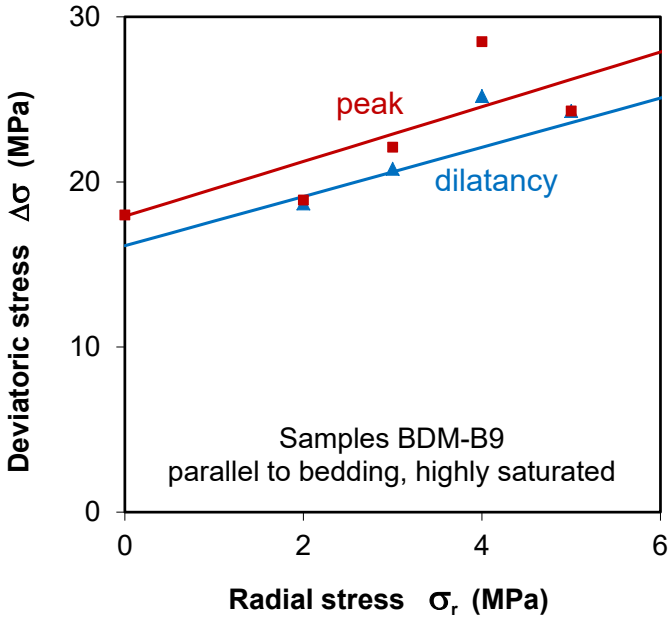

Fig. 3.24 Dilatancy and peak failure strengths of the OPA sandy claystone as function of radial stress

Fig. 3.25 Pictures of some failed samples with induced fractures after deviatoric compressional loading at constant radial stresses

3.3.4 Strength in dependence on load path

In order to uniformly evaluate the strength data obtained from the different load paths (TCS, TEM, TEA, TCD in Fig. 3.2), a more complex Mohr-Coulomb's model is adopted, which considers the third stress invariant in terms of Lode's angle as an additional factor determining the rock strength /UPC 15/ as

$$q = \frac{3 \cdot sin\varphi}{(\sqrt{3}cos\theta - sin\theta sin\varphi)}(\sigma_m + \sigma_t) \tag{3.3}$$

where

$q = \frac{1}{\sqrt{2}}[(\sigma_1 - \sigma_2)^2 + (\sigma_2 - \sigma_3)^2 + (\sigma_3 - \sigma_1)^2]^{1/2}$ shear stress

$\sigma_m = \frac{1}{3}(\sigma_1 + \sigma_2 + \sigma_3)$ mean stress

$\theta = arctan\left[\frac{2\sigma_2 - \sigma_1 - \sigma_3}{\sqrt{3}(\sigma_1 - \sigma_3)}\right] \quad (-\frac{\pi}{6} \leq \theta \leq \frac{\pi}{6})$ Lode's angle

$\sigma_1 > \sigma_2 > \sigma_3$ are the major, intermediate and minor principal stress, respectively,
$\sigma_t = c \cdot cot\varphi$ is tensile strength, c cohesion, and φ friction angle of the material.

This model takes into account the stress geometry or load path in terms of Lode's angle as a factor determining the shear strength of a material in addition to the mean stress and the material inherent properties (inner cohesion and friction resistance). In case of triaxial stress conditions, $q = |\sigma_1 - \sigma_3| = \Delta\sigma$, $\theta = -\pi/6$ for compression, where $\sigma_a = \sigma_1 \geq \sigma_r = \sigma_2 = \sigma_3$; and $\theta = \pi/6$ for extension, where $\sigma_a = \sigma_3 \leq \sigma_r = \sigma_2 = \sigma_3$.

Figure 3.26 summarizes the peak shear strengths as a function of mean stress obtained from the compression tests (TCS) on the samples with average saturation degrees of S_w = 68% and 85% respectively, the cyclic compression tests (TCD) on the highly saturated samples with S_w = 95%, the extension tests (TEA, TEM) on the relatively dry samples with S_w = 61 % and 63 % respectively. Fitting the data of the compression tests TCS and TCD ($\theta = -\pi/6$) yields the strength parameters for the samples with different saturation degrees. The cohesion is determined to c = 4.5, 3.5 and 2.5 MPa for Sw = 68 %, 85 % and 95 % respectively, whereas the friction angle determined is unique φ = 45°, independent of the saturation degree. This indicates that the water saturation affects the inner cohesion of the claystone but not - or only to a small amount - the inner friction. The cohesion decreases linearly with increasing the water saturation as shown in figure 3.27. An extrapolation yields the parameter c = 2.3 MPa

for full saturation. The extrapolated shear strength for the fully-saturated sandy claystone is depicted in figure 3.26, which is only slightly lower than that for Sw = 95 %.

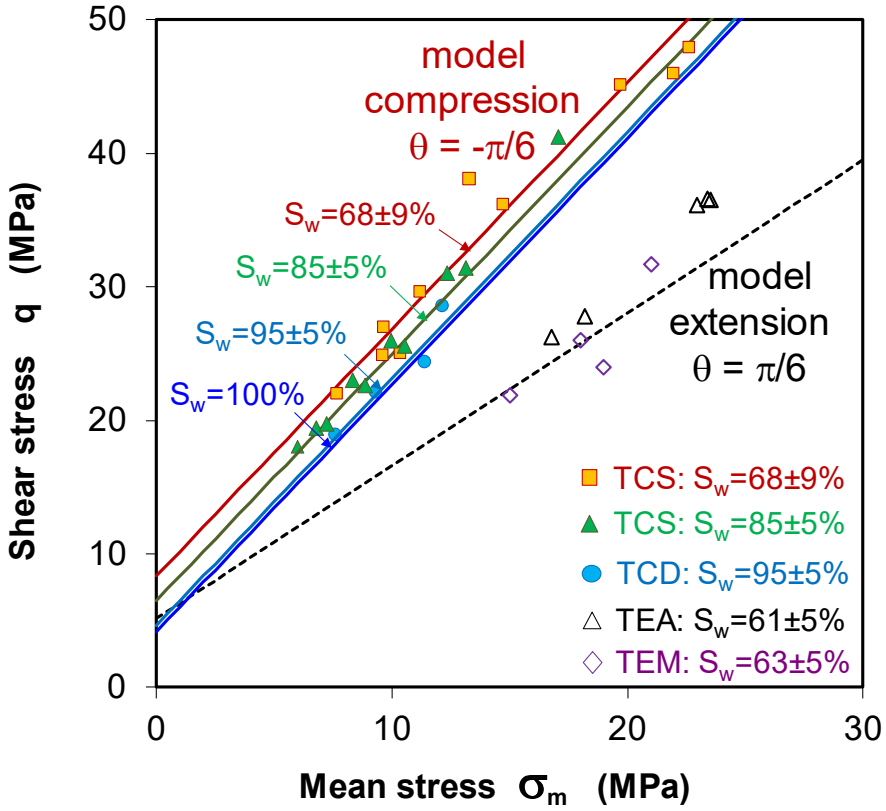

Fig. 3.26 Shear strength of the OPA sandy claystone under triaxial compression at constant radial stress (TCS & TCD: $\sigma_r = c$) and extension at constant mean (TEM: $\sigma_m = c$) or axial stress (TEA: $\sigma_a = c$) as a function of mean stress and degree of water saturation (S_w)

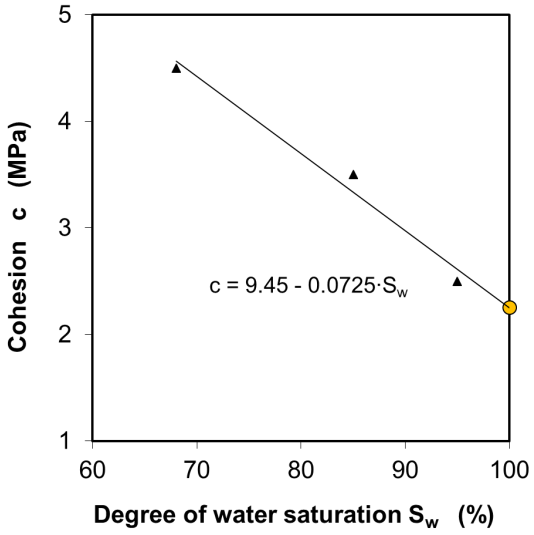

Fig. 3.27 Parameter cohesion related to the degree of water saturation

It is also obvious that at a given mean stress, the strength obtained by extension testing (TEA and TEM: $\theta = \pi/6$) is lower than that by compression (TCS & TCD: $\theta = -\pi/6$). Using the strength parameters of c = 4.5 MPa and φ = 45° obtained from the compression tests on the samples with S_w = 68 %, the extensional strength of the samples can be well predicted at any given stress state by applying the Mohr-Coulomb model (equation 9). Some underestimation of the data is probably due to the fact that the TEM and TEA samples were relatively dry at average S_w – values between 61 % and 63 %. Low water saturation enhances the strength of claystone.

After testing, failure modes of the samples were visually inspected, as already shown in figures 3.11 and 3.25 picturing some failed samples during the triaxial compression (TCS and TCD) and figure 3.18 some samples during the extension (TEA and TEM). The fracture angle is defined as the angle β of the fracture surface to the direction of the major principal stress σ_1 ($\sigma_1 = \sigma_a$ for triaxial compression; $\sigma_1 = \sigma_r$ for extension). The measured β - values are given in tables 3.1 (TCS), 3.2 (TEA, TEM) and 3.3 (TCD). The Mohr-Coulumb's model can predict a fracture angle by $\beta = 45° - \varphi/2 = 22.5°$. This value represents the mean value of the measured data β = 19° – 27° under compression (table 3.1 and 3.3) and β = 15° – 25° under extension (table 3.2), except for small values of β = 13° – 15° at low confining stresses. Figure 3.12 illustrates the model prediction for the fracture angle under compression at different radial stresses. The model overestimates the fracture angle at low radial stresses σ_r < 2 MPa, which might be attributed to aperture opening effect of the axial bedding planes in radial direction. The failure modes of the sandy claystone with bedding planes parallel to the major principal stress are similar to those observed on the OPA shaly facies /NAU 07/, /POP 07/, /VAL 12/.

It may be interesting to compare the shear strength of the OPA sandy facies to the shaly facies reported by Wild and Amann /WIL 18/ and to the shallow claystone at a depth of 33 m below ground by Giger et al. /GIG 18/. Figure 3.28 shows the Mohr-Coulumb's failure envelopes and strength data for these claystones in terms of shear strength q vs. effective mean stress p' (= σ_m - u, where σ_m is the total mean stress and u is the porewater pressure). The data were determined under drained and undrained triaxial compression tests at similar strain rates in a range of $7 \cdot 10^{-7}$ to $2 \cdot 10^{-8}$ s^{-1}. The strength parameters are summarized in table 3.4.

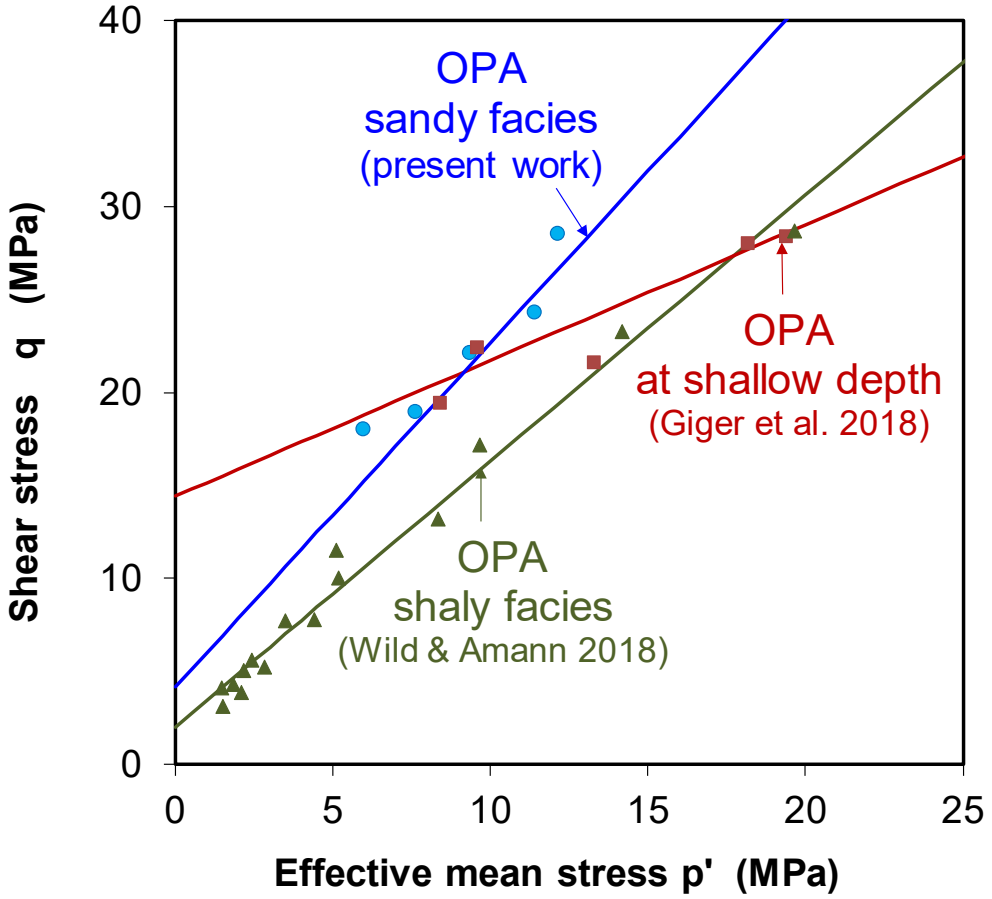

Fig. 3.28 Comparison of the Mohr-Coulumb's failure envelopes of the saturated OPA sandy facies (present work), shaly facies (Wild and Amann 2018 /WIL 18/), and shallow claystone (Giger et al. 2018 /GIG 18/) under drained and undrained triaxial compression

Tab. 3.4 Mohr-Coulumb's strength parameters of the OPA sandy and shaly facies and the shallow claystone at a depth of 33 m below ground

Material parameter	Sandy facies (present work)	Shaly facies (Wild and Amann 2018)	Shallow claystone (Giger et al. 2018)
Clay content (%)	25-40	60-80	59
Porosity (%)	10.4-13.2	16.2-17.5	10.3-13.1
Cohesion *c* (MPa)	4.5	1.0	6.8
Friction angle β (°)	45	35.3	19

Whereas the strength parameters for the sandy facies are obtained by the extrapolation of the unsaturated data to full saturation (c.f. figs. 3.26 and 3.27), the others /WIL 18/ and /GIG 18/ were determined on fully-saturated samples. The comparison shows that a) in the same mean stress range, the measured strength values of the

sandy facies are higher than those of the shallow claystone and the shaly facies, indicating that the strength increases with decreasing clay content and porosity; b) the slopes of the derived model lines are differing from each other, reflecting different friction angles of the materials. Somewhat unexpected, the failure envelope of the shallow claystone intersects those of the sandy and shaly facies at a low and high mean stress respectively, where the measured data are close to each other, too. Comparing the clay contents and porosities of the studied claystones (table 3.4), the strength of the shallow claystone shall be in between those of the sandy and shaly facies. A main reason for the inconsistent results may be from the different testing conditions applied. We encourage more systematic experiments under various conditions for enhancing the certainty of the strength parameters of the studied claystones.

3.3.5 Time-dependent behaviour

Time-dependent deformability of the sandy OPA claystone was studied on three samples (BLT-A8 and BDM-B9-11 and -12, table 2.5) under undrained multi-step triaxial loads by keeping a mean stress of $\sigma_m = (\sigma_a + 2\sigma_r)/3$ = 13 MPa over time periods of months to years. Sample BLT-A8 and BDM-B9-12 were rewetted to high saturation degrees of S_w = 93 % and S_w = 98.5 % respectively, while BDM-B9-11 was dried to a low saturation degree of S_w = 27.0 %. The tests on samples BDM-B9-11 and -12 with the different saturation degrees aimed at examining influence of water saturation on creep of the claystone. Again, the bedding of both samples was parallel to their axes.

3.3.5.1 Creep of a highly saturated sample

Sample BLT-A8 had been pre-compacted at isostatic stress of 15 MPa for 7 days (figure 3.29), resulting in a decrease of the porosity from 8.3 % to 8.0 % and thus an increase of the saturation degree from 93 % to 96 %.

It was then followed by creep testing under multistep deviatoric stresses of $\Delta\sigma = \sigma_a - \sigma_r$ = 3 MPa for 1 month, 9 MPa for 3.5 months, 15 MPa for 5.5 months, and 24 MPa for 5 months. The mean stress was kept at σ_m = 13 MPa for the first three phases and then slightly increased to 14 MPa for the last phase. The temperature was controlled at 27.5±0.1 °C. The applied stresses and temperature, and the resulting axial, radial and volumetric strains are illustrated in figure 3.30a. It can be found that: a) strains could be hardly detected during the first phase at $\Delta\sigma$ = 3 MPa; b) each sudden increase in devia-

toric stress yielded a rapid deformation with axial compression, radial extension and volume dilatancy due to the relatively larger extension in radial direction normal to the bedding; c) under each constant stress state, the axial and radial strains continued with time from a transient phase to a steady state (fig. 3.30b); and d) the volume did not change much with time at deviatoric stresses of $\Delta\sigma \leq 15$ MPa, but at a deviatoric high stress of $\Delta\sigma = 24$ MPa at $\sigma_r = 6$ MPa, a dilation process evolved with time indicating a damage evolution. This dilatancy stress is slightly lower than that of the short-term compression tests on the samples with nearly the same saturation degrees of 95±5 %, as compared in figure 3.31. It seems that the damage of the claystone is little dependent of load duration.

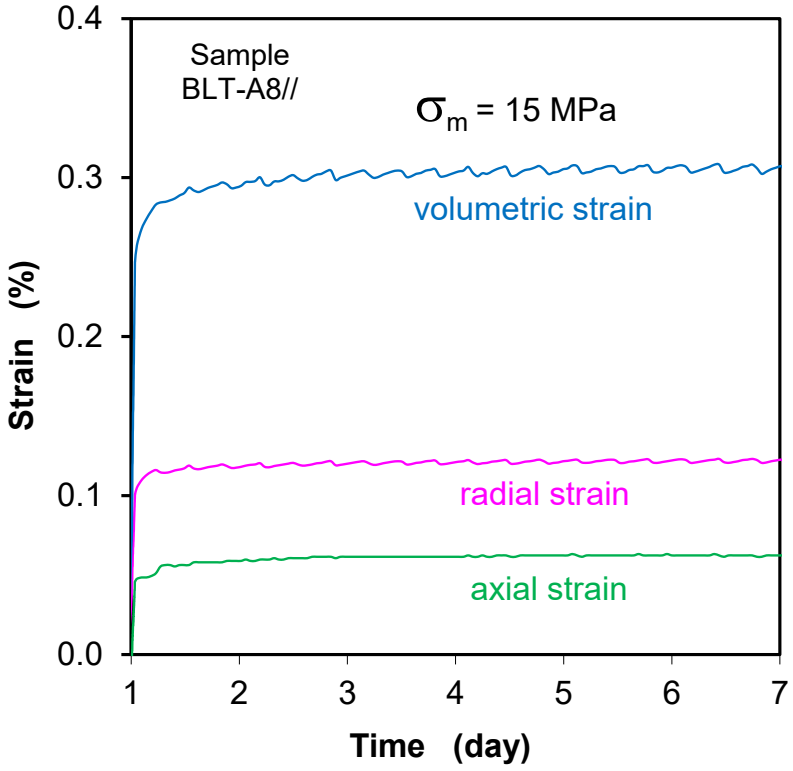

Fig. 3.29 Pre-compaction of the sample under the undrained isostatic stress conditions

From the strain – time curves, axial and radial strain rates at each load stage are derived and depicted in figure 3.34b against the time. The data show that the creep rates decreased with time during the first 2 – 3 months and then tended to steady state. The stationary creep rates were quite low in a range of 10^{-12} to 10^{-11} s^{-1}, which increased with increasing the deviatoric stress, i.e. the creep was accelerated by increasing the deviatoric stress.

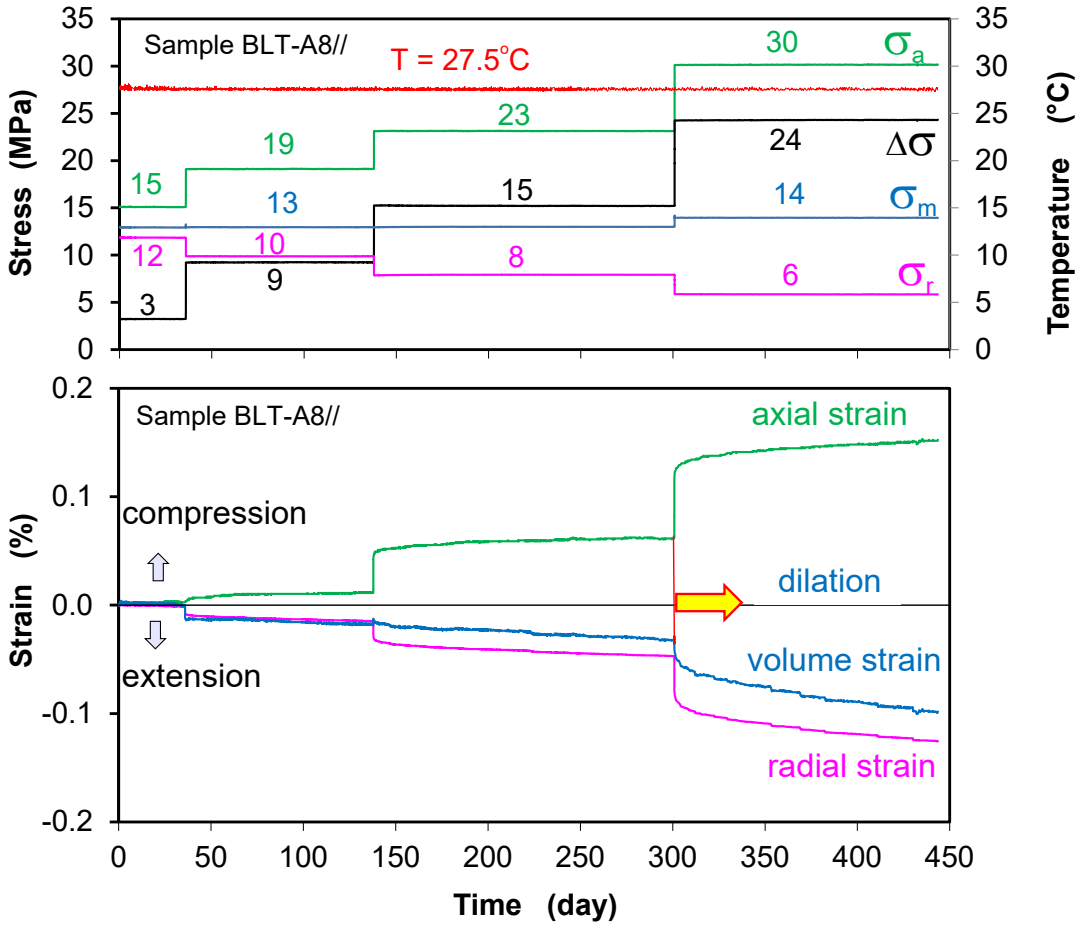

a. applied stresses and resulting axial / radial / volumetric strains

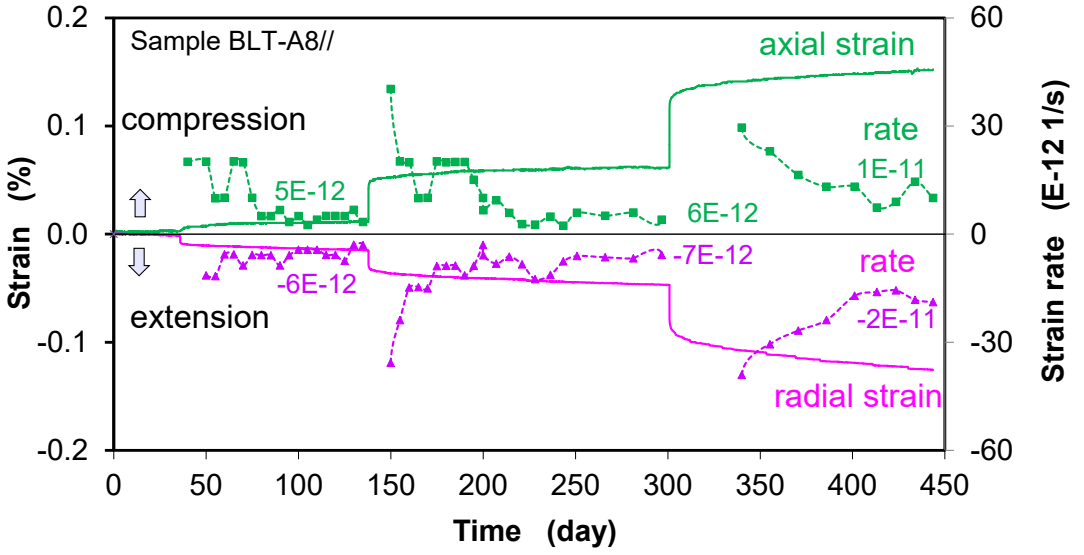

b. axial and radial strain rates

Fig. 3.30 Results of a multistep triaxial creep test on a highly-saturated sample

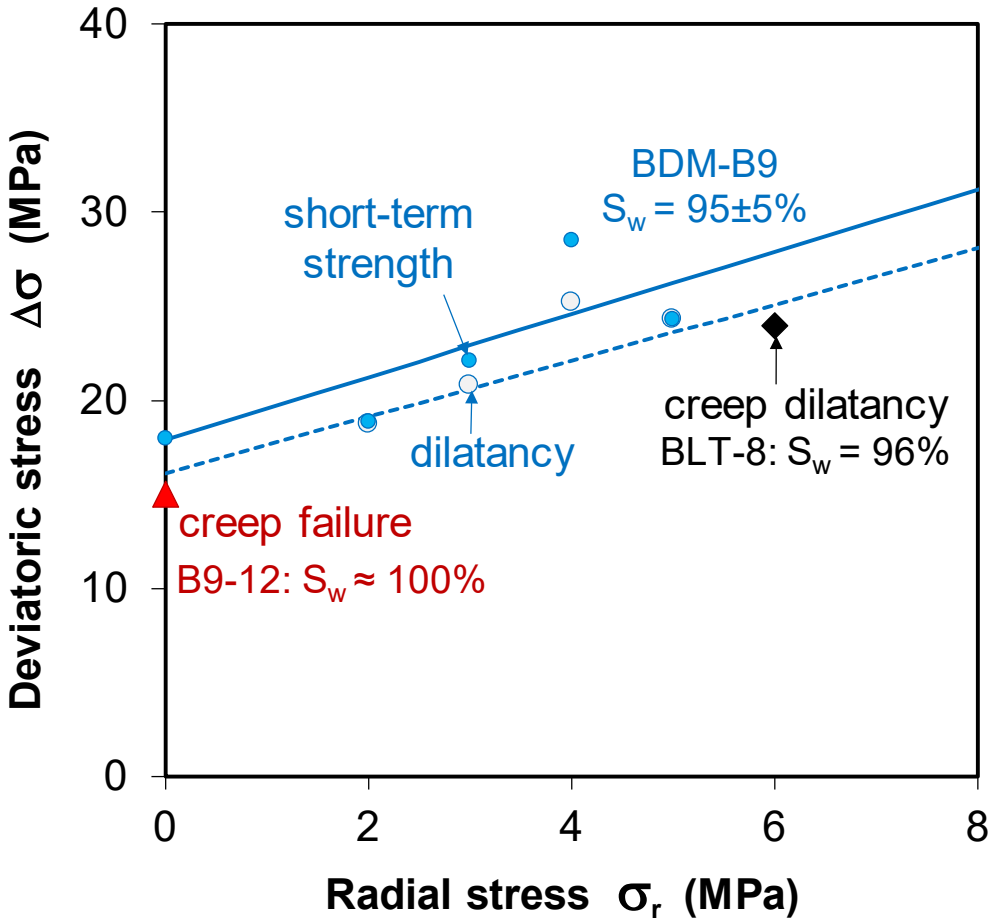

Fig. 3.31 Comparison of the dilatancy and peak strengths observed on the OPA sandy claystone during the short and long-term tests

3.3.5.2 Creep of saturated and unsaturated samples

In order to examine the influence of water saturation on creep of the OPA sandy claystone, a dried sample BDM-B9-11 with S_w = 27 % and a rewetted sample BDM-B9-12 with S_w = 98.5 % were tested under identical multistep loads: firstly pre-compacted at isostatic stress of σ_m = 13 MPa for 0.5 month and then increased deviatoric stress to $\Delta\sigma$ = 3 MPa for 0.5 month, 9 MPa for 1 month, and 15 MPa for another month at σ_m = 13 MPa. The temperature was ambient at 26 °C. Unfortunately, radial strain could not be monitored in the used creep rig. The applied stresses and the resulting axial strains are illustrated in figure 3.32a for both samples. The following lists the sequence of observations.

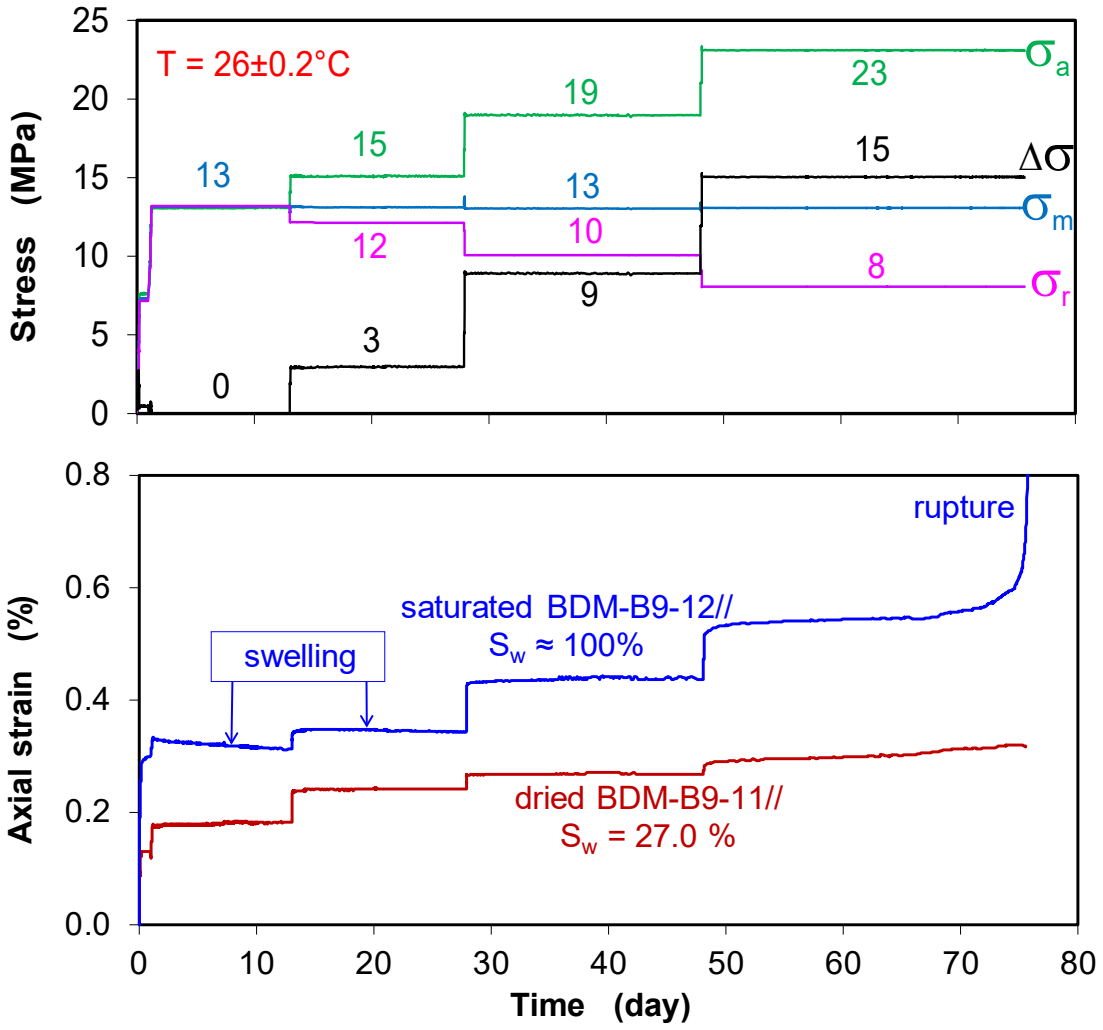

a. applied stresses and resulting axial strains

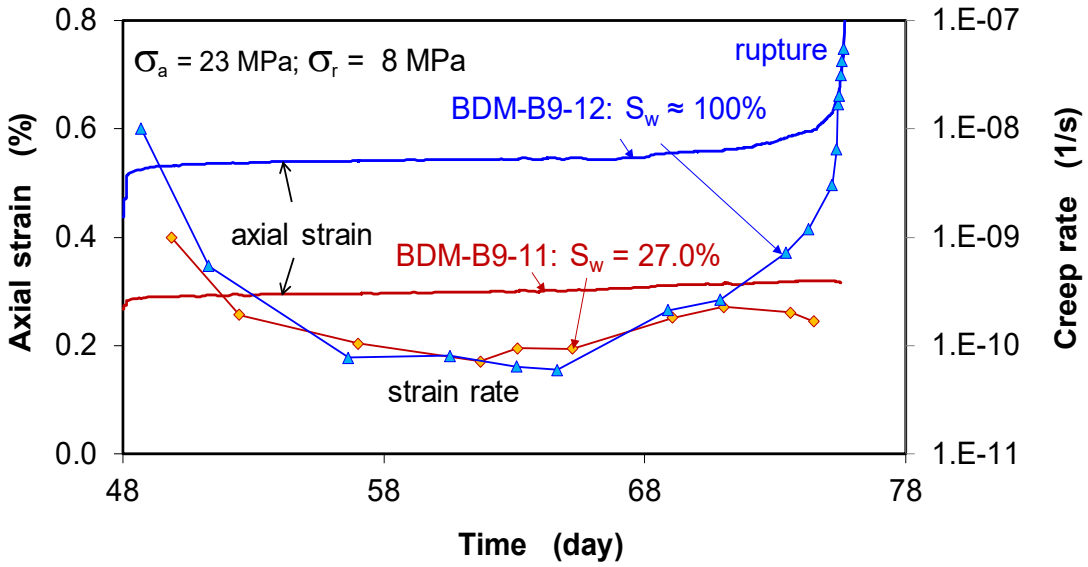

b. axial strains and rates during the last load phase

Fig. 3.32 Creep of the saturated and dried samples under multistep triaxial loads

First, the sudden isostatic compression resulted in rapid compaction. The wetted sample was more compacted to an axial strain of ε_a = 0.33 % than the dried one to ε_a = 0.19 %, again indicating more micro-cracks induced during sample resaturation. During the pre-compaction phase at the high load of σ_m = 13 MPa, the compaction of the dried sample terminated several days later, while the wetted sample exhibited a gradual expansion by $\Delta\varepsilon_a \approx$ -0.01 % rather than a compaction. This phenomenon remains enigmatic to us. It might be attributed to swelling effects from clay minerals in the sample. In the previous experiments /ZHA 17a/b/, some swelling was already observed on COX claystone even under the *in situ* rock stresses (σ_1 = 15 MPa $\sigma_2 = \sigma_3$ = 12 MPa) and porewater pressure of 4.5 MPa at URL Bure /ARM 14/. The pre-compaction might have led to a decrease in the thickness of water-films in interlayers in clay particles and to a decrease of distances between clay particles, in which the disjoining (swelling) pressures acting in the intra- and interparticle bound water might become higher than the external confining stress and in turn enlarge the thickness of the narrowed interlayers and interparticle distances until equilibrium. Additionally, the water in relatively large pores could be expelled into unsaturated pores, increasing the water saturation degree by 1 – 3 % as observed on the other samples and to approximately full saturation.

Following the pre-compaction phase, a low deviatoric stress phase of $\Delta\sigma = 3$ MPa was applied, under which entire time span the gradual axial expansion of the saturated sample continued. Following the above hypothesis of swelling and porewater pressure, this result implies that the internal swelling pressure acting in the interlayers of the clay minerals and the porewater pressure in the interparticle pore space must exceed the external (axial and radial) stress. As the axial stress was increased to 19 MPa and the radial stress decreased to 10 MPa ($\Delta\sigma = 9$ MPa), a very slow axial compression appeared at the saturated sample, but not at the dried one. A significant creep took place at both saturated and dried samples at further increased deviatoric stress of $\Delta\sigma = 15$ MPa ($\sigma_a = 23$ MPa, $\sigma_r = 8$ MPa). After about a month, the creep of the saturated sample then evolved with increased rates into rupture (fig. 3.32b). Before the failure, the creep rates of both saturated and dried samples are quite similar with a transient phase in the beginning and the following stationary phase, which lasted for a short time at the saturated sample.

Compared to the short-term strength of 30 MPa at $\sigma_r = 8$ MPa determined on the highly-saturated samples with S_w = 95±5 % (fig. 3.35), the creep rupture stress of 15 MPa seems to be quite low. Similar low creep rupture stresses were also observed on the

highly saturated COX samples in undrained conditions /ZHA 19/. The low creep rupture stresses observed might be caused (1) by high internal swelling pressures that built up in the interlayers in clay particles and in the interparticle narrow pore space and (2) by high water pressures increased in the large pores under the previously applied high radial stress. The internal pore pressures, particularly the swelling pressures, could exceed the reduced external radial stress, resulting in a decrease in effective stress down to zero and even possibly to negative values (tensile state). At the lowered effective radial stress, the applied deviatoric stress could yield failure as illustrated in figure 3.31 by assuming zero effective radial stress. This creep failure stress is slightly lower than the uniaxial strength. This hypothesis needs to be confirmed by undrained triaxial creep testing with monitoring porewater pressure.

3.3.5.3 Stationary creep rate

The stationary shear creep rates, $\dot{\varepsilon} = \frac{2}{3}|\dot{\varepsilon}_{\mathrm{a}} - \dot{\varepsilon}_{\mathrm{r}}|$, obtained on the OPA sandy facies (sample BLT-A8) are compared in figure 3.33 with those of the clay-rich OPA shaly facies and the COX claystone at the -490 m level of the URL Bure /ZHA 13/15/. The COX claystone contains clay minerals of 50 – 55 %, carbonates of 202 – 5 %, quartz of ~20 % and others of ~3 % /ARM 14/. All the tested samples were highly water-saturated with degrees of larger than 95 % and the testing temperatures were comparable in a range of 25 °C to 28 °C. The comparison shows that the OPA sandy claystone crept more slowly than the clay-rich ones at a given deviatoric stress, i.e. the creep rate increases with increasing clay content.

Mitchell /MIT 92/ derived a constitutive equation for creep of clay soils through thermodynamical analysis of soil flow by application of the absolute reaction-rate theory. This model was slightly modified and applied by Zhang /ZHA 13/15/ for the stationary creep of clay rocks

$$\dot{\varepsilon} = A\ \exp\left(-\frac{Q}{RT}\right)\ \sinh(\alpha \cdot \Delta\sigma) \qquad (3.4)$$

where $\dot{\varepsilon}$ is the stationary shear creep rate (s^{-1}), $\Delta\sigma$ the deviatoric stress (MPa), T the absolute temperature (K), R the universal gas constant ($8.31433 \cdot 10^{-3}$ $kJmol^{-1}K^{-1}$), Q the apparent activation energy ($kJmol^{-1}$), A a parameter in s^{-1}, and α a parameter in MPa^{-1}. These parameters were established: $A = 2 \cdot 10^{-4}$ s^{-1}, $\alpha = 0.2$ MPa^{-1}, and $Q = 45$ $kJmol^{-1}$

for the COX claystone /ZHA 13/; and $A = 6 \cdot 10^{-4}\ s^{-1}$, $\alpha = 2\ MPa^{-1}$, and $Q = 45\ kJmol^{-1}$ for the OPA sandy claystone. Figure 3.33 shows a reasonable agreement between the model (solid line) and the data for the respective claystone. However, please note also that the observed volumetric deformation (consolidation and/or dilatancy) with time is not yet taken into account in the creep equation. Particularly, dilatancy or damage induced by excavation accelerates drift convergence as observed in the URLs Mont-Terri /BOS 17/ and Bure /ARM 14/. The damage effect on the long-term deformation needs to be involved in the creep models for predicting long-term performance of the potential repositories in the OPA and COX formations.

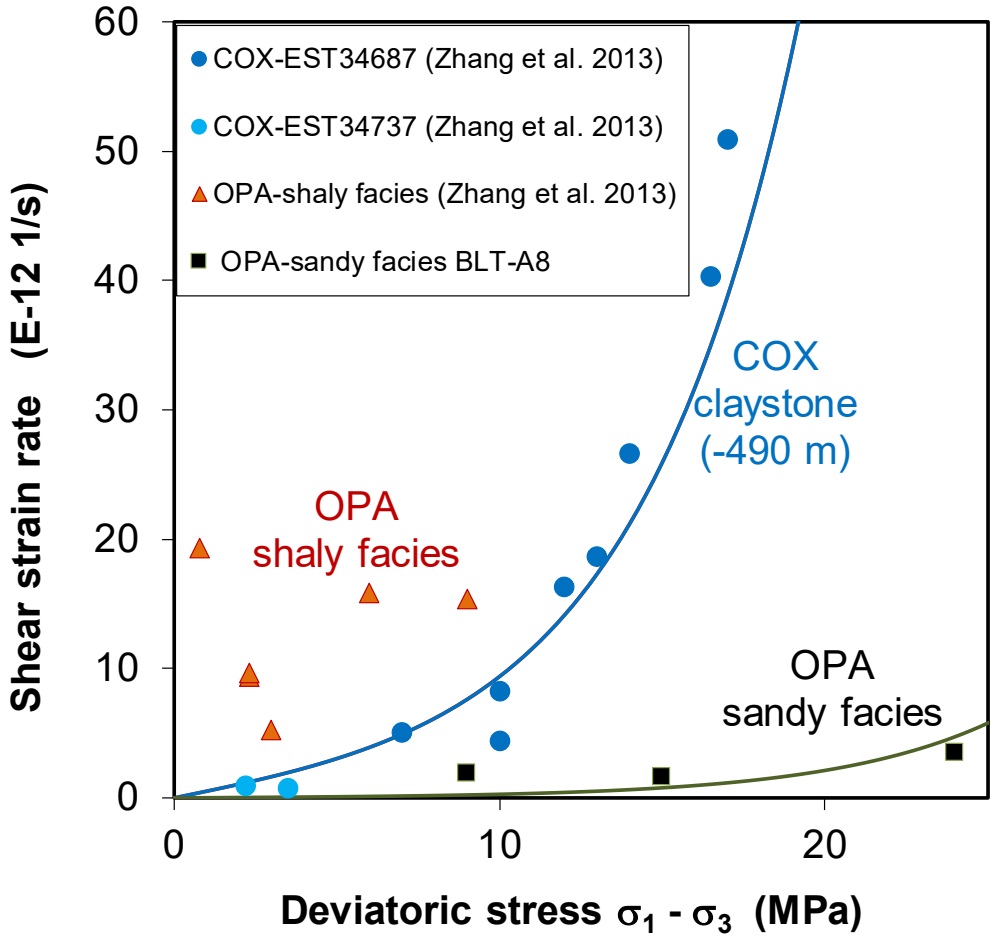

Fig. 3.33 Comparison of the steady-state creep rates between the OPA sandy claystone and the clay-rich OPA and COX claystones

At low stresses of $\Delta\sigma \leq 24$ MPa for the OPA sandy claystone and $\Delta\sigma \leq 10$ MPa for the COX claystone, the creep rate is linearly related to the stress. According to /RUT 83/ and /LIU 18/, the linear stress/strain rate relation implicates that the time-dependent deformation of water-saturated claystone is controlled by diffusive mass transfer or pres-

sure solution processes in interfaces between grains. One of the required conditions for diffusive transport is the existence of interparticle water-films, which must be so strongly adsorbed onto grain surfaces that they are able to support shear stress without being squeezed out. As demonstrated in /HOR 96/ and /ZHA 17a/b/, large amounts of the porewater in the studied claystones are strongly adsorbed between clay particles and capable of sustaining high shear stresses up to the material strength. At high stresses, the creep rate increases rather exponentially, as shown by the COX claystone (Fig. 3.37). This might be contributed by more rapid slips of water-films at interparticle contacts and additionally micro-cracking along the particle boundaries. Accumulation of the micro-cracks could lead to macro-fractures and ultimately to creep-failure. This micro-structural hypothesis requests to be validated by microscopic observations.

Laboratory investigation of the long-term deformability of claystones is a big challenge due to the high sensitivity of the material to environment variations and strong thermo-hydro-mechanical-chemical coupling effects. In addition to the requirements on the short-term testing with careful sampling and reconditioning, specific methodologies are required in creep tests: They need more precisely controlled boundary conditions, precise measurements of deformation, pore pressure and other parameters during long time periods of months to years at each load step. Maintaining such accurate and precise measurement equipment for these long runtimes is ambitious. Micro-structural observation and analysis of the creeping material might give relevant insights to understand the micro-processes and identify the creep mechanisms. However, even after long runtimes, the sample deformations are marginally small and it is uncertain if those strains can be identified, even in using electron microscopy. Based on the creep tests and micro-structure observations, constitutive models shall be developed, validated by comparison with qualified laboratory and *in situ* test data, and then applied for the (numerical) prediction of the long-term deformation of the clay host rock under repository conditions.

4 Moisture effects

Ventilation of excavated repository openings in clay rock will lead to desaturation of the surrounding rock (EDZ). As the openings are backfilled and sealed with relatively dry clay-based materials, the clay rock on the backfill/seal side will be more desaturated. On the other side, water in the clay formation migrates from the saturated far-field towards the unsaturated EDZ and increases the saturation of the clay rock and backfill/seal until a hydraulic equilibrium will be reached in the rock-backfill/seal system. The saturation process in the clay-based backfill/seal will result in a development of swelling pressure, which is thought to prevent further extension of the EDZ and closes fractures in the EDZ. Fracture interstices tend to seal due to swelling of clay minerals during the resaturation of the EDZ. As observed previously on the clay-rich shaly facies of OPA and the COX claystone /ZHA 07/10/13/, de- and resaturation result in shrinking and swelling and variations of the stiffness and strength of the claystones. The de- and resaturation processes are controlled by their matric suction of the claystones. In the framework of this project, water uptake and retention capacity as well as moisture effects on the sandy OPA claystone were investigated on samples from the OPA sandy facies at URL Mont-Terri.

4.1 Water uptake and free swelling

Water uptake and retention capacity of a clay material is governed by its suction. The relationship between water content (or saturation degree) and suction is called water retention curve, which is one of the most important characteristics of the material. Water retention curves of the OPA sandy claystone at different locations were determined using vapour transfer technique.

4.1.1 Samples

A large number of core samples from boreholes BDM-B9 and BLT-A8/9/10 were examined. Most of the samples were prepared to a size of 70 mm in diameter and 20 mm in height. Figure 4.1 pictures two core samples and a powder sample in unconfined conditions. The initial characteristics of the core samples are summarized in table 2.6 for samples from borehole BDM-B9 and in table 2.7 for samples from boreholes BLT-A8/9/10, respectively. The main minerals of the claystone from borehole BDM-B9 are given in table 2.1. The samples BDM-B9 were divided in three groups: A, B and C. Samples from A and B derived from the same locations to ensure reproducibility and accuracy of the measurements, whereas samples from C are about 5 meters in distance to the locations of A and B. The sample properties show a spatial variability (cf. figure 2.5), indicating the distinct heterogeneity of the sandy facies. In addition to the core samples, fine-grained powder samples were produced during the preparation of the group A and B samples, too. Due to the sampling, the samples were desaturated to degrees of 55 – 78 % (cf. figure 2.6).

Fig. 4.1 Pictures of the powder and disc samples from borehole BDM-B9 for measurement of water retention properties

Additionally, the water retention capacities of the OPA sandy facies from boreholes BLT-A8/9/10 were determined on 24 core pieces of 40 grams each (figure 4.2). The average properties of these are given in table 2.7.

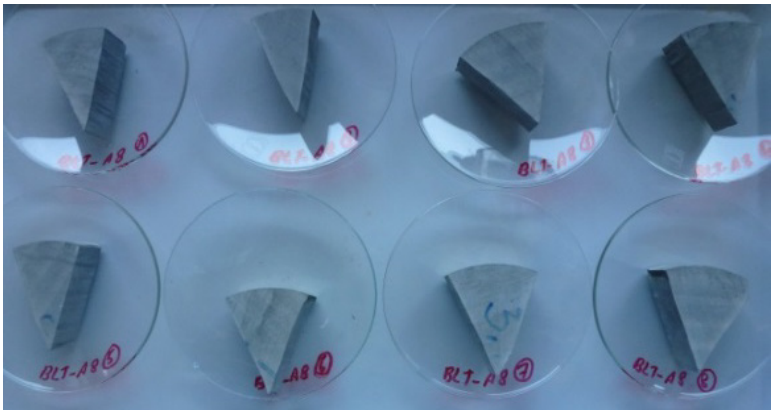

OPA-BLT-A8

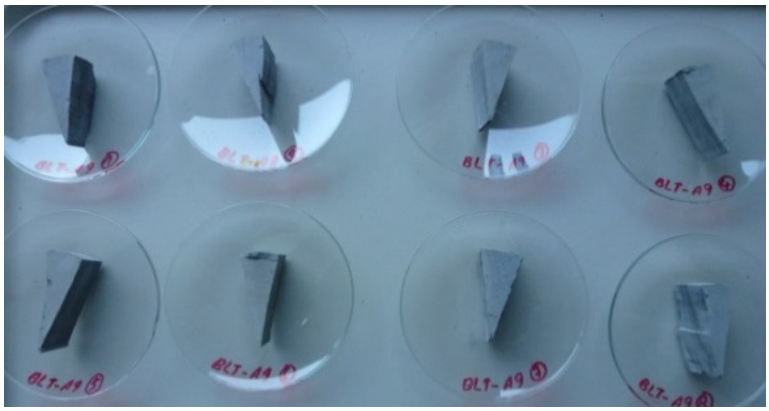

OPA-BLT-A9

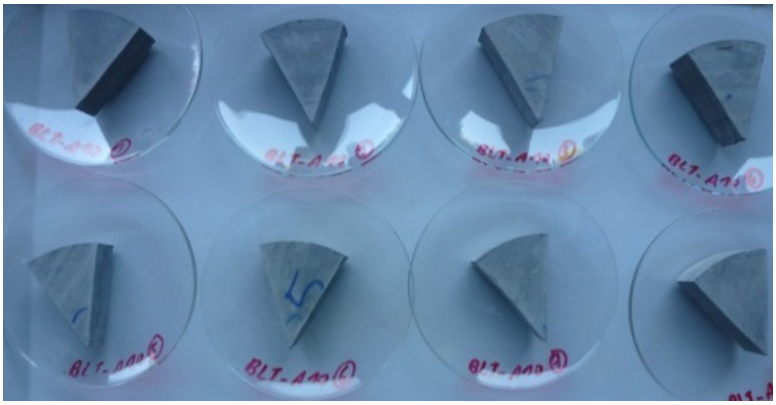

OPA-BLT-A10

Fig. 4.2 Pictures of the OPA sandy claystone samples OPA-BLT-A8/9/10 for measurement of water retention properties

4.1.2 Test methodology

The samples were unconfined and placed in individual desiccators at different relative humidity values of RH = 30 % to 100 % (figure 4.3). The RH-values were adjusted by means of different saturated salt solutions as used in the previous tests on the clay-rich OPA and COX claystones /ZHA 10/13/. The corresponding suctions are determined according to Kelvin's law /FRE 93/

$$s = -\frac{\rho_w RT}{M_w}\ln(RH) \qquad (4.1)$$

where s = suction, T = absolute temperature, R = universal gas constant, ρ_w and M_w are the density and the molecular mass of water, respectively. The applied suctions are in a range of 0 to 160 MPa at the testing temperature of 24° C. The relative humidity in each desiccator was continuously recorded by transistor psychrometer sensors, while the water content and volume of each sample was measured at time intervals of 1 – 3 months. Water content was determined by weighing, sample volume change was determined by measurement of its diameter and height at four positions using callipers. The total durations lasted for 9 to 12 months until equilibrium. Subsequent, the samples in groups B and C were dried at 105 °C, while the samples in A were not.

Fig. 4.3 Measurement of water retention properties of the samples in desiccators at different relative humidities

This procedure was followed by contacting the samples to liquid water to determine their maximum capacities of water uptake. The samples were put on porous plates with contact to synthetic OPA water, which was produced according to the chemistry of the pore water in the OPA claystone /PER 99/ with main components: Na [240 mmol/l], Cl [300 mmol/l], Mg [16.9 mmol/l], Ca [25.8 mmol/l], SO4 [14.1 mmol/l] and small amounts of others. After stabilisation of the water uptake, all the samples were dried at 105 °C and weighted for the final determination of the maximal water content.

4.1.3 Test results

4.1.3.1 Water uptake and free swelling in humid air

Figures 4.4a-d illustrate the evolution of water content and volumetric strain measured on the OPA sandy-clay samples from borehole BDM-B9 at different humidities of RH = 30.5 % to 100 %. The data of measured water content indicate that water uptake or release is dependent upon the initial water content and the applied humidity or suction. When the samples with low initial water contents are exposed to humid environment, water uptake occurs; and in contrast, the pore water evaporates and moves out of the pore space when the highly-saturated samples contact dry air. The processes of water uptake and release tend to stabilize with time. In case of the applied sample size of D/L = 70/20 mm, desaturation process to equilibrium needs relatively short time periods of 1 – 2 months at RH < 97.5 % (s > 3 MPa), while resaturation at RH = 100 % or zero suction to equilibrium needs longer time periods up to 4 – 5 months.

In correspondence to the variation of the water content, the volume of the samples varied. At RH < 97.5 % (s > 3 MPa), most of the samples were desaturated and shrunk more or less, depending on the difference between the initial and remaining water content. The shrinkage observed on the partly-saturated samples with S_w = 55 % to 78 % is limited within 0.7 %. In In humid conditions at RH = 100% (s = 0), the unconfined samples took up water and expanded to a volume increase up to 2.0 %. This confirms that de-stressing of the claystone by coring leads to development of suction even without water release /HOR 96/. The unloading-induced suction draws water from humid environment into the pore space and results in swelling of the claystone under unconfined conditions. The same phenomenon was also observed on the clay-rich OPA and COX claystones /ZHA 10/15/17a/b/. The characteristics of the samples determined in

equilibrium at the individual humidities (RH) or suctions (s) are summarized in table 4.1, including bulk density ρ_{bs}, dry density ρ_{ds}, porosity ϕ_s and water content w_s.

The water content w and volumetric strain ε_v at equilibrium states are illustrated in figures 4.5a and 4.5b as function of suction s for the samples from borehole BDM-B9. The water retention curves (w-s, figure 4.5a) show that the water content increases with decreasing suction. At low suctions s < 3 MPa, the water content rises sharply to the maximum w_{sm} at zero suction: w_{sm} = 5.4 % for samples in groups A-B, w_{sm} = 4.0 % for group C, and w_{sm} = 7.1 % for the powder samples. The higher water content observed on the powder compared to the core samples might be caused by high specific surface of its fine grains, more accessible pores and easier swelling conditions for clay particles as they are not confined by the rock's fabric. Whereas the w-s curves of the samples in groups A-B from the same location are consistent with each other, the curve of group C is relatively lower at suctions s < 30 MPa.

Moreover, the other samples from boreholes BLT-A8/9/10 also exhibited some differences in water retention properties with different water contents of w_{sm} = 7 – 9 % at zero suction (see figure 4.6). The heterogeneous water retention properties are likely attributed to the heterogeneities of the mineralogical composition.

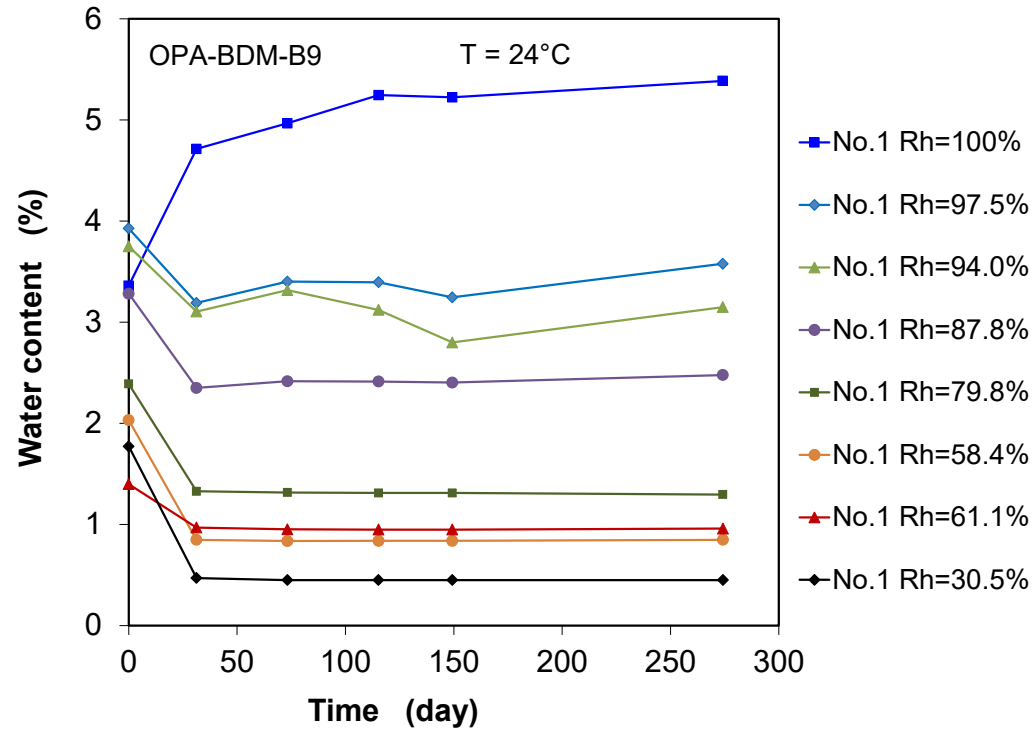

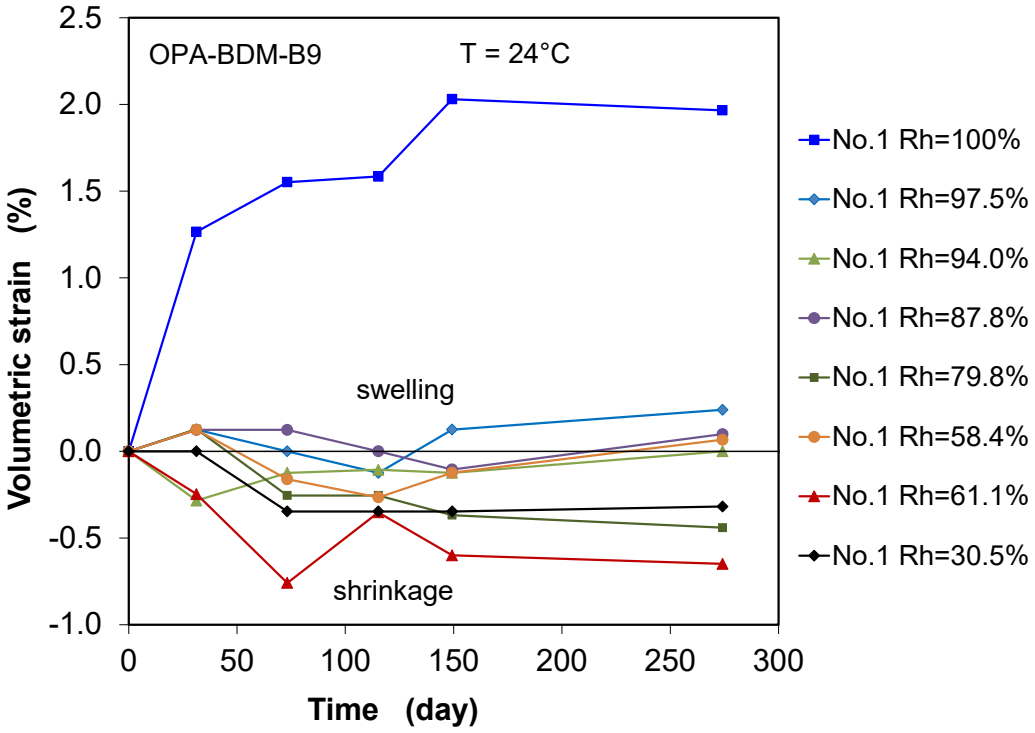

a. Core samples in group A

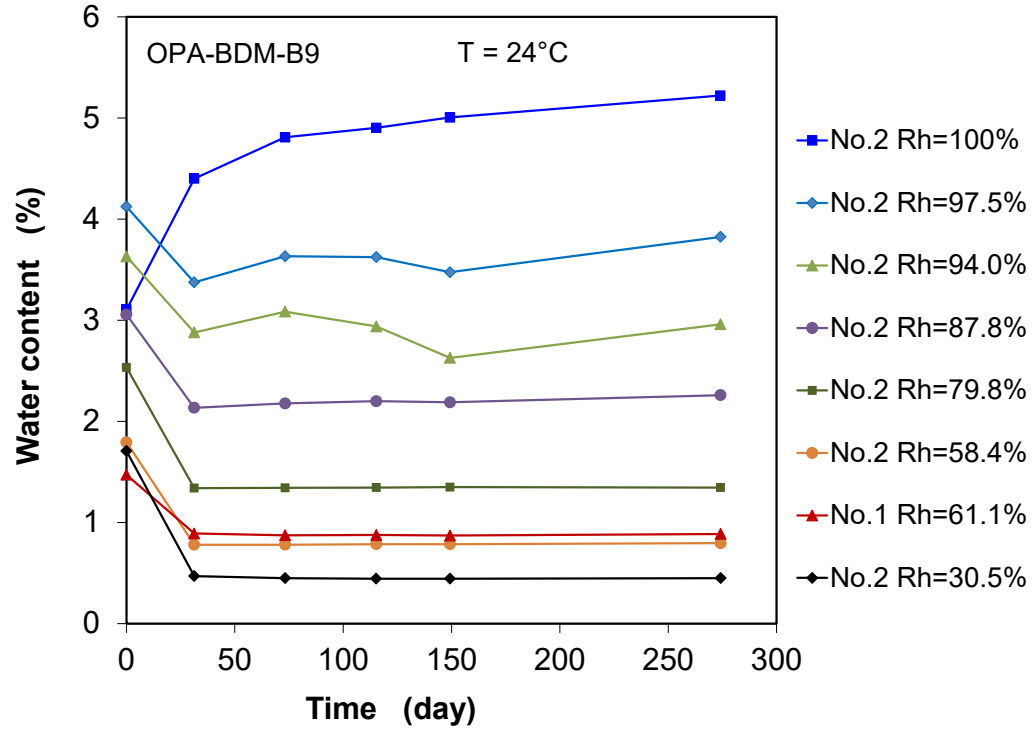

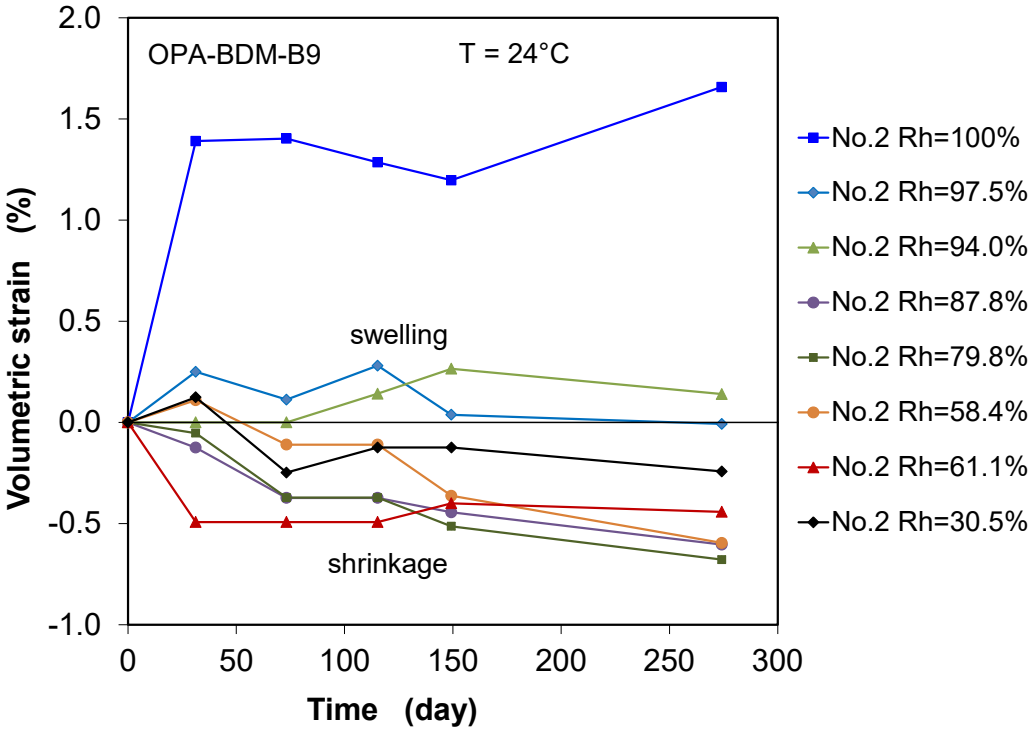

b. Core samples in group B

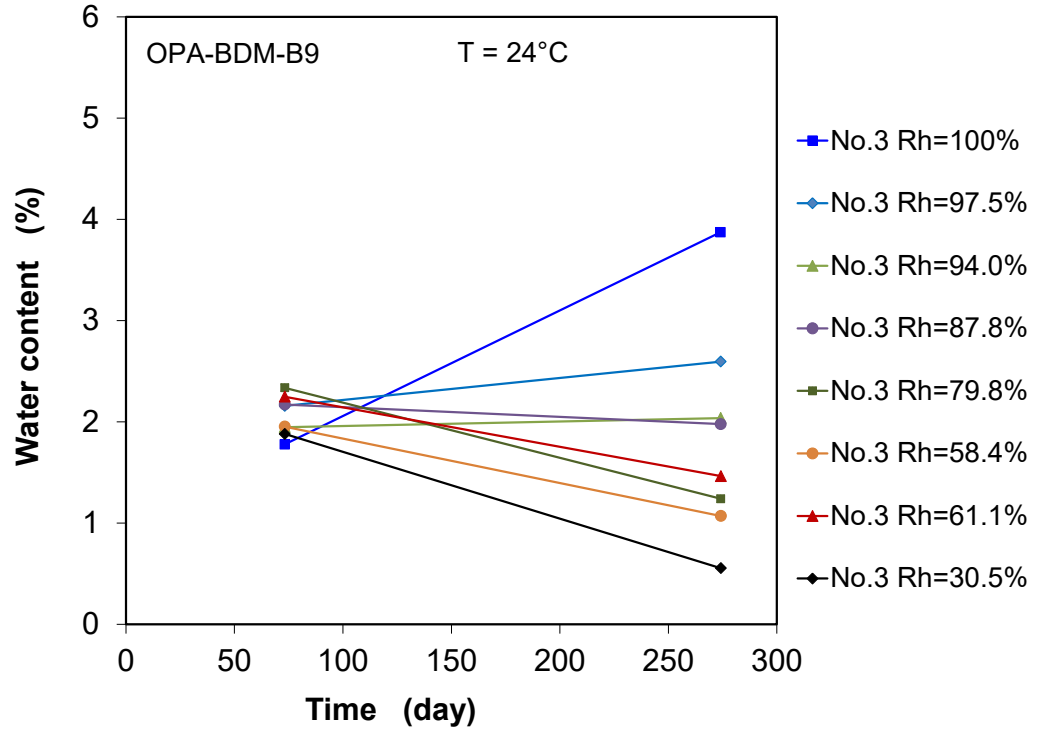

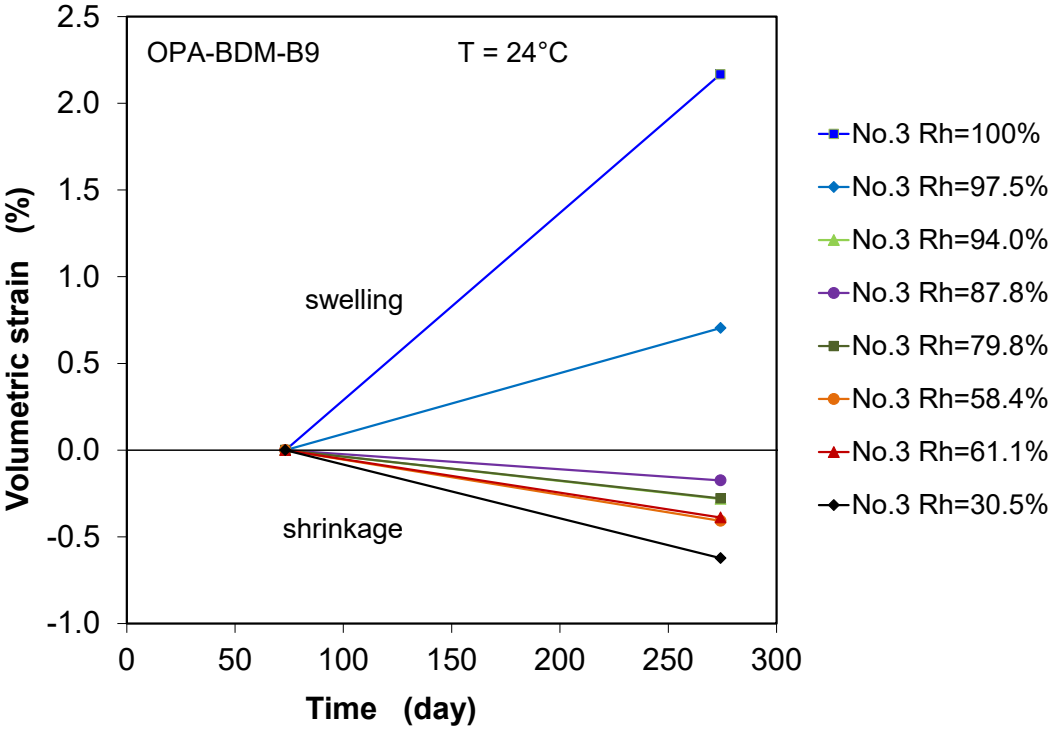

c. Core samples in group C

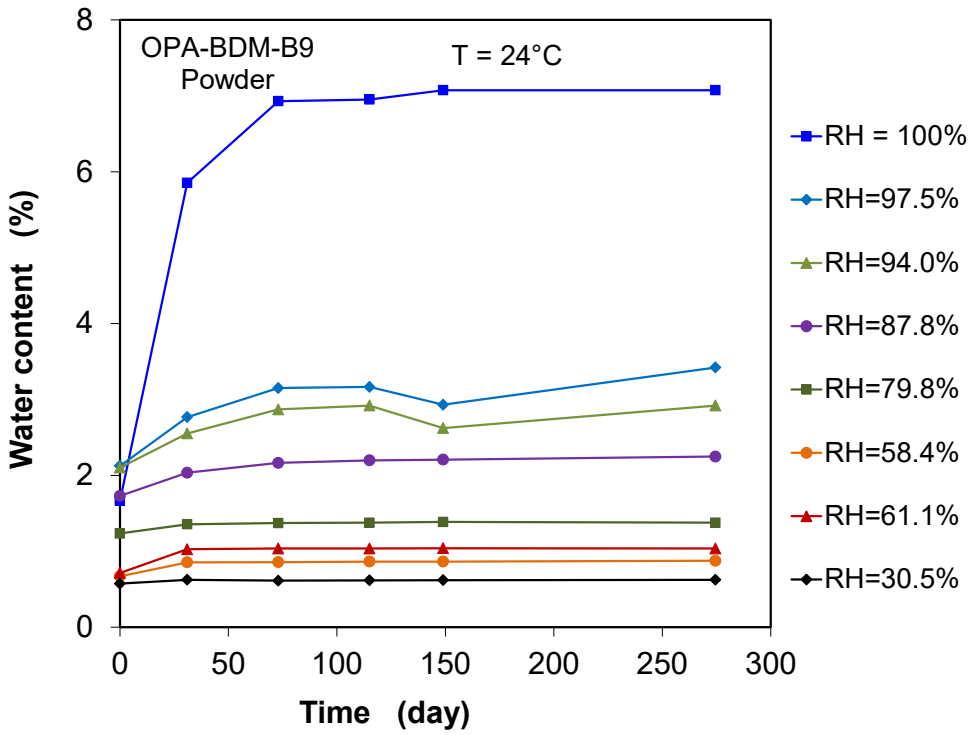

d. Powder samples in group D

Fig. 4.4 Evolution of water content and volumetric strain observed on the OPA sandy-clay samples in different humid conditions

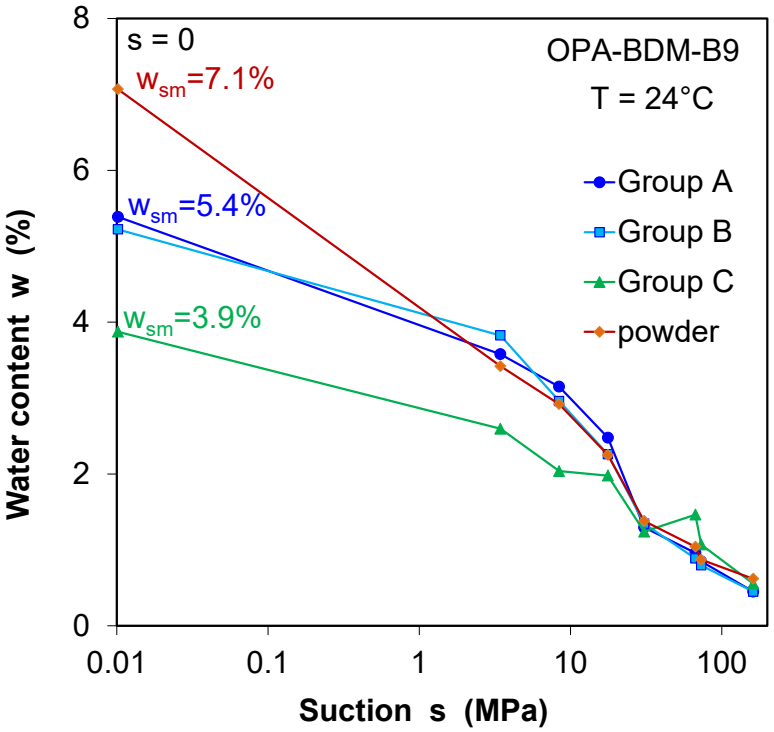

a. Water content – suction

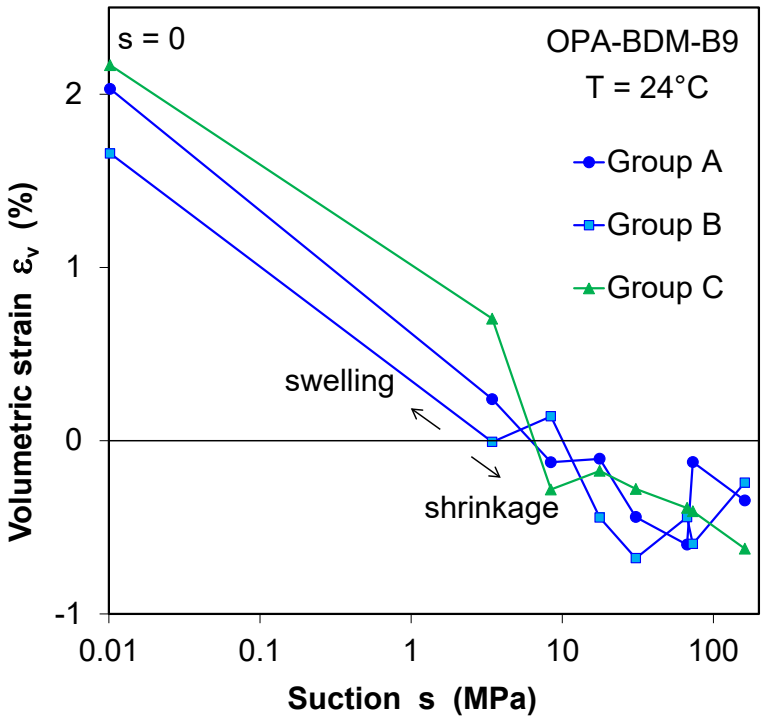

b. Volumetric strain – suction

Fig. 4.5 Water contents and volumetric strains of the OPA sandy claystone from borehole BDM-B9 at different suctions

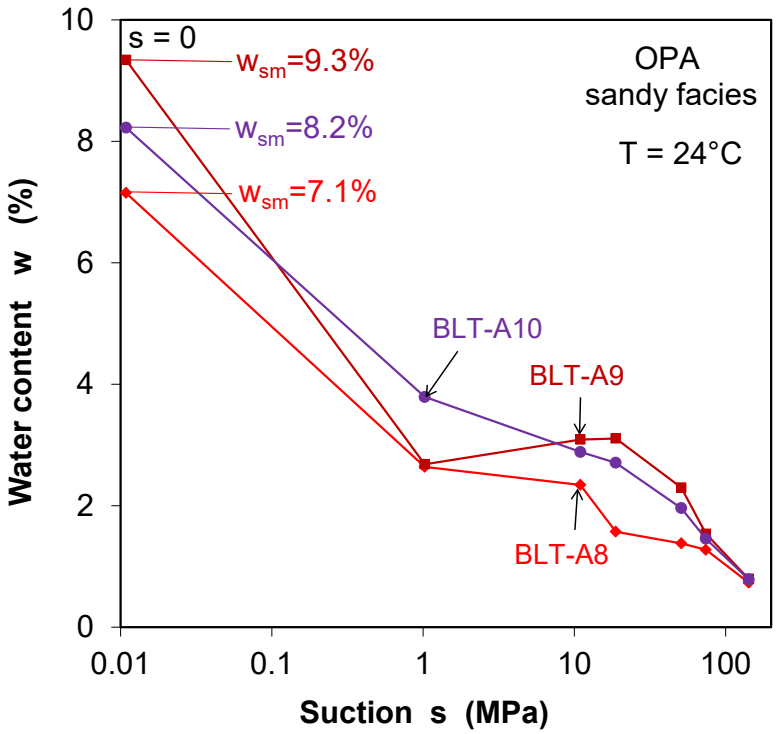

Fig. 4.6 Water retention curves of the OPA sandy claystone from different boreholes BLT-A8/9/10

Tab. 4.1 Final characteristics of the samples in equilibrium at different humid conditions and maximal water contents reached by wetting with synthetic water

Sample	Initial characteristics			Data obtained at different suctions			Maximal **water content** w_{max} **(%)**
Group A	**Borehole depth (m)**	**Porosity ϕ_o (%)**	**Water content w_o (%)**	**Suction s (MPa)**	**Porosity ϕ_s (%)**	**Water content w_s (%)**	
B9-1a	6.21	12.71	3.36	0.0	14.54	5.39	9.05
B9-2a	6.45	13.51	3.93	3.4	13.70	3.58	11.90
B9-3a	6.71	13.30	3.75	8.2	13.26	3.15	13.25
B9-4a	6.94	11.30	3.28	17.7	11.35	2.48	9.21
B9-5a	7.28	8.51	2.39	30.7	8.07	1.30	5.39
B9-6a	7.53	6.77	2.03	73.1	6.80	0.85	2.70
B9-7a	7.78	6.48	1.40	66.9	5.85	0.96	3.33
B9-8a	8.06	6.57	1.77	161.3	6.22	0.45	3.27
Group B							
B9-1b	6.22	12.24	3.11	0.0	13.82	5.22	8.90
B9-2b	6.47	13.71	4.12	3.4	13.68	3.82	6.84
B9-3b	6.72	12.72	3.63	8.2	12.81	2.96	11.19
B9-4b	6.95	11.92	3.06	17.7	11.35	2.26	7.80
B9-5b	7.29	9.11	2.53	30.7	8.44	1.35	5.25
B9-6b	7.54	6.81	1.79	73.1	6.22	0.80	2.70
B9-7b	7.79	5.91	1.47	66.9	5.48	0.89	3.25
B9-8b	8.07	6.60	1.71	161.3	6.35	0.45	3.41
Group C							
B9-26a	12.13	7.30	1.78	0.0	9.37	3.87	5.98
B9-26b	12.14	8.57	2.16	3.4	9.23	2.60	6.84
B9-26c	12.15	8.79	1.95	8.2	8.54	2.04	6.21
B9-26d	12.16	8.12	2.17	17.7	7.95	1.98	5.73
B9-27a	12.30	7.49	2.34	30.7	7.19	1.24	5.04
B9-27b	12.31	7.94	1.95	73.1	7.54	1.07	5.50
B9-27c	12.32	8.27	2.25	66.9	7.88	1.46	5.12
B9-27d	12.33	8.09	1.88	161.3	7.48	0.55	5.20

4.1.3.2 Water uptake and free swelling in clay solution

Following the measurements of water content and volume changes at the different humidities, the core samples were then wetted with OPA synthetic pore water in order to determine maximal water uptake or water adsorption capacity of the sandy claystone. The samples were placed on porous plates and filter papers, which are directly contacted to the water, as shown in figure 4.7. Whereas the samples in group A were directly contacted to the water, the other samples in groups B and C had been dried at 105 °C before contacting the solution.

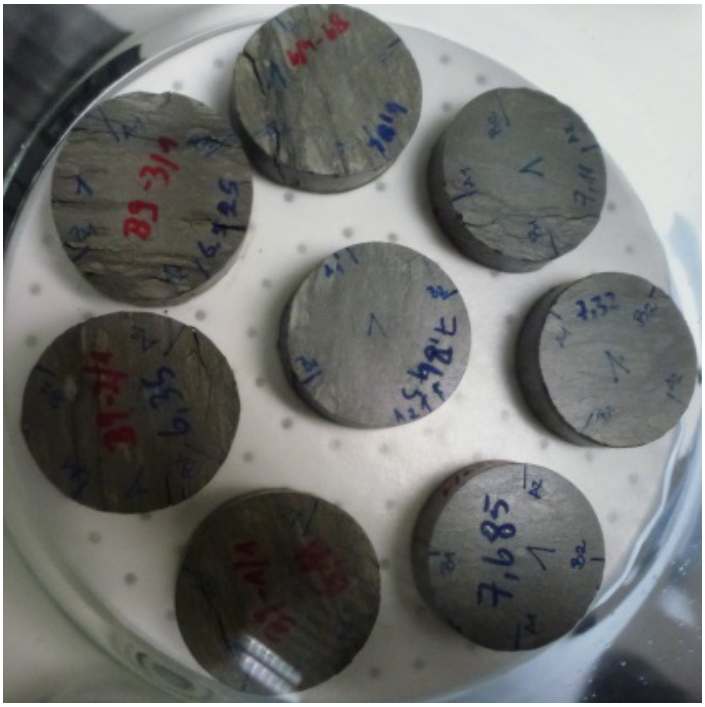

Group A:
Samples wetted with
synthetic OPA clay water

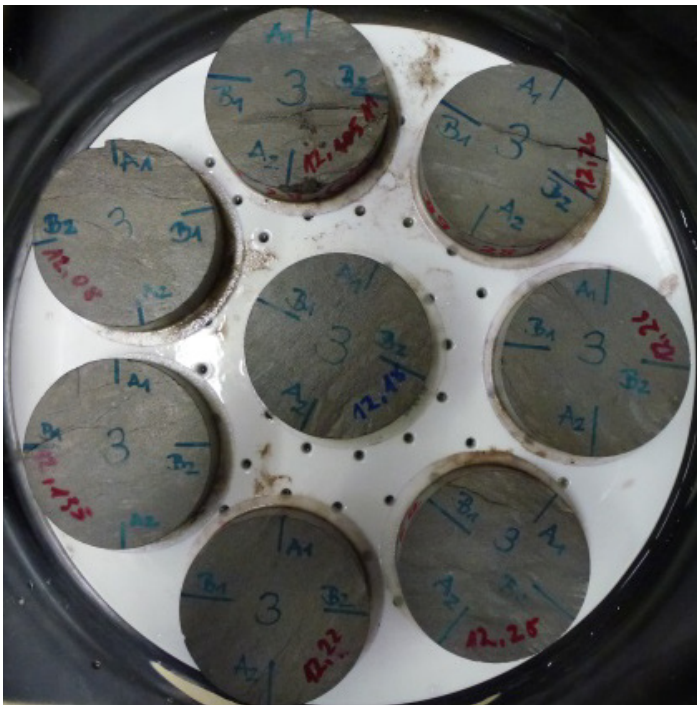

Group C:
Samples wetted with
synthetic OPA clay water

Fig. 4.7 Samples wetted by contacting to synthetic clay water at bottom

It was observed that when the samples were contacted to the liquid phase, the water uptake increased rapidly and reached a maximum w_{max} at each sample within days. The maximal water contents w_{max} achieved in contact with the water are summarised in table 4.1. Comparing the water contents w_{sm} = 5.4 % and 3.9 % reached in water va-

pour (s = 0) at samples B9-1/a/b and B9-26/a, one can recognize that the claystone takes up more water during contact with the liquid phase to a maximum w_{max} = 9.0 % and 6.0%, respectively. We propose two causations for this phenomenon. The first and likely the dominant causation are capillary effects that fill larger cracks with water (see crack in figure 4.8). The water immersion could have led to localized disintegration of the microstructure, which might have led (1) to access of initially isolated porosities and (2) to the generation of fracture voids between clay particles and/or bedding planes. Similar observations were made by Stavropoulou1 et al. /STA 18/ on unconfined COX claystone during contacting with liquid water, too. They suggested that the cracking results from breakdown in capillary suction due to water arrival, which decreases the effective bound stress, leading to locally heterogeneous swelling of heterogeneously distributed clay minerals and causing crack opening in between bedding planes.

Fig. 4.8 Cracks generated in the OPA sandy claystone by water penetration

The maximal water content w_{max} data obtained on the core samples (table 4.1) are depicted in figure 4.9a as function of the initial porosity ϕ_o. It can be found that the water uptake capacity of the claystone increases with increasing the porosity. Houben et al. /HOU 14/ showed that the porosity is positively correlated to the clay matrix content, as it accounts for more than 50 % of the porosity visible in broad-ion-beam scanning electron microscopy. High amounts of clay minerals result in more water uptake and swelling. Clay contents of the samples were not directly measured on them but might be estimated by the values of 25 – 40 % obtained from some other samples from the same borehole BDM-B9 (table 2.1).

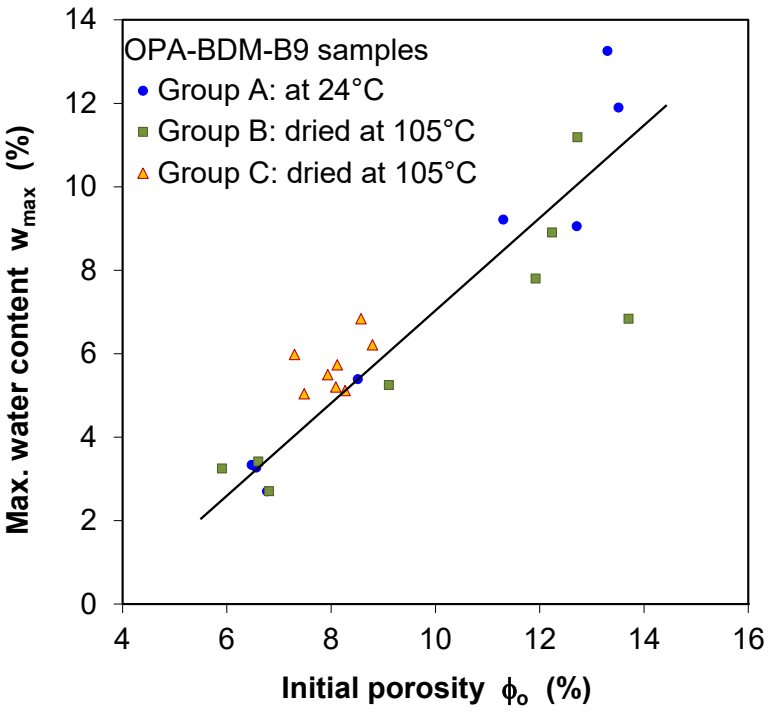

a. Maximum water content

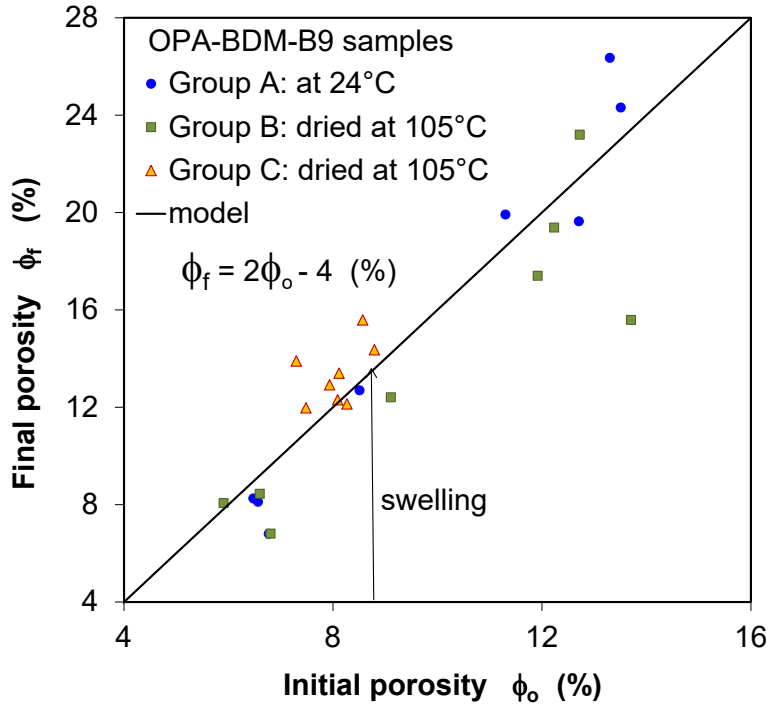

b. Final porosity

Fig. 4.9 Maximum water contents and final porosities of the OPA sandy claystone samples after saturation in synthetic clay water

Assuming that each sample contacting to the liquid is fully saturated at the reached maximum water content w_{max}, the final porosity can be obtained from the definition of degree of water saturation

$$S_w = w_{max} \frac{(1-\varphi_f)}{\varphi_f} \frac{\rho_s}{\rho_w} \tag{4.2}$$

where ρ_s is the grain density (2.70 g/cm^3) and ρ_w is the water density (1.0 g/cm^3). For full saturation $S_w = 100$ % at w_{max}, the porosity φ_f is determined by rewriting equation (4.2) as

$$\varphi_f = \frac{1}{1+\frac{S_w \cdot \rho_w}{w_{max} \cdot \rho_s}} \tag{4.3}$$

The calculated final porosities are depicted in figure 4.9b for the samples in relation to their initial porosities ($\phi_f - \phi_o$). The free swelling in the liquid water increased the porosity by 30 % – 80 %. The final porosity is linearly related to the initial one, which may be used for estimation of the maximum free swelling of the claystone in the clay water.

4.1.3.3 Water retention behaviour

The water content of the claystone in humid environment is controlled by its matrix suction (equation 4.1). The relationship between water content w and suction s is called water retention curve. Figure 4.10 depicts the water contents reached in equilibrium at each suction value for the samples from borehole BDM-B9 and BLTA-8/9/10, respectively. For each group of samples, the water content increases with decreasing suction. At zero suction, the water content reaches the maximum w_m. Each water retention curve is approximated by the van Genuchten model /VAN 80/:

$$w = w_m \cdot \left[1 + \left(\frac{s}{P_{ow}}\right)^{\frac{1}{1-\beta}}\right]^{-\beta} \tag{4.4}$$

where P_{ow} and β are the material parameters. The parameter values are estimated by fitting the $w - s$ data for each group of samples as summarized in table 4.2. The parameter values are different between the samples. The model reasonably agrees with the measured data, except for the overestimation at s = 1 MPa for the samples BLT-A8/9/10 in figure 4.10b. It can also be seen that the amount of water uptake is differing from the locations mainly due to different porosities (see table 4.3). Larger porosity al-

lows higher water content. Moreover, the water uptake by the core samples is lower than that by fine-grained powder. This may indicate there were some dead-pores in the cores, which did not allow water migrating into and being adsorbed on clay minerals.

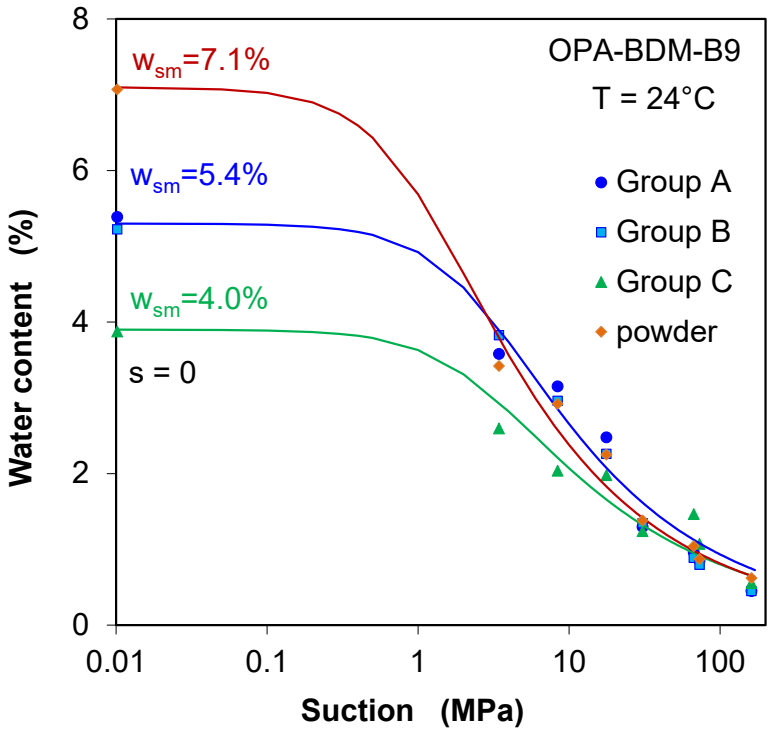

a. Samples from borehole BDM-B9

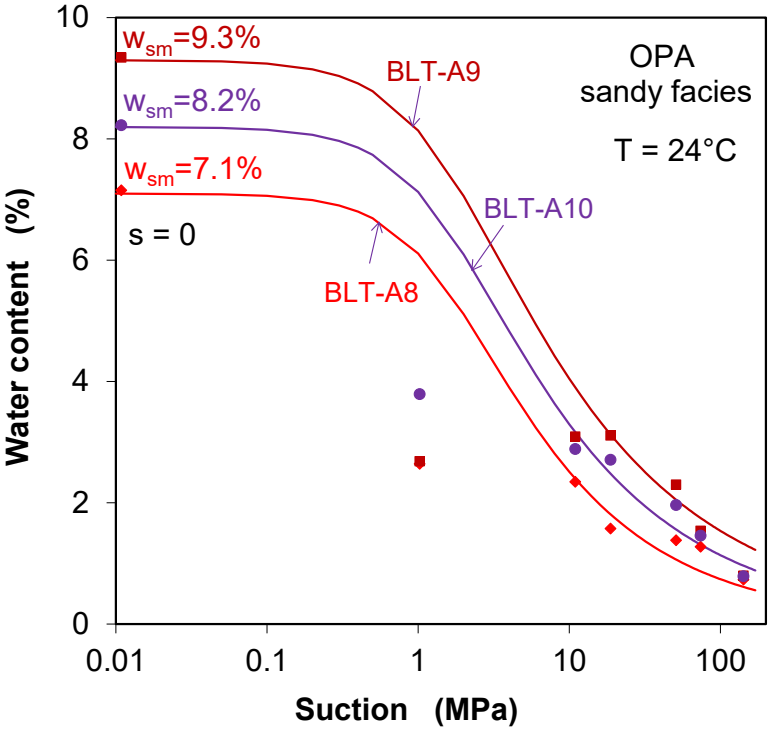

b. Samples from boreholes BLT-A8/9/10

Fig. 4.10 Water content-suction curves of the OPA sandy clay samples from borehole BDM-B9 (a) and BLT-A8/9/10 (b)

Tab. 4.2 Parameters of the water retention curves in expression of water content

Parameter	BDM-B9-A/B	BDM-B9-C	BDM-B9 powder	BLT-A8	BLT-A9	BLT-A10
w_m (%)	5.4	4.0	7.1	7.1	9.3	8.2
P_{ow} (MPa)	2.5	2.5	1.0	1.5	1.5	1.5
β (-)	0.32	0.30	0.32	0.35	0.30	0.32

The water retention behaviour is usually expressed by the degree of water saturation S_w (equation (2.6) via suction s. The van Genuchten model is rewritten as

$$S_w = \left[1 + \left(\frac{s}{P_{os}}\right)^{\frac{1}{1-\gamma}}\right]^{-\gamma} \tag{4.5}$$

where P_{os} and β are the material parameters. Determination of the model parameters needs constant dry density and porosity of the samples during the water uptake or release, which is usually achieved by volume-constant samples confined in cells. The data obtained in unconfined conditions like the tests reported above could be used only for approximately estimation of the parameters within certain limitation.

For instance, taking the averaged dry density and porosity of the tested samples constant (tables 2.6 and 2.7) and the normal water density of ρ_w = 1.0 g/cm^3, the degrees of water saturation S_w are calculated according to equation (2.6) from the water content w at suction s (cf. figure 4.10). Figure 4.11 shows the estimated S_w–data at the applied suctions. Because the water uptake at zero caused swelling and/or an increase in porosity as well as a decrease in dry density, the calculated saturation degree for the assumed constant dry density and porosity is higher than 100 %, indicating “oversaturation”. The exceedance must be disregarded in the approximation of water retention parameters for the pre-defined dry density and porosity. Fitting the data without S_w-values over 100 % yields different values of the parameters for the claystone in different locations, which are summarized in table 4.3. This implies that the water retention behaviour of the claystone is dependent on its inherent properties such as the mineralogical compositions, particularly the clay content, density and porosity, etc.

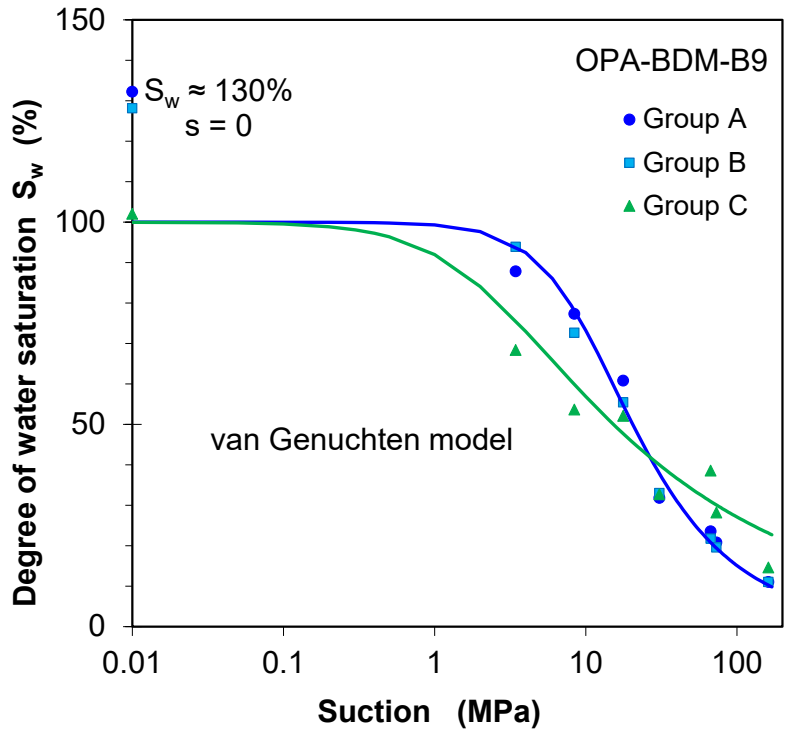

a. Samples from borehole BDM-B9

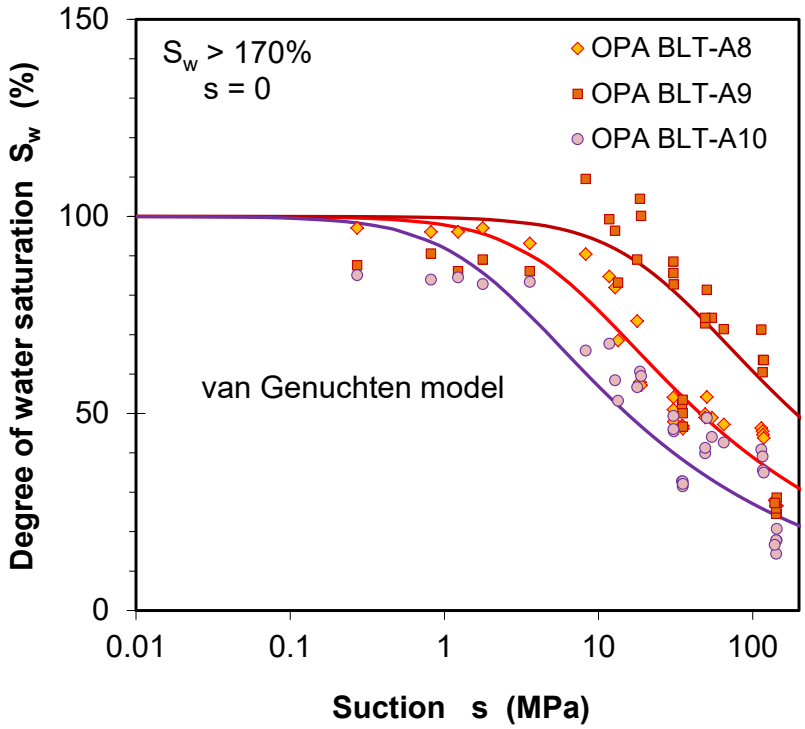

b. Samples from boreholes BLT-A8/9/10

Fig. 4.11 Saturation degree-suction curves of the OPA sandy clay samples from borehole BDM-B9 (a) and BLT-A8/9/10 (b)

Tab. 4.3 Parameters of the water retention curves in expression of saturation degree

Parameter	BDM-B9-A/B	BDM-B9-C	BLT-A8	BLT-A9	BLT-A10
ρ_d (%)	2.43	2.45	2.52	2.50	2.4
ϕ (%)	9.9	9.3	7.0	7.7	11.3
P_{os} (MPa)	10	2	6	25	2
γ (-)	0.45	0.25	0.25	0.25	0.25

4.2 Strain response to humidity change under load

In addition to the free swelling of claystone upon water uptake, swelling of claystone under load was examined by wetting and drying two samples under constant axial stress of 3.3 MPa in a coupled creep rig (figure 4.12). One sample OPA-BLT-A4 was taken from the OPA sandy facies and another one sample COX-EST44170 from the Callovo-Oxfordian clay formation at the -490 m level of the URL Bure. The initial characteristics of the samples are summarized in table 4.4. Both stressed samples were exposed to ventilating air at controlled relative humidity, whereby their axial strains were monitored by a deformation transducer. The temperature was ambient at 24 °C.

Tab. 4.4 Initial characteristics of the samples for swelling tests under uniaxial load

Sample	Size D/L (mm)	Bulk density ρ_b (g/cm^3)	Dry density ρ_d (g/cm^3)	Porosity ϕ (%)	Water content w (%)	Degree of saturation S_w (%)
OPA-BLT-A4	78/180	2.428	2.360	12.43	2.81	53.4
COX-EST44170	78/117	2.457	2.319	14.44	5.60	89.9

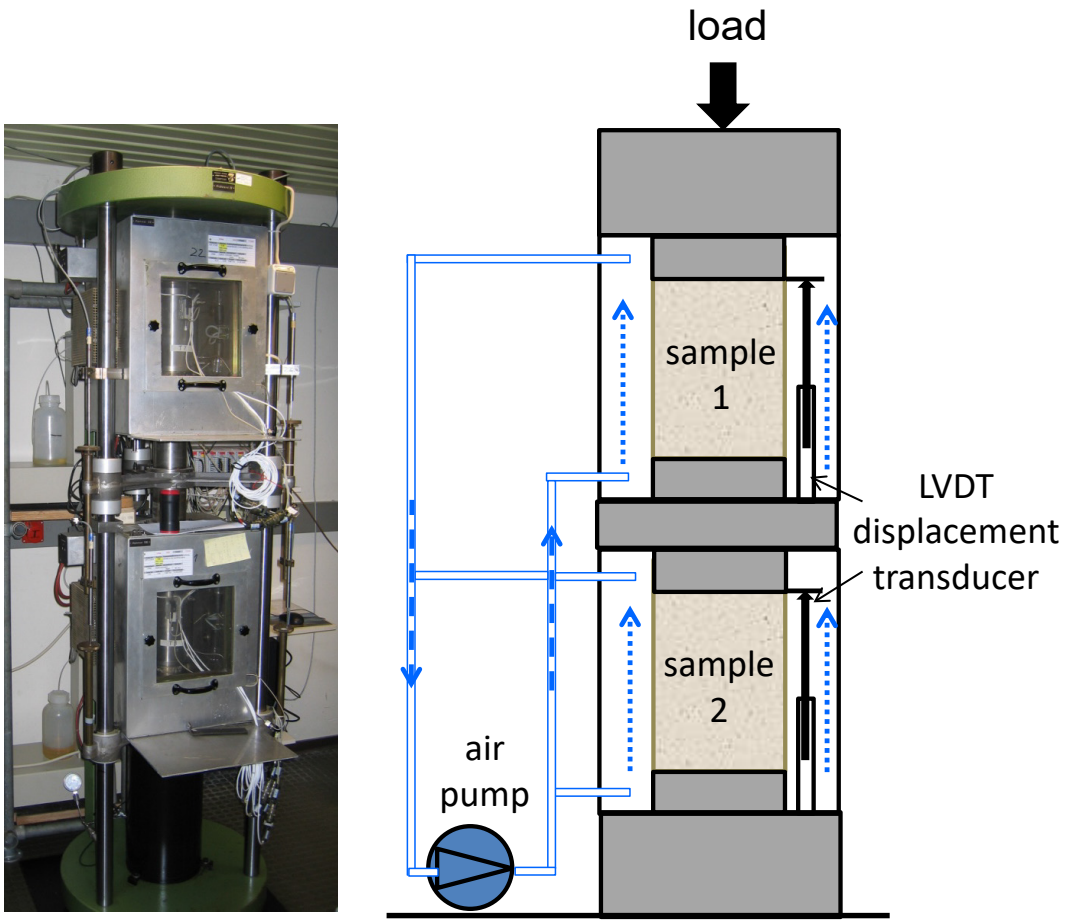

Fig. 4.12 A coupled rig for uniaxial creep testing on two samples one upon another with ventilation

Figure 4.13 demonstrates the response of axial strain to periodical variations of the air humidity for both samples. Initially, the samples were isolated in rubber jackets and deformed in compression with time. When exposed to air and wetted by increasing the air humidity from 55 % to 75 %, the progressive axial compression of both samples turned over to expansion even in the axial load direction. When the humidity decreased, the expansion turned over to compression again. The compression-expansion process repeated with subsequent drying-wetting cycles. Both samples exhibited the same behaviour. But the strain variation observed on the OPA sample is about one order of magnitude lower than that of the COX sample. This indicates a relatively low sensitivity of the OPA sandy claystone to humidity change compared to the COX claystone with more clay content. A very similar result has been obtained by Ziefle et al. /ZIE 17/, who monitored and numerically modelled the convergence of a niche in the URL Mont-Terri under the influence of seasonal humidity changes.

In fact, the expansion indicates a development of high swelling pressure exceeding the external load of 3.3 MPa. If the claystone had been constrained in constant volume and exposed to high humidity up to RH = 100 %, the swelling pressure might develop to higher levels equivalent to the *in situ* rock stresses (intermediate principal stress of 4 – 5 MPa and maximum of 6 – 7 MPa at Mont-Terri /BOS 04/ and /COR 07/. Such high swelling pressures were already observed by wetting the COX and OPA shaly claystones under uniaxially-fixed conditions /ZHA 13/17a/b/. Even under high confining stresses of 12 – 12.5 MPa and water injection pressures of 4 – 4.5 MPa, close to the *in situ* stress conditions at URL Bure, swelling strain up to 1% was observed on COX samples during water resaturation /ZHA 10a/13/17a/ and /BEL 18/. These observations provide significant evidence of the stress concept proposed by Horseman et al. /HOR 96/ and confirmed by Zhang /ZHA 13/17a/ for dense claystone. The stress concept suggests that a significant fraction of porewater in a dense claystone is adsorbed within the sheet structures of clay minerals and on the external surfaces of clay particles, which is, if not fully, capable of bearing effective stresses as high as the lithostatic ones and even bearing deviatoric stresses up to the material strength /HOR 96/ and /ZHA 13/17a/.

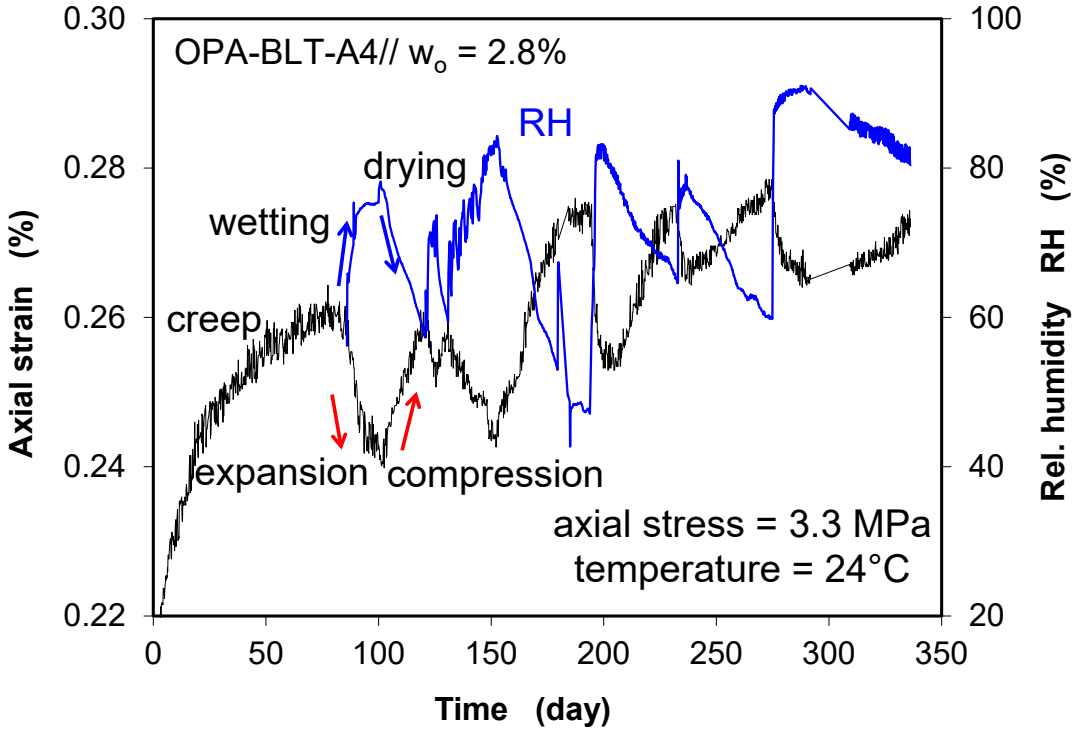

a. Sandy OPA claystone sample

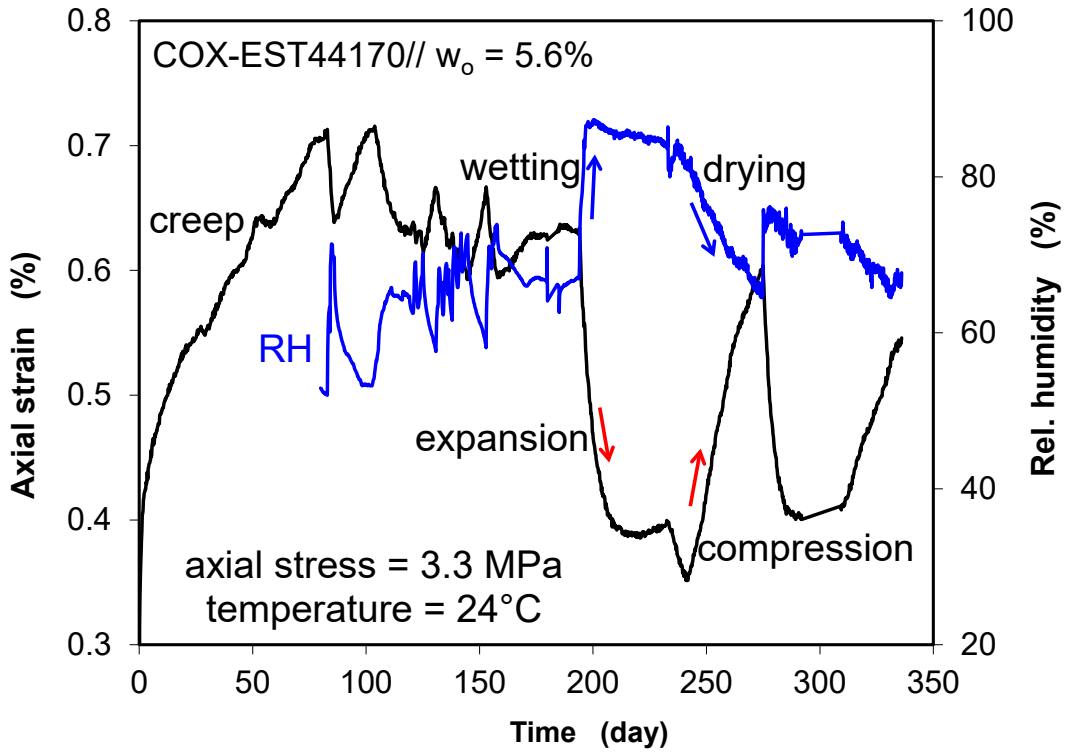

b. Clay-rich COX claystone sample

Fig. 4.13 Influences of humidity change on axial strain of the sandy OPA and clay-rich COX claystone samples under uniaxial load of 3.3 MPa

4.3 Influences of water content on stiffness and strength

In order to examine influences of water content on mechanical properties of the OPA sandy claystone, a series of uniaxial compression tests were carried out on five samples with different water contents of w = 0.6 % to 4.3 %, corresponding to saturation degrees of S_w = 22 % to 97 % (table 2.8). Figure 4.14 presents the results in terms of axial stress versus axial and radial strain (σ_a-ε_a, σ_a-ε_r), and volumetric strain versus axial strain (ε_v-ε_a). The envelopes of the uniaxial stress-strain curves of each sample show a nonlinear axial compression ($\varepsilon_a > 0$), radial extension ($\varepsilon_r < 0$) and volumetric compaction ($\varepsilon_r > 0$) with loading until the dilatancy threshold σ_D is reached, where the volume compaction reaches its maximum and then turns over to dilatation. The dilatation or damage develops, causing sample failure at peak stress σ_F. The data of σ_D and σ_F are summarized in table 4.5.

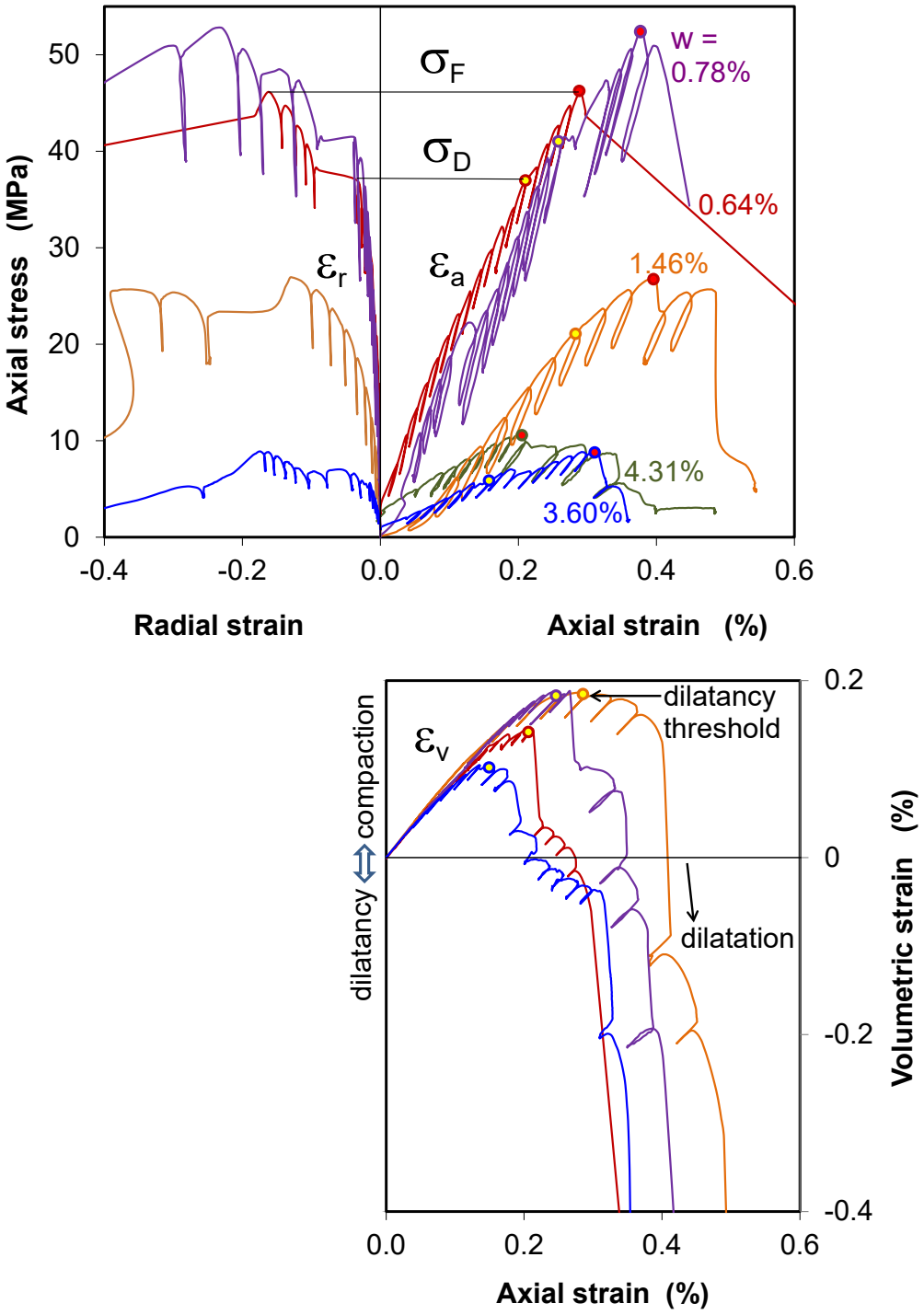

Fig. 4.14 Uniaxial stress-strain curves of the claystone samples with different water contents

Tab. 4.5 Uniaxial dilatancy threshold and failure strength of the samples from borehole BDM-B9 parallel to bedding and with different degrees of water saturation

Sample	Porosity ϕ (%)	Saturation degree S_w (%)	Dilatancy threshold σ_D (MPa)	Failure strength σ_F (MPa)	Fracture angle β (°)
B9-8	7.26	22.0	35.0	46.0	12
B9-14	5.45	30.9	39.0	51.0	8
B9-7	11.31	36.6	22.0	27.0	10
B9-5	9.49	92.7	5.5	8.9	10
B9-16	10.69	97.3	-	10.7	10

From each loading and unloading path, the elastic parameters were obtained at different load and deformation conditions. Figure 4.15 illustrates Young's modulus E and Poisson's ratio ν versus axial stress (E-σ_a, ν-σ_a). The uniaxial dilatancy threshold σ_D and peak strength σ_F are depicted in figure 3.34 as a function of water content w.

The mechanical behaviour and properties of the claystone are significantly affected by water content. When dried to low water contents, the claystone becomes brittle with high stiffness and strength. The low water content means more solid contacts between particles, which increase the friction resistance and strengthen of the inner structure. Contrarily, increasing water content results in widening of the distances between clay particles or increases the thickness of interparticle bound water-films, which reduces the inherent cohesion and friction resistance. Hence, the stiffness and strength decrease with increasing water content. For instance, the elastic stiffness of E = 5 - 10 GPa was obtained at water contents of w = 3.6 – 4.3 %, which is 2 – 4 times lower than E = 25 – 28 GPa obtained at low water contents of w = 0.6 – 0.8 % (figure 4.15); and the uniaxial strength of $\sigma_F \approx$ 10 MPa at w ≈ 4.0 % is four times lower than $\sigma_F \approx$ 50 MPa at a low w-value of ~0.7 % (figure 4.16).

It is also interesting to compare the uniaxial strength of the OPA sandy claystone parallel to bedding with that of the clay-rich COX claystone parallel to bedding /ZHA 17b/ as a function of degree of water saturation, as shown in figure 4.17. It can be clearly seen that the strength variations of both claystones are rather coincident, despite their differences in mineralogy, consolidation history and fabric. The strength of the dried claystones with a low water saturation of ~20 % is about five times that of the saturated ones.

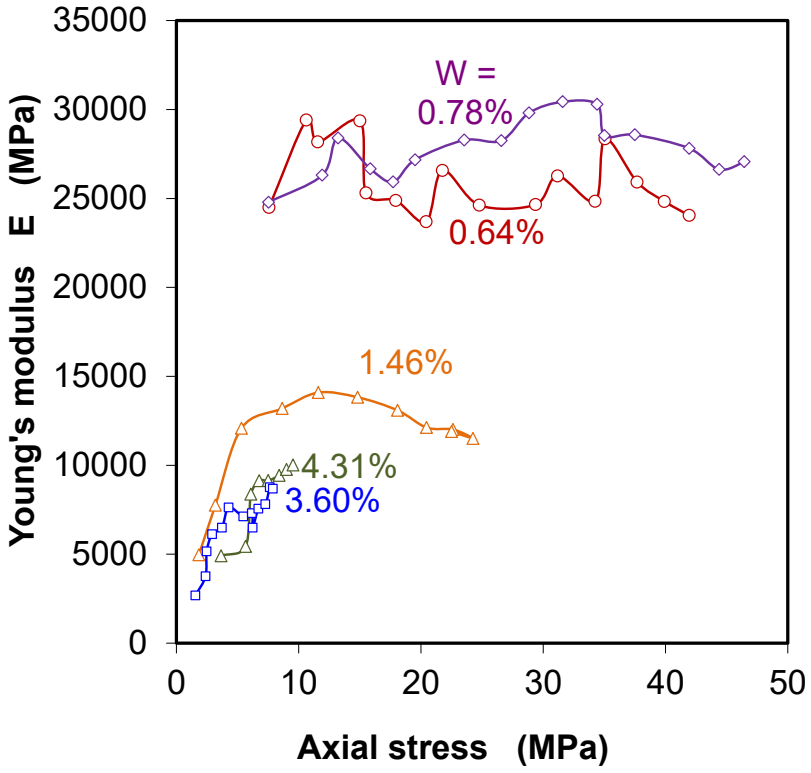

a. Young's modulus

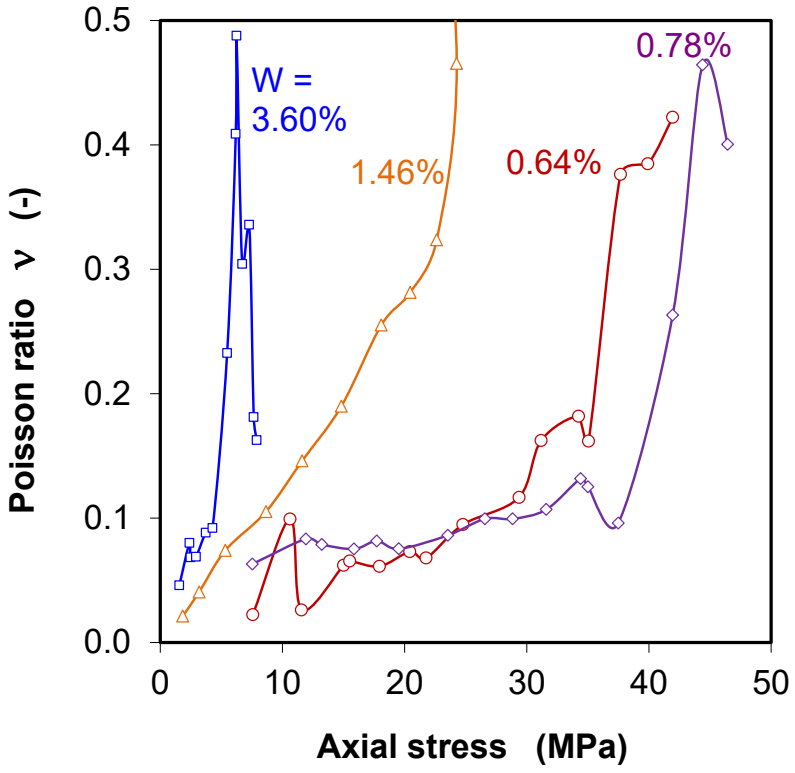

b. Poisson's ratio

Fig. 4.15 Elastic parameters as function of applied axial stress and water content

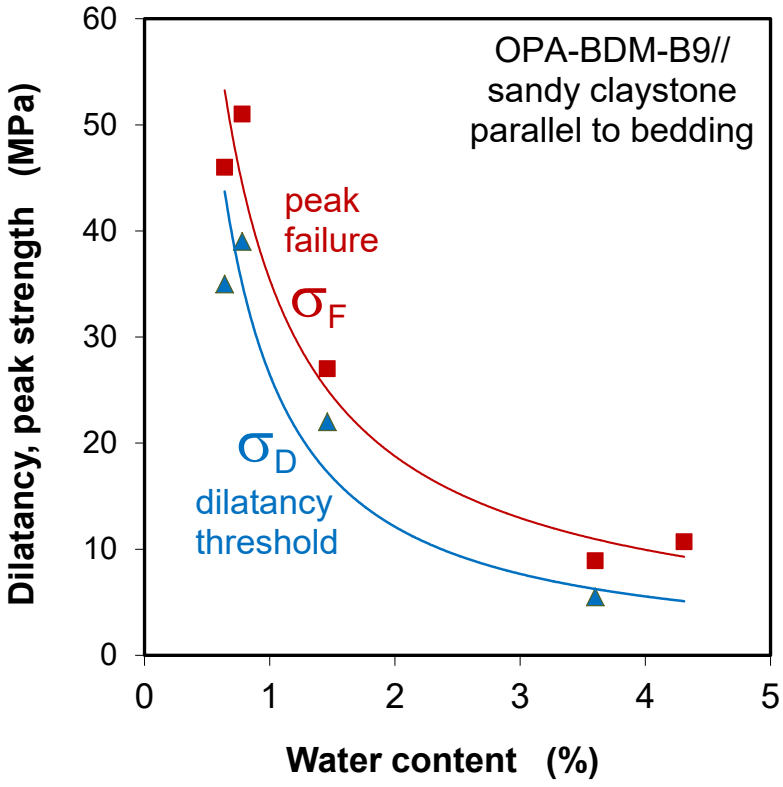

Fig. 4.16 Dilatancy threshold and peak failure strengths as a function of water content

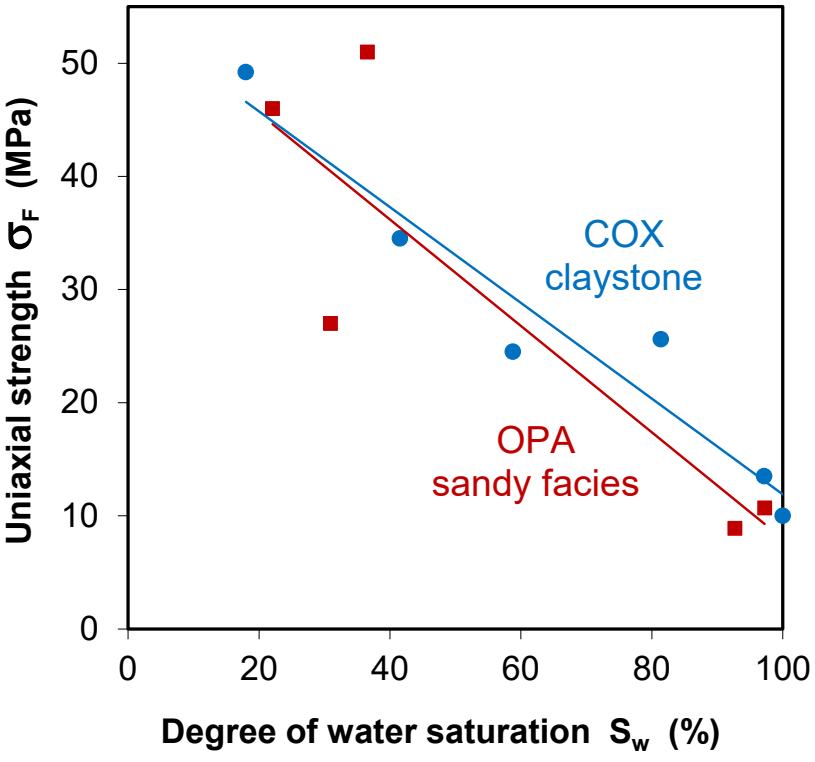

Fig. 4.17 Comparison of the uniaxial strengths between the OPA sandy and COX clay-rich claystones parallel to bedding as a function of water saturation

Figure 4.18 shows pictures of the failed samples. Most of the fractures generated by uniaxial loading are oriented almost axially parallel to the bedding planes, indicating that the fractures initiated from and penetrated through the weak bedding planes and finally extended in radial or minor principal stress direction.

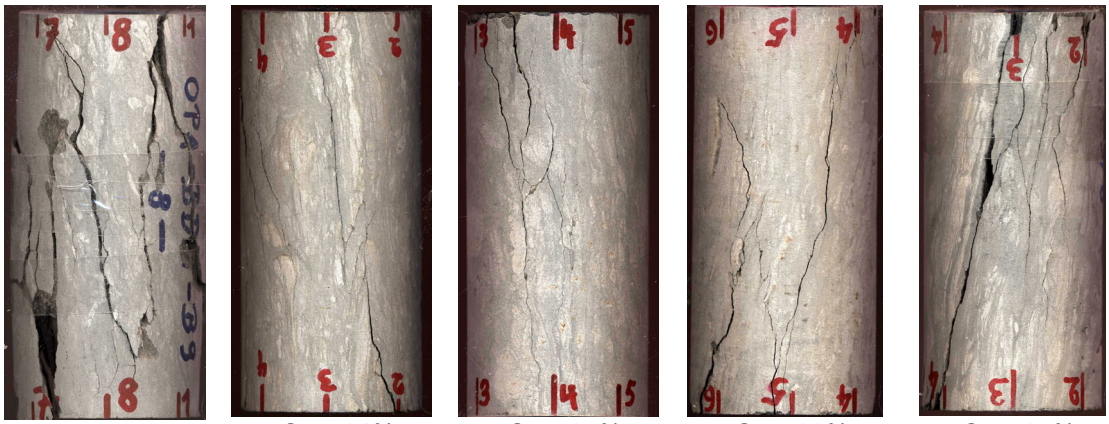

S_w = 22%
$\beta \approx 12°$
BDM-B9-8

S_w = 31%
$\beta \approx 8°$
BDM-B9-14

S_w = 37%
$\beta \approx 10°$
BDM-B9-7

S_w = 93%
$\beta \approx 10°$
BDM-B9-5

S_w = 97%
$\beta \approx 10°$
BDM-B9-18

Fig. 4.18 Pictures of the failed samples with fractures generated by uniaxial compression

5 Summary

The mechanical properties and behaviour of the sandy facies of Opalinus Clay at the URL Mont-Terri was experimentally investigated with a great number of samples under the prevailing repository conditions. The research work focused on determining a) the mechanical deformation, damage and strength under load conditions during repository excavation and operation; and b) moisture effects due to ventilation and water migration.

5.1 Main characteristics

The samples were taken from boreholes drilled parallel to bedding. The mineralogical composition of the studied sandy claystone displays a spatial variability: clays range from 24 – 41 %, quartz from 33 – 39 %, carbonates from 14 – 33 %, and feldspar from 8 – 9 %. The petrophysical properties vary too: the dry density along borehole BNM-B9 varies from 2.33 g/cm^3 to 2.53 g/cm^3 corresponding to porosity from 13.5 % to 6.5 %; but these are relatively constant along borehole BMB-A0 at dry density of 2.37±0.027 g/cm^3 and porosity of 11.7±1.30 %. The samples were inevitably desaturated to different degrees of 60 – 80 % and some micro-fissures were generated due to coring, storage and preparation. For mechanical testing, most of the samples were rewetted in humid air to high saturation degrees of 85 – 100 % and recompacted at isostatic stress of 15 MPa to minimize effects of the sampling-induced desaturation and micro-fissures. The applied stress corresponds to the maximum effective consolidation pressure (total overburden pressure – pore pressure) experienced during the geological history at the maximum burial depth of approximately 1350 m /MAZ 07/.

5.2 Deformation and strength

The mechanical experiments were carried out on the samples under drained and undrained triaxial compression and extension, cyclic compression, and multistep constant stresses for long time periods. The OPA sandy claystone under triaxial compression and extension showed the elastoplastic stress-strain behaviour with volumetric compaction until onset of dilatancy at high deviatoric stresses above 80 – 90 % of the peak failure strength. The volume compaction before dilatancy leads to an increase in elastic stiffness. In contrast, the dilatancy results in decrease of the stiffness. The strength is

dependent on load path in terms of Lode's angle and mean stress. The strength under triaxial compression is higher than that under extension. The respective strength increases with increasing mean stress. The strength behaviour of the claystone under triaxial compression and extension can be revealed by the Mohr-Coulomb's failure model implemented in the computing code CODE-BRIGHT /UPC 15/. The effective shear strength of the saturated sandy facies is higher than those of the shallow claystone /GIG 18/ and the shaly facies /WIL 18/ because of its lower clay content and lower porosity. However, the strength parameters obtained for these claystones need to be confirmed by more systematic experiments under repository-relevant conditions.

Time-dependences of deformation and strength of the claystone were observed. Under constant deviatoric stress, it crept continuously with time, which can be characterized by a transient phase and a following stationary phase, and even a tertiary phase at high deviatoric stresses to rupture. The creep of the OPA sandy claystone is slower than that of the clay-rich shaly facies of OPA and COX claystone. Even though some hypotheses have been proposed for creep and failure mechanisms in claystone, clear evidence is still missing and needs further precisely controlled long-term creep experiments and microstructural analysis.

5.3 Moisture effects

Moreover, significant moisture effects on the sandy claystone were observed in the laboratory experiments with various respects. The claystone exhibits high water adsorption potentials, under which a large amount of water can be taken up from humid environment. The maximal water uptake is reached in direct contact with a liquid phase and in unconfined conditions. Therein, the increased water content was almost doubled compared to in situ confined conditions. The water uptake causes significant free swelling, leading to a porosity increase of 30 % – 80 % when contacting liquid water. Even the claystone under uniaxial stress of 3.3 MPa, swelling in load direction happens during wetting by circulating humid air. Conversely, an arid environment causes drying, release of porewater, hence shrinkage and/or stress relaxation. The process of swelling and shrinkage is repeatable.

The swelling during wetting alters the internal structure of claystone and leads to degradation of the inherent cohesion between solid particles, so that the stiffness and strength of the claystones decrease with increasing water content. Conversely, the shrinkage during drying increases contacts between particles and leads to an increase in the cohesion and thus stiffness and strength. It was observed that the uniaxial strength of both the OPA sandy facies and COX claystone increases strongly with decreasing water saturation from about 10 MPa at full saturation up to 50 MPa at saturation degree of 20 %.

5.4 Outlook

Our investigation programme is still going on with more experiments to confirm the above conclusions, strengthen the data base, and enhance the knowledge of the mechanical behaviour of the sandy claystone. Some experiments were started 1 – 2 years ago and are continuing: a) long-term creep tests on five samples from the OPA sandy facies and COX claystone to study the time-dependent behaviour; and b) self-sealing tests on artificially-cracked samples from the OPA sandy facies and COX claystone to investigate the seal-sealing behaviour of fractures in these claystones. In the framework of the Work Package Gas in a new European project EURAD, GRS will investigate gas impact on fracture sealing in the different claystones. These investigations and results will be sequentially reported.

6 Acknowledgements

This work was funded by the German Federal Ministry for Economic Affairs and Energy (BMWi) under contract number 02E11304.

We would like to thank the staff of Swisstopo for their valuable on-site support. Many thanks to the colleagues of BGR for the fruitful discussions and helpful suggestions on the research work.

References

/AMN 15/ Amann F and Vogelhuber M (2015): Expert Report - Assessment of Geomechanical Properties of Intact Opalinus Clay. Retrieved from http://www.ensi.ch/de/wp-content/uploads/sites/2/2015/11/Assessment_ Geomechanical_Properties_Opalinus_Clay-ENSI_33_461_final.pdf

/AMN 17/ Amann F, Wild KM, Loew S, Yong S, Thoeny R, Frank E, (2017): Geomechanical behaviour of Opalinus Clay at multiple scales: results from Mont-Terri rock laboratory (Switzerland). Swiss Journal of Geosciences, DOI 10.1007/s00015-016-0245-0.

/ARM 14/ Armand G, Leveau F, Nussbaum C, de La Vaissiere R, Noiret A, Jaeggi D, Landrein P, Righini C (2014): Geometry and properties of the excavation-induced fractures at the Meuse/Haute-Marne URL drifts. Rock Mechanics and Rock Engineering 2014; 47(1): 21-41.

/AUV 15/ Auvray C, Grgic D, Morlot C, Fourreau E, Talandier J (2015): X-ray tomography applied to self-sealing experiments on argillites, The 13th International Congress of ISRM, "Innovations in Applied and Theoretical Rock Mechanics".

/BAK 17/ Bakker E, Kaszuba JP, Hangx SJT (2017): Assessing Chemo-mechanical Behavior Induced by CO2-Water-rock Interactions in Clay-rich Fault Gouges. Procedia Earth and Planetary Science, 17, 292–295. https://doi.org/10.1016/j.proeps.2016.12.060.

/BEL 18/ Belmokhtar M, Delage P, Ghabezloo S, Conil N (2018): Drained Triaxial Tests in Low-Permeability Shales: Application to the Callovo-Oxfordian Claystone. Rock Mechanics and Rock Engineering 51, 1979–1993.

/BOC 10/ Bock H, Dehandschutter B, Martin CD, Mazurek M, de Haller A, Skoczylas F, Davy C (2010): Self-sealing of fractures in argillaceous formations in the context of geological disposal of radioactive waste – Review and synthesis. NEA Report No. 6184. OECD.

/BÖH 18/ Böhm A and Gräsle W (2018): Mohr-Coulomb failure criterion for transversely isotropic materials, EUROCK 2018 - the ISRM European Rock Mechanics Symposium, Saint Petersburg, Russia, 22-26 May 2018.

/BOS 04/ Bossart P, Trick T, Meier PM, Mayor JC (2004): Structural and hydrogeological characterisation of the excavation-disturbed zone in the Opalinus Clay (Mont-Terri Project, Switzerland), Applied Clay Science 2004; 26(1-4): 429-48.

/BOS 17a/ Bossart P and Milnes AG (2017): Mont-Terri Rock Laboratory, 20 Years of Research and Experimentation on Claystones for Geological Disposal of Radioactive Waste, Swiss Journal of Geosciences, Vol. 110, No.1, 2017.

/BOS 17b/ Bossart P, Jaeggi D, Nussbaum C (2017): Experiments on thermo-hydro-mechanical behaviour of Opalinus Clay at Mont-Terri rock laboratory, Switzerland, Journal of Rock Mechanics and Geotechnical Engineering 9 (2017), 502-510.

/BRA 06/ Brady BHG and Brown ET (2006): Rock Mechanics for underground mining, third edition, Springer.

/CON 18/ Conil N, Talandier J, Djizanne H, de La Vaissière R, Righini-Waz C, Auvray C, Morlot C, Armand C (2018): How rock samples can be representative of in-situ condition: a case study of Callovo-Oxfordian claystones, Journal of Rock Mechanics and Geotechnical Engineering 10 (2018) 613-623.

/COR 07/ Corkum AG and Martin CD (2007): Modelling a mine-by test at the Mont-Terri rock laboratory, Switzerland. Int. J. Rock Mech. Min. Sci. 44(6): 846-859.

/CRI 98/ Cristescu ND and Hunsche U (1998): Time Effects in Rock Mechanics, John Wiley & Sons.

/DEL 15/ De La Vaissiere R, Armand G, Talandier J (2015): Gas and water flow in an excavation-induced fracture network around an underground drift: A case study for a radioactive waste repository in clay rock, Journal of Hydrology 521 (2015) 141–156.

/EWY 18/ Ewy RT (2018): Practical approaches for addressing shale testing challenges associated with permeability, capillarity and brine interactions. Geomechanics for Energy and the Environment 14, 3–15.

/FAV 18/ Favero V, Ferrari A, Laloui L (2018): Anisotropic Behaviour of Opalinus Clay Through Consolidated and Drained Triaxial Testing in Saturated Conditions. Rock Mechanics and Rock Engineering 51, 1305–1319.

/GIG 18/ Giger SB, Ewy RT, Favero V, Stankovic R, Keller LM (2018): Consolidated-undrained triaxial testing of Opalinus Clay: Results and method validation. Geomechanics for Energy and the Environment 14, 16–28.

/GIO 18/ Giot R, Auvray A, Talandier J (2018): Self-sealing of claystone under X-ray nanotomography, in Multiple Roles of Clays in Radioactive Waste Confinement (edited by Norris S, Neeft EAC & Van Geet M), Geological Society, London, Special Publications, 482, https://doi.org/10.1144/SP482.4.

/GUS 17/ Guss RJ, Harrington JF, Sathar S, Norris S, Talandier J (2017): The role of the stress-path and importance of stress history on the flow of water along fractures and faults; an experimental study conducted on kaolinite gouge and Callovo-Oxfordian mudstone. Applied Clay Science. DOI: 10.1016/j.clay.2017.09.029

/HOU 14/ Houben ME, Desbois G, Urai J (2014): A comparative study of representative 2D microstructures in Shaly and Sandy facies of Opalinus Clay (Mont-Terri, Switzerland) inferred form BIB-SEM and MIP methods, Marine and Petroleum Geology 49 (2014) 143-161.

/HOR 96/ Horseman ST, Higgo J JW, Alexander J, Harrington JF (1996): Water, Gas and Solute Movement through Argillaceous Media. Report CC-96/1.

/ISR 81/ ISRM (1981): Rock Characterization Testing & Monitoring – IRSM suggested methods, Commission on Testing Methods, International Society for Rock Mechanics.

/JAE 17/ Jaeggi D, Bossart P, Nussbaum C (2017): The Rock Mechanical Behavior of Opalinus Clay – 20 Years of Experience in the Mont-Terri Rock Laboratory, Advances in Laboratory Testing and Modelling of Soils and Shales (ATMSS), Springer Series in Geomechanics and Geoengineering. DOI 10.1007/978-3-319-52773-4_41.

/JOB 17/ Jobmann M, Bebiolka A, Burlaka V, Herold P, Jahn S, Lommerzheim A, Maßmann J, Meleshyn A, Mrugalla S, Reinhold K, Rübel A, Stark L, Ziefle G (2017): Safety assessment methodology for a German high-level waste repository in clay formations, Journal of Rock Mechanics and Geotechnical Engineering 9 (2017) 856-876.

/KAU 11/ Kaufhold A, Dohrmann R, Siegesmund S, Gräsle W, Plischke I (2011): Mineralogical and Microfabric Investigations of the Sandy Facies of Opalinus Clay (Mont-Terri), Clay characterisation from nanoscopic to microscopic resolution – proceedings of the NEA Clay Club workshop, Karlsruhe, Germany, 6-8 Sept. 2011, p.53-57, http://www.oecd-nea.org/globalsearch/download.php?doc=78225

/KAU 13/ Kaufhold A, Gräsle W, Plischke I, Dohrmann R, Siegesmund S (2013): Influence of carbonate content and micro fabrics on the failure strength of the sandy facies of the Opalinus Clay from Mont-Terri (Underground Rock Laboratory), Engineering Geology 156, 111-118. http://www.sciencedirect.com/science/article/pii/S0013795213000434

/KAU 16/ Kaufhold A, Halisch M, Zacher G, Kaufhold S (2016): X-ray computed tomography investigation of structures in Opalinus Clay from large-scale to small-scale after mechanical testing, Solid Earth 7, 1171-1183. https://www.solid-earth.net/7/1171/2016/se-7-1171-2016.pdf.

/LAU 14/ Laurich B, Urai J, Desbois G, Vollmer C, Nussbaum C (2014): Microstructural evolution of an incipient fault zone in Opalinus Clay: Insights from an optical and electron microscopic study of ion-beam polished samples from the Main Fault in the Mt-Terri underground research laboratory, J. Struct. Geol., 67, 107–128, doi:10.1016/j.jsg.2014.07.014.

/LIU 18/ Liu Z, Zhou CY, Li BT, LU YQ, Yang X (2018): A dissolution-diffusion sliding model for soft rock grains with hydro-mechanical effect, Journal of Rock Mechanics & Geotechnical Engineering 10 (2018) 457-467.

/LUP 81/ Lupini JF, Skinner AE, Vaughan PR (1981): The drained residual strength of cohesive soils. Geotechnique, 31(2), 181–213.

/MEN 15/ Menaceur H, Delage P, Tang A-M, Conil N (2015): The thermo-mechanical behaviour of the Callovo-Oxfordian claystone. Internat J Rock Mech Min Sci. 2015; 78:290–303.

/MAR 17/ Marschall P, Giger S, De La Vassiere R, Shao H, Leung H, Nussbaum C, Trick T, Lanyon B, Senger R, Lisjak A, Alcolea A. (2017): Hydro-mechanical evolution of the EDZ as transport path for radionuclides and gas: insights from the Mont-Terri rock laboratory (Switzerland), Swiss J Geosci (2017) 110:173–194.

/MAZ 06/ Mazurek M, Hurford AJ, Leu W. (2006): Unravelling the multi-stage burial history of the Swiss Molasse Basin: Integration of apatite fission track, vitrinite reflectance and biomarker isomerisation analysis. Basin Research, 18: 27-50.

/MAZ 08/ Mazurek M, Gautschi A, Marschall P, Vigneron G, Lebon P, Delay J (2008): Transferability of geoscientific information from various sources (study sites, underground rock laboratories, natural analogues) to support safety cases for radioactive waste repositories in argillaceous formations. Physics and Chemistry of the Earth, Vol. 33, 95-105.

/MIN 17/ Minardi A, Crisci E, Ferrari A, Laloui L (2017): The Role of Anisotropy on the Volumetric Behaviour of Opalinus Clay upon Suction Change, Advances in Laboratory Testing and Modelling of Soils and Shales (ATMSS), Springer Series in Geomechanics and Geoengineering. DOI 10.1007/978-3-319-52773-4_36.

/MIT 92/ Mitchell JK (1992): Characteristics and mechanisms of clay creep and creep rupture, “Clay-water interface and its rheological implications, Clay Mineral Society”, Vol.4, p. 212-244.

/NAG 02/ Nagra (2002): Project Opalinus Clay. Safety Report. Demonstration of disposal feasibility for spent fuel, vitrified high-level waste and long-lived intermediate-level waste. Nagra Tech. Rep. NTB 02-05. Nagra, Wettingen (2002b).

/NGA 14/ Nagra (2014): Sicherheitstechnischer Vergleich und Vorschlag der in Etappe 3 weiter zu untersuchenden geologischen Standortgebiete, NTB14-01, Nagra, Wettingen (2014).

/NAU 07/ Naumann M, Hunsche U, Schulze O (2007): Experimental investigations on anisotropy in dilatancy, failure and creep of Opalinus Clay, Phys. Chem. Earth Parts 32, 2007, 889–895.

/POP 07/ Popp T and Salzer K (2007): Anisotropy of seismic and mechanical properties of Opalinus clay during triaxial deformation in a multi-anvil apparatus, Phys. Chem. Earth Parts 32, 2007, 879–888.

/PEA 03/ Pearson FJ, Arcos D, Bath A, Boisson J-Y, Fernandez AM, Gäbler H-E, Gaucher E, Grifault L, Hernan P, Waber HN (2003): Mont-Terri Project – Geochemistry of Water in the Opalinus Clay formation at the Mont-Terri Rock Laboratory, Reports of the FOWG, no. 5, 2003, Bern.

/RUT 83/ Rutter EH (1983): Pressure solution in nature, theory and experiment. Journal of Geological Society, London, Vol. 140, pp. 725-740.

/STA 18/ Stavropoulou1 E, Ando E. Tengattini A, Briffaut M, Dufour F, Atkins D, Armand G (2018): Liquid water uptake in unconfined Callovo Oxfordian clay-rock studied with neutron and X-ray imaging, Acta Geotechnica, https://doi.org/10.1007/s11440-018-0639-4.

/SWI 18/ Swisstopo (2018): Programme Overview and Work Programme of Phase 24 (July 2018 – June 2019. International Research Project in the Mont-Terri Rock Laboratory for the Hydrogeological, Geochemical and Geotechnical Characterisation of an Argillaceous Formation (Opalinus Clay). Swiss Federal Office of Topography, Seftigenstrasse 264, 3084 Wabern, Switzerland.

/THU 99/ Thury M and Bossart P (1999): Mont-Terri Rock Laboratory, Results of the hydrogeological, geochemical and geotechnical experiments performed in 1996 and 1997. Landeshydrologie und –geologie, Geologischer Bericht No. 23. Federal Officie of Topography (swisstopo), Wabern, Switzerland.

/UPC 15/ UPC (2015): User's Guide of CODE_BRIGHT - A 3-D Program for Thermo-Hydro-Mechanical Analysis in Geological Media, Department of Geotechnical Engineering and Geosciences of Technical University of Catalonia (UPC), Barcelona, Spain.

/VÖB 14/ Vöbel T, Gräsle W, Plischke I (2014): LT-A Experiment: Strength and Deformation of Opalinus Clay: Data report from phase 19, Technical Report 2014-06 of the Mont-Terri Project, Federal Institute for Geosciences and Natural Resources (BGR), Hannover, Germany.

/WIL 15/ Wild, KM, Wymann LP, Zimmer S, Thoeny R, Amann F (2015): Water Retention Characteristics and State-Dependent Mechanical and Petro-Physical Properties of a Clay Shale. Rock Mechanics and Rock Engineering 48, 427–439. https://doi.org/10.1007/s00603-014-0565-1

/WIL 17/ Wild KM, Barla M, Turinetti G, Amann F (2017): A multi-stage triaxial testing procedure for low permeable geomaterials applied to Opalinus Clay. Journal of Rock Mechanics and Geotechnical Engineering 9, 519–530.

/WIL 18/ Wild KM and Amann F (2018): Experimental study of the hydro-mechanical response of Opalinus Clay – Part 1: Pore pressure response and effective geomechanical properties under consideration of confinement and anisotropy. Engineering Geology 237, 32–41.

/YU 17/ Yu C, Matray JM, Goncalves J, Jaeggi D, Gräsle W, Wieczorek K, Vogt T, Sykes E (2017): Comparative study of methods to estimate hydraulic parameters in the hydraulically undisturbed Opalinus Clay (Switzerland), Swiss J Geosci (2017) 110: 85-104.

/ZHA 07/ Zhang CL, Rothfuchs T, Jockwer N, Wieczorek K, Dittrich J, Müller J, Hartwig L, Komischke M (2007): Thermal Effects on the Opalinus Clay – A Joint Heating Experiment of ANDRA and GRS at the Mont-Terri URL (HE-D Project), Final report GRS-224, February 2007.

/ZHA 10/ Zhang CL, Wieczorek K, Xie ML (2010a): Swelling experiments on mudstones, Journal of Rock Mechanics & Geotechnical Engineering, 2010, 2(1): 41-47.

/ZHA 11/ Zhang CL (2011): Experimental evidence for self-sealing of fractures in claystone, Physics and Chemistry of the Earth, Vol. 36, 2011, 1972-1980.

/ZHA 13a/ Zhang CL (2013): Sealing of Fractures in Claystone, Journal of Rock Mechanics and Geotechnical Engineering 5 (2013), 214-220.

/ZHA 13b/ Zhang CL, Czaikowski O, Rothfuchs T, Wieczorek K (2013): Thermo-Hydro-Mechanical Processes in the Nearfield around a HLW Repository in Argillaceous Formations, Project Report THM-TON, GRS-312.

/ZHA 15/ Zhang CL (2015): Long-term deformation of clay rock under various thermo-hydro-mechanical conditions, Proceedings of the ISRM Regional Symposium EUROCK 2015 & 64th Geomechanics Colloquium, 689-694.

/ZHA 17a/ Zhang CL (2017a): Examination of Effective Stress in Clay Rock, Journal of Rock Mechanics and Geotechnical Engineering 9 (2017) 479-489.

/ZHA 17b/ Zhang CL (2017b): Response of clay rock to moisture change, in: Advances in Laboratory Testing and Modelling of Soils and Shales (ATMSS), Springer Series in Geomechanics and Geoengineering, DOI 10.1007/978-3-319-52773-4 17.

/ZHA 19/ Zhang CL, Armand G, Conil N, Laurich B (2019): Investigation on Anisotropy of Mechanical Properties of Callovo-Oxfordian Claystone, Engineering Geology 251 (2019) 128-145. https://doi.org/10.1016/j.enggeo.2019.02.008.

List of tables

Tab. 2.1 Main mineralogical components of the sandy facies from borehole BDM-B9 8

Tab. 2.2 Characteristics of the samples from borehole BMB-A0 parallel to bedding for triaxial compression tests (sample size: D = 70 mm, L = 140 mm) 10

Tab. 2.3 Characteristics of the samples from borehole BMB-A0 parallel to bedding for triaxial extension tests (sample size: D = 50 mm, L = 100 mm) 11

Tab. 2.4 Characteristics of the samples from borehole BDM-B9 parallel to bedding for triaxial cyclic compression tests (sample size: D=70mm, L=140 mm) 12

Tab. 2.5 Initial characteristics of the samples for creep tests 12

Tab. 2.6 Initial characteristics of the samples (D=70mm, L=20mm) for measurement of water retention and volume change at different humidities 13

Tab. 2.7 Average characteristics of the samples from boreholes BLT-A8/9/10 for measurement of water retention 14

Tab. 2.8 Characteristics of the reconditioned samples from borehole BMB-B9 parallel to bedding for testing moisture effects on uniaxial deformation and strength (sample size: D = 70 mm, L = 140 mm)..... 14

Tab. 3.1 Dilatancy threshold σ_D, peak strength σ_F and residual strength σ_R obtained on the dried samples in group 1 and wetted samples in group 2 during deviatoric loading (the characteristics of the samples in table 2.2) 35

Tab. 3.2 Characteristics of the samples from borehole BMB-A0 parallel to bedding for triaxial extension tests 43

Tab. 3.3 Results of the pre-compaction and deviatoric compression on the samples from borehole BDM-B9 parallel to bedding 48

Tab. 3.4 Mohr-Coulumb's strength parameters of the OPA sandy and shaly facies and the shallow claystone at a depth of 33 m below ground 57

Tab. 4.1 Final characteristics of the samples in equilibrium at different humid conditions and maximal water contents reached by wetting with water 79

Tab. 4.2 Parameters of the water retention curves in expression of water content..... 85

Tab. 4.3 Parameters of the water retention curves in expression of saturation degree 87

Tab. 4.4 Initial characteristics of the samples for swelling tests under uniaxial load..... 87

Tab. 4.5 Uniaxial dilatancy threshold and failure strength of the samples from borehole BDM-B9 parallel to bedding and with different degrees of water saturation 92

List of figures

Fig. 1.1 Geological structure map and horizontal cross section of the Underground Rock Laboratory Mont-Terri (taken from Swisstopo, 2019) 2

Fig. 2.1 Positions of boreholes drilled in the sandy facies of Opalinus Clay at URL Mont-Terri 5

Fig. 2.2 Pictures of some drilled cores from boreholes BMB-A0 and BDM-B9 parallel to bedding 6

Fig. 2.3 Pictures of the confinement, storage and preparation of test samples 7

Fig. 2.4 Distributions of grain density along borehole length for boreholes BMB-A0 and BMB-B9 16

Fig. 2.5 Distributions of dry density and porosity along borehole length for boreholes BMB-A0 and BDM-B9 17

Fig. 2.6 Distributions of water content and saturation degree along borehole length for boreholes BMB-A0 and BDM-B9 18

Fig. 2.7 Comparison of water content and saturation degree of the samples in the initial conditions (w_o, S_{wo}) and after resaturation (w_r, S_{wr}) at 100 % relative humidity over 1.5 months 18

Fig. 2.8 Wetting-induced cracks along bedding planes in an unconfined sample (diameter = length = 100 mm) at relative humidity of 100% over 6 months 18

Fig. 3.1 Assemble of sample for triaxial testing (a) under undrained (b) and drained (c) conditions 21

Fig. 3.2 Load paths applied in mechanical testing of the OPA sandy claystone 22

Fig. 3.3 A triaxial testing system with thermo-hydro-mechanical control and measurements of deformation, permeability, and ultrasonic wave velocity 26

Fig. 3.4 A coupled rig for triaxial creep testing on two samples one upon another 27

Fig. 3.5 Typical results of the pre-compaction of the delivered and wetted samples under undrained and isostatic load conditions 29

Fig. 3.6 Volumetric compaction of the non-wetted and rewetted samples under undrained and isostatic load conditions 30

Fig. 3.7 Typical deviatoric stress-strain curves ($\Delta\sigma$–ε_a, $\Delta\sigma$–ε_r, ε_v–ε_a) of the claystone with dilatancy threshold σ_D, peak strength σ_F and residual strength σ_R 31

Fig. 3.8 Stress-strain behaviour of the no-wetted and rewetted samples during deviatoric loading 33

Fig. 3.9 Comparison of the deviatoric stress-strain curves of the dried and wetted samples at constant radial stress in a range from 0.5 to 4 MPa 34

Fig. 3.10 Dilatancy, peak and residual strengths of the claystone dried to saturation degree of S_w = 68±9.0% and wetted to S_w = 85±5.0% as a function of radial stress 36

Fig. 3.11 Pictures of some failed samples with induced fractures after deviatoric compression at different radial stresses 37

Fig. 3.12 Shear fracture angles observed on the failed samples under different radial stresses in comparison with the model result 37

Fig. 3.13 Volumetric compaction of the dried samples with saturation degrees of 61±7.0% under undrained and isostatic load conditions 38

Fig. 3.14 Evolution of applied stresses during the triaxial extension (TEM) by lateral compression and axial extension 39

Fig. 3.15 Stress-strain curves obtained on the dried samples with saturation degrees of 52-63% during lateral compression and axial extension at constant mean stress in a range of 15 to 20 MPa 40

Fig. 3.16 Evolution of applied stresses during the triaxial extension (TEA) by lateral compression at constant axial stress 41

Fig. 3.17 Stress-strain curves obtained on the dried samples with saturation degrees of 46-67% during lateral compression at constant axial stress in a range of 1 to 8 MPa..... 42

Fig. 3.18 Pictures of some samples fractured under triaxial extension at constant mean and axial stresses 44

Fig. 3.19 Volumetric compaction of the samples during isostatic loading/unloading cycle in dependence on degree of water saturation..... 45

Fig. 3.20 Stress-strain curves obtained on four highly saturated samples during cyclic deviatoric loading/unloading 47

Fig. 3.21 Evolution of Young's modulus and Poisson's ratio obtained from unloading and reloading paths with deviatoric stress and deformation..... 50

Fig. 3.22 Elastic parameters averaged for each reloading-unloading cycle in correlation with volume change during deviatoric loading 51

Fig. 3.23 Variations of the elastic parameters with axial strain during deviatoric loading under different radial confining stresses 52

Fig. 3.24 Dilatancy and peak failure strengths of the OPA sandy claystone as function of radial stress 53

Fig. 3.25 Pictures of some failed samples with induced fractures after deviatoric compressional loading at constant radial stresses 53

Fig. 3.26 Shear strength of the OPA sandy claystone under triaxial compression at constant radial stress (TCS & TCD: $\sigma_r = c$) and extension at constant mean (TEM: $\sigma_m = c$) or axial stress (TEA: $\sigma_a = c$) as a function of mean stress and degree of water saturation (S_w) 55

Fig. 3.27 Parameter cohesion related to the degree of water saturation 55

Fig. 3.28 Comparison of the Mohr-Coulumb's failure envelopes of the saturated OPA sandy facies (present work), shaly facies (Wild and Amann, 2018 /WIL 18/), and shallow claystone (Giger et al., 2018 /GIG 18/) under drained and undrained triaxial compression 57

Fig. 3.29 Pre-compaction of the sample under the undrained isostatic stress conditions 59

Fig. 3.30 Results of a multistep triaxial creep test on a highly-saturated sample..... 60

Fig. 3.31 Comparison of the dilatancy and peak strengths observed on the OPA sandy claystone during the short and long-term tests 61

Fig. 3.32 Creep of the saturated and dried samples under multistep triaxial loads 62

Fig. 3.33 Comparison of the steady-state creep rates between the OPA sandy claystone and the clay-rich OPA and COX claystones 65

Fig. 4.1 Pictures of the powder and disc samples from borehole BDM-B9 for measurement of water retention properties 68

Fig. 4.2 Pictures of the OPA sandy claystone samples OPA-BLT-A8/9/10 for measurement of water retention properties 69

Fig. 4.3 Measurement of water retention properties of the samples in desiccators at different relative humidities..... 70

Fig. 4.4 Evolution of water content and volumetric strain observed on the OPA sandy-clay samples in different humid conditions 76

Fig. 4.5 Water contents and volumetric strains of the OPA sandy claystone from borehole BDM-B9 at different suctions 77

Fig. 4.6 Water retention curves of the OPA sandy claystone from different boreholes BLT-A8/9/10 78

Fig. 4.7 Samples wetted by contacting to synthetic clay water at bottom 80

Fig. 4.8 Cracks generated in the OPA sandy claystone by water penetration 81

Fig. 4.9 Maximum water contents and final porosities of the OPA sandy claystone samples after saturation in synthetic clay water 82

Fig. 4.10 Water content-suction curves of the OPA sandy clay samples from borehole BDM-B9 (a) and BLT-A8/9/10 (b) 84

Fig. 4.11 Saturation degree-suction curves of the OPA sandy clay samples from borehole BDM-B9 (a) and BLT-A8/9/10 (b) 86

Fig. 4.12 A coupled rig for uniaxial creep testing on two samples one upon another with ventilation 88

Fig. 4.13 Influences of humidity change on axial strain of the sandy OPA and clay-rich COX claystone samples under uniaxial load of 3.3 MPa 90

Fig. 4.14 Uniaxial stress-strain curves of the claystone samples with different water contents 91

Fig. 4.15 Elastic parameters as function of applied axial stress and water content 93

Fig. 4.16 Dilatancy threshold and peak failure strengths as a function of water content 94

Fig. 4.17 Comparison of the uniaxial strengths between the OPA sandy and COX clay-rich claystones parallel to bedding as a function of water saturation 94

Fig. 4.18 Pictures of the failed samples with fractures generated by uniaxial compression 95

Gesellschaft für Anlagen- und Reaktorsicherheit (GRS) gGmbH

Schwertnergasse 1
50667 Köln
Telefon +49 221 2068-0
Telefax +49 221 2068-888

Boltzmannstraße 14
85748 Garching b. München
Telefon +49 89 32004-0
Telefax +49 89 32004-300

Kurfürstendamm 200
10719 Berlin
Telefon +49 30 88589-0
Telefax +49 30 88589-111

Theodor-Heuss-Straße 4
38122 Braunschweig
Telefon +49 531 8012-0
Telefax +49 531 8012-200

www.grs.de

ISBN 978-3-947685-40-0